U.PORTO
FACULDADE DE CIÊNCIAS
UNIVERSIDADE DO PORTO

Development of an Algorithm for a GNSS/MEMS-IMU/Imaging Coupled System for Direct Georeferencing

Wenlin Yan
Engenharia Geográfica
Departamento de Geociências Ambiente e Ordenamento do Território
2017

Orientador
M. Luísa M. C. Bastos, Investigador Principal,
Faculdade de Ciências da Universidade do Porto

Coorientador
José A. Gonçalves, Professor Auxiliar,
Faculdade de Ciências da Universidade do Porto

PhD

Acknowledgements

Time always goes by quickly. I still remember the situation when I came to Porto in February 2011. At that time I had the ambition to reach a great academic level in several years, and this wish was like the leaves of a cup of tea: at the beginning they are holding on the top of the water, after a period of time they extend and subside gradually, meanwhile the tea becomes more and more flavored.

At first, I would like to give my gratitude to my supervisor Dr. Luísa Bastos and Porto University, because she and the university provided me the means for further opportunities and to get the experience in GNSS/IMU related applications. Because of this chance, not only my methodologies to deal with academic problems, but also the thinking of life were improved or redesigned. Secondly, great respect should be delivered to my co-supervisor Prof. José A. Gonçalves, his excellent acknowledge and skill in photogrammetry inspired me greatly, and his suggestions becomes the critical part of this thesis. I would like to give my thanks to the colleagues, Mr. Américo Magalhães, an excellent engineer to validate the designed tests, and he always gives timely help to my living problems in Porto; Dr. Dalmiro Maia, Dr. Sérgio Madeira, Dr. Richard Deurloo, Dr. Machiel Bos, Mr. Diogo Ayres-Sampaio, Dr. Paulo Marreiros and the other excellent researchers I met in Portugal, the conversations with those peoples benefit me from different aspects of the academic; Ms. Mónica Sofia Guerreiro Rodrigues, her “Bom Dia” gives me a delighted start every day; I would like to further acknowledge Prof. Rui Moura, from the Faculty of Science of the University of Porto, for conducting the flight tests in the Espinho area.

Meanwhile, I would also give my thanks to the project of “PITVANT” (Projecto de Investigação e Tecnologia em Veículos Aéreos Não-Tripulados) funded by the Portuguese Ministry of Defense, and the project of “DEOSOM” (Detection and Evaluation of Oil Spills by Optical Methods), those project give me the opportunities to work in Porto University from 2011 to 2013, and this work experience gives me a good start for the further PhD study.

Then, I also want deliver my thanks to some researchers in China side: Prof. Jian Wang and Prof. Jingxiang Gao, thanks for their guiding in many aspects not only in academic since the year of 2003; Prof. Yingcheng Li, thanks for your work opportunity and the help with using the commercial photogrammetry software from your company; Prof. Guochang Xu and Prof. Tianhe Xu, thanks for your work opportunities in Shandong University, and the guides of the robust adaptive Kalman Filter; Prof. Qiuzhao Zhang, Prof. Chao Liu, Dr. Feng Zhou, thanks for the conversations in GNSS area, and also want to give many apologies to the persons who gave me support but not possible to mention in this thesis.

Finally, I would like to give thanks to my familly members: my little daughter Anna Yan, her birth brought me joy beyond description; my wife Ying Kang, her love to me becomes the pills to kill off the pains from any crisis in my life; my mother and father, my mother and father in law, and my brother and his wife, thanks for all their understanding and support.

Resumos

Nos levantamentos fotogramétricos aéreos a determinação de parâmetros de orientação externa precisos é um aspecto crítico da georeferenciação direta. O desempenho do sistema de Posicionamento e Orientação (POS Position and Orientation System), em particular a precisão da orientação, é um dos fatores mais importantes para fotogrametria aérea, especialmente quando são usados veículos aéreos ligeiros, incluindo veículos não tripulados (UAV, Unmanned Aeral Vehicles). O baixo custo do POS que atualmente são usados na maioria dos veículos aéreos ligeiros, nomeadamente em UAVs, possuem algumas limitações, como a baixa precisão na orientação, que é obtida a partir de sensores MEMS IMUs (Micro-Electro-Mechanical System, Inertial Measurement Units) de baixa precisão. Neste contexto, a precisão da orientação de um POS de baixo custo, que possa ter um desempenho equivalente a um POS de grau superior, é do maior interesse.

A precisão de um POS pode ser melhorada otimisando as estratégias de integração de sistemas GNSS e IMU, com base em diferentes arquiteturas de acoplamento, tais como integração *loosely*, *tightly*, ou *deeply coupled* e uma configuração apropriada do filtro de Kalman utilizado, e/ou através da incorporação de informações adicionais, provenientes por exemplo de um radar, odómetro, modelo de terreno, etc. Na última década, com a disponibilidade de câmaras de alta resolução de menor custo, outras estratégias tornaram possível explorar a fusão de medidas GNSS e IMU com imagem para melhorar a precisão do POS. A disponibilidade de sensores miniaturizados, com capacidades melhoradas, e novos métodos para o processamento de imagem, juntamente com o aparecimento das plataformas aéreas ligeiras, para aquisição de dados, nomeadamente os veículos não tripulados abriu uma série de novas possibilidades para aplicações de navegação geodésica, alavancando novos desenvolvimentos na fusão de sensores. Dada a limitação da capacidade de carga e fornecimento de energia nos veículos aéreos pequenos, foi desenvolvido um o algoritmo GNSS/MEMS-IMU que integra também informação das imagens obtidas pela câmara acoplada ao sistema. Esta abordagem tem a vantagem de permitir mellhorar o desempenho do sistema com base na concepção e configuração adequada do filtro usado no algoritmo de processamento, e sem a introdução de quaisquer dispositivos adicionais.

Neste trabalho, foi implementado um sistema de georeferenciação direta simples e barato, composto por um receptor GNSS de frequência dupla, um IMU de baixo custo e uma pequena câmara digital, para uso em plataformas aéreas ligeiras. Com o objetivo de melhorar o desempenho de orientação deste tipo de sistema de baixo custo, projetado para ser usado em

veículos aéreos ligeiros, o trabalho de investigação apresentado nesta tese foca-se nos seguintes principais aspectos:

1) Validação dos algoritmos de triangulação aérea, georeferenciação direta (forward intersection) e ajuste do levantamento fotogramétrico com este sistema.

2) Validação das funções de navegação de integração GNSS/MEMS-IMU aplicando um Filtro de Kalman de 15 estados, demonstração de equivalência do Filtro de Kalman de *loosely* e *tightly* coupled sob a condição de haver boa visibilidade nas observações GNSS.

3) Implementação de um Filtro de Kalman GNSS/MEMS-IMU aumentado com a informação geométrica obtida a partir de imagens consecutivas, uma vez que a orientação relativa pode ser obtida com precisão a partir de imagens consecutivas usando um algoritmo SIFT/SFM (Scale-Invariant Feature Transform/Structure From Motion) apropriado. A incorporação no Filtro de Kalman desta informação sobre a orientação relativa permite melhorar significativamente a precisão dos parâmetros de orientação externa.

4) Utilização de um Filtro de Kalman robusto adaptativo, com a determinação do fator adaptativo e do fator robusto realizado pela informação de inovação e pelo estabelecimento de limites para os valores relativos a mudanças de orientação entre imagens consecutivas, o que permite melhorar ainda mais o desempenho do novo método.

Os resultados dos testes aéreos reais usados para avaliar o desempenho do método confirmam a sua eficiência. Os resultados mostram que usando uma câmara simples e barata, a solução de orientação resultante da integração GNSS/MEMS-IMU pode ser melhorada significativamente até cerca de 60% se a informação geométrica obtida das imagens for introduzida. Melhoria adicional pode ser obtida aplicando um Filtro de Kalman robusto adaptativo. Os testes também mostraram que a precisão do método proposto depende, fundamentalmente, da taxa de sobreposição das imagens e da qualidade da câmara.

O sistema implementado garante uma solução de orientação de boa qualidade para aplicações fotogramétricas usando veículos aéreos ligeiros (incluindo UAVs) com a vantagem de ser eficiente e acessível. Esse tipo de abordagem pode ser explorada para uso em outros tipos de aplicações, como a navegação em ambientes desafiantes.

Palavras-chave: GNSS/MEMS-IMU/Imaging navegação acoplada; POS; Georeferenciação direta; Filtro de Kalman robusto adaptativo; SFM/SFIT.

Abstract

The determination of precise exterior parameters is critical for aerial photogrammetric surveys, particularly for direct georeferencing. The performance of the Position and Orientation System (POS), in particular the orientation accuracy, is one of the most important factors in aerial photogrammetry specially when it is based on light airborne vehicles, including unmanned vehicles (UAV, Unmanned Aeral Vehicles). The low cost POS systems that are currently used in most of the light aerial vehicles, particularly in UAVs, have some weaknesses, such as the low accurate orientation, which is derived from the low accuracy MEMS IMUs (Micro-Electro-Mechanical System, Inertial Measurement Units). In this context, the exploration of the improvement of orientation accuracy of low cost POS, to provide equivalent performance as the high grade POS, is of utmost interest.

The accuracy of a POS can be improved by optimizing strategies of the integration system of GNSS and IMU, based on different coupling architectures, such as *loosely*, *tightly* or *deeply* coupled integration and proper filter configuration in Kalman Filter, and/or through incorporation of additional information, such as radar, odometer, terrain aiding, etc. In the last decade with the availability of cheaper high resolution cameras, other strategies are possible exploring the fusion of the measurements of GNSS, IMU and imagery to improve the accuracy of the POS. The availability of miniaturized sensors with enhanced capabilities and new methods for image processing together with the booming of light airborne platforms, for data acquisition, particularly in unmanned vehicles, opens a range of new possibilities for geodetic navigation applications, leveraging new developments in sensor fusion. Due to the limitation of payload capacity and power supply of the light aerial vehicles, an algorithm for a GNSS/MEMS-IMU was developed, in which it also integrates the information from images obtained by the camera attached to the system. This method has an advantage that, the improvement to the system is only depend on the design and appropriate configuration of the filter used in the algorithm, without introducing any additional devices.

In this work, a simple and cheap direct georeferencing system, consisting of a GNSS receiver, a low cost IMU and a small digital camera, for the use in light airborne platforms, was Implemented. Aiming at improving the orientation performance of this type of low cost system, which is designed to be used on light airborne vehicles, the research work presented in this

thesis focus on the following main aspects:

1) Validate the algorithms of aerial triangulation, direct georeferencing (forward intersection), and bundle adjustment for the photogrammetric survey with this system.

2) Validate the GNSS/MEMS-IMU integration navigation functions by applying a 15-state Kalman Filter, and prove the equivalence of the *loosely* and the *tightly* coupled Kalman Filter under the condition of good GNSS visibility.

3) Implement a GNSS/MEMS-IMU Kalman Filter augmented with the geometric information retrieved from consecutive images, as the precise relative orientation of consecutive images can be obtained using a SIFT/SFM (Scale-Invariant Feature Transform/Structure From Motion) matching algorithm. Incorporating this relative orientation information in the Kalman Filter improves the accuracy of the exterior orientation parameters.

4) Use a robust adaptive Kalman Filter, with the determination of the adaptive factor and the robust factor accomplished by the innovation information and the threshold value of the orientation changes between consecutive images respectively, to further improve the performance of the new method.

Results from real airborne tests were used to assess the performance of the method and confirm its efficiency. The results show that using a simple cheap camera, the solution of the orientation resulting from the integration of GNSS/IMU-MEMS can be improved significantly by about 60%, if the geometric information obtained from the images is introduced. An additional improvement can be obtained by applying a robust-adaptive-image Kalman Filter. The tests also show that the accuracy of the proposed method is dependent on the overlapping rate as well as the quality of the camera.

The system implemented guarantees a good quality orientation solution for photogrammetric applications using light aerial vehicles (including UAVs) with the advantage of being efficient and affordable. This type of approach can be further exploited for use in other types of applications, such as navigation in challenging environments.

Keywords: GNSS/MEMS-IMU/Imaging coupled navigation; POS; Direct georeferencing; Robust adaptive Kalman Filter; SFM/SFIT

Contents

List of tables

List of figures

List of abbreviations

AT	Aerial Triangulation
AO/FCUP	Observatório Astronómico do Prof. Manuel de Barros / Faculdade de Ciências da Universidade do Porto
APs	Application Programs
BBA	Bundle Block Adjustment
BDS	BeiDou Navigation Satellite System
C/A	Coarse/Acquisition
CCD	Charged Coupled devices
CDMA	Code Division Multiple Access
CODE	Center for Orbit Determination in Europe
DGS	Direct Georeferencing System
DOM	Digital Orthoimage Mosaic
DSM	Digital Surface Model
ECEF	Earth Center Earth Fixed
ECI	Earth Center Inertial
EGNOS	European Geostationary Navigation Overlay Service
ESA	European Space Agency
FDMA	Frequency Division Multiple Access
FOG	Fiber Optic Gyros

GCPs	Ground Control Points
GLONASS	GLObal'naya NAvigatsionnaya Sputnikovaya Sistema
GNSS	Global Navigation Satellites System
GPS	Global Positioning System
Hz	Hertz
IGS	International GNSS Service
IGSO	Inclined Geosynchronous Satellite Orbit
IMU	Inertial Measurement Unit
INS	Inertial Navigation System
InSAR	Synthetic Aperture Radar Interferometry
IRNSS	Indian Regional Navigation Satellite System
ISPRS	International Society for Photogrammetry and Remote Sensing
LC	Linear Combination
Lidar	Light Detection and Ranging
LRF	Laser Ranger Finder
MEMS	Micro-Electro-Mechanical System
MSF	Russian Military Space Forces
MTSAT	Multi-Functional Transport Satellite
PAF	Portuguese Air Force
PITVANT	Projecto de Investigação e Tecnologia em Veículos Aéreos Não-Tripulados
POS	Position and Orientation System
PPP	Precise Point Positioning
PRN	Pseudo-Random Noise

QZSS	Quasi-Zenith Satellite System
RNSS	Regional Navigation Satellite System
SAR	Search and Rescue Services
SBAS	Satellite Based Augmentation System
SIFT/SFM	Scale-invariant Feature Transform, Structure From Motion
SMU	Sensor Management Unit
SoL	Safety-of-Life
STD	Standard Deviation
WAAS	Wide Area Augmentation System

The cite sentences are writing in Italic.

1 Introduction

In order to describe the world perfectly, neoclassical artists represented by Leonardo Di Serpiero da Vinci pursued to painting the objects with special ideals and skills. The goal of this work is to use the geometric information to model the surface of the earth precisely. The tools that artists used included pencil, brush, and ink, while the tools in this work are GNSS (Global Navigation Satellites System), inertial systems, cameras, coordinates, and pixels. The methodologies used to develop this work involve different geomatics disciplines such as GNSS positioning, GNSS/INS (Inertial Navigation System) coupled navigation, Photogrammetry, as well as Mathematics, Computer vision, and Electronics.

GNSS has been the most outstanding positioning and timing tool since the eighties in the 20 century, with the features such as high accuracy, world-wide coverage, independent of atmospheric conditions, and low cost, which has been widely used in the areas of navigation, timing and geomatics, in the airborne, marine and terrestrial scenarios, both for military and civil purposes. Continuous and accurate GNSS positioning requires a good line of sight visibility of satellites, which makes it difficult to use the GNSS in urban areas, valleys and forests, in which the signals are easily blocked or degraded.

Unlike GNSS, INS is a dead reckoning and self-contained navigation system, used in navigation since the beginning of last century. Inertial systems are not dependent on exterior signals, and can therefore provide a position solutions in every environment, including underwater. An INS can provide continuous position and attitude outputs, and therefore becomes the complement or other navigation aiding source, namely during short term lack of GNSS. Besides, INS has the capacity of giving high rate positioning and attitude results, which can reach several hundred Hertz (Hz), much higher than GNSS (normally from 1 to 20 Hz). However, the drawback of INS is the time-dependent errors of the sensors, which grow fast with time, which means that without a timely correction the performance of an INS will be highly disturbed or even corrupted. Therefore, the integration of GNSS and INS can take the most of the advantages from both systems, and can provide a continuous, accurate, and high rate output of position and attitude solutions, which can be used in many practical applications besides navigation, the classic application, such as photogrammetry (Cramer *et al.* 2000, Cramer 2001, Gonçalves and Henriques 2015), strapdown gravimetry (Schwarz *et al.* 1993, Deurloo 2011, Ayres-Sampaio *et al.* 2015, Yan *et al.* 2016) or video photogrammetry (Madeira *et al.* 2014, Yan *et al.* 2017).

The word "photogrammetry" derives from three words: light, writing and measurement. In 1998, the congress of ISPRS (International Society for Photogrammetry and Remote Sensing), defined it as: *Photogrammetry is the art, science, and technology of obtaining reliable information and other physical objects from none-contact imaging and other sensor systems about the earth and its environment, and processes through recording, measuring, analyzing and representation*.

Photogrammetry relies on the extraction of the geometric information and its main task is to build the relationship between the pixels of the images and the corresponding objects of the world. This technology started in the fiftieth of the 20 century, and went through three stages, analog, analytic and digital, according to the medium types to restore the images, chemical films or digital code, as well as the projection models. Depending on the platforms used, Photogrammetry also can be classified as satellite photogrammetry, aerial photogrammetry, terrestrial photogrammetry, micro-range photogrammetry, and two-media photogrammetry.

Within this context, we are aiming to build a 3D geodetic model of the earth surface through the integration of like technologies of GNSS, INS, Photogrammetry and measurements from other devices. In this thesis, we focused on the exploration of low cost sensors, such as MEMS-IMU (Micro-Electro-Mechanical System, Inertial Measurement Unit) and consumer digital cameras, which were integrated to be strapped on a small light aerial vehicle, and designed in particular for UAV applications, in order to make the photogrammetric survey efficient and, at the sometime more affordable.

1.1 State of the art

Conventional photogrammetric surveys are based on the geometry relationship between the pixel coordinates and the real coordinates of the object, which need a certain amount of GCPs (Ground Control Points). For instance, in traditional aerial photogrammetry, it is a standard procedure to determine the exterior orientation parameters through the so-called Aerial Triangulation (AT) process. The exterior orientation parameters' quality is dependent on the quantity, distribution and precision of GCPs. High accuracy surveys for the establishment of GCPs involve a certain amount of field work, using for example, RTK GNSS surveying, and are therefore costly. Aerial Triangulation in a large scale mapping work needs even many GCPs. Moreover, in areas without man-made objects ground control point identification can be quite difficult and time consuming.

With the development of GNSS and INS, which can provide the exterior orientation parameters for the photogrammetric survey, reduction of the required GCPs can be considered (Tachibana *et al.* 2004, Madeira *et al.* 2014). The integration of GNSS and INS is named as **POS** (Position and Orientation System). Used together with a digital camera, which should be synchronized with the POS, makes a **DGS** (Direct Georeferencing System), which allows to transfer object data in the images immediately into a local or global coordinate system making further processing more efficient. For instance, in urban street mapping (Ellum and El-Sheimy 2002, Madeira *et al.* 2010), coastal monitoring (Madeira *et al.* 2013), forests monitoring (Hopkinson *et al.* 2013) and particularly in quick mapping of disaster areas (Hutton and Mostafa 2005, Mitishita *et al.* 2008). DGS allows a fast characterization of the actual situation, which is of utmost relevance. This has great advantages, especially in terms of cost and efficiency, in comparison with conventional photogrammetry methodologies.

DGS has two core parts: one is the POS and the other is the camera. The POS consists of a GNSS and a IMU. The POS is used for the estimation of the exterior orientation parameters and the camera is used for the acquisition of image information. Many time we see references that in the POS, the GNSS is providing the positions and the IMU is providing the orientations, which is not very precise, because both the results of position and orientation are provided by the integration of the GNSS and IMU.

IMUs are classified into different grades, mainly according to the stability of the inherent bias of the sensors output, normally based on the gyro bias (Jekeli 2001b), or also on the type of applications they are mostly used. Table 1-1 indicates the typical performance of the actual different IMUs grades.

Table 1-1 Performance characteristics of inertial navigation systems (Jekeli 2001b, Hewitson 2006)

sensors	performance parameters	Grade			
		Consumer (MEMS)	Tactical	Navigation	Military
gyroscope	bias °/hr	> 10	1.0-10	0.0001-1.0	< 0.0001
	scale factor ppm	> 500	200-500	1-200	< 50
	random walk °/sqrt(hr)	-	0.2-0.5	0.002-0.2	-
accelerometer	bias μg	> 500	200-500	1-200	< 10
	scale factor *ppm*	> 1000	400-1000	1-400	< 2
	random walk μg/hr/sqrt(Hz)	-	200-400	5-200	-

From this table we can see that, from the Consumer to the Military applications, the accuracy of the sensors are better and better, and the prices are also becoming higher, from several Euros to millions Euros. The correct specification of the IMU errors is essential to the final GNSS/INS solution quality, and the full error specification includes systematic and random errors, such as initial alignment error, gravity modelling error and linearization error.

There are several commercial POS products that have been brought to market. Since 2002, the PASCO Corporation (now belonging to Trimble) has introduced APPLANIX POS/AV for airborne and terrestrial applications which is combined with high resolution aerial cameras. The company IGI has brought out the AEROcontrol, which consists of an Inertial Measurement Unit based on Fiber Optic Gyros (FOG) and a Sensor Management Unit (SMU) with an integrated high end GNSS receiver. The attitude accuracy of these commercial POS can achieve a few hundredth to thousandth degrees, with a position accuracy from several centimeters to a few decimeters (Kremer and Kruck 2003, Scholten *et al.* 2003). Those advanced POS, which are using high grade IMUs, integrated with high quality cameras/scanners, have the ability to provide products with high level of accuracy, but with the disadvantage of being very expensive (normally more than 100 thousand Euros). These commercial POS achieving accurate exterior orientation parameters for aerial photogrammetric surveys, relying on the use of tactical or navigation grade IMUs (either with laser or fiber optics gyros). These precision manufacturing IMUs are expensive and delicate, and need to be handled carefully and set safely. These high grade IMUs normally are mounted within stable aerial manned vehicles, which means normal sized airplanes that have conditions (space and power) adequate to carry these sensors.

Modern MEMS technology makes it possible to burn a complete inertial unit on an electro chip. The MEMS IMU is characterized by quick boot, low power consumption, compact and quite low-cost. This functional chip is already being used in more and more applications, such as navigation, camera calibration, and even the smartphones have a small unit inside. Compared with the Laser/Fiber IMUs, the MEMS IMUs have a much higher level of noises, such as constant bias and random walk calibration error, temperature error, etc. (Flenniken *et al.* 2005, Woodman 2007), which grow proportionally to the time, and can reach a high level within a short period if there is no exterior correction (Collin *et al.* 2001). These may lead to quite low quality position and orientation solutions, and therefore degrade the quality of an aerial photogrammetry survey.

These type of IMUs are acquiring a growing relevance due to the potential of their application in remote sensing from light airborne platforms, namely UAVs, whose market is booming. This kind of low cost POS can provide the exterior orientation parameters for aerial triangulation or direct geo-referencing, and has already been implemented in different applications, such as forestry and agriculture (Grenzdörffer *et al*. 2008), and low altitude photogrammetry (Jang 2004, Haarbrink 2006, Zongjian 2008, Eisenbeiß 2009). However, the accuracy of these exterior orientation parameters provided by the low cost POS is not enough to obtain precise photogrammetric products, mainly because of the limited performance of the low cost IMUs.

Some commercial low cost IMUs also have been brought to market, such as Xsens MTi-G, Advanced Navigation Spatial and VectorNav NV-200. The costs of those products normally range from 1,500 to 2,500 Euros, and can provide moderate accurate orientation output based on the use of thermal compensation model of the sensors and multi-antenna system, but with bad navigation performance (a few meters) since there are no geodetic GNSS receivers integrated (Xsens Technologies B.V. 2009, Advanced Navigation 2017, VectorNav 2017).

These IMUs can be mounted on an photogrammetric survey system, providing the aiding to the processing of the photogrammetry. There are several commercial small light photogrammetric systems, for examples, the UAV photogrammetry systems of the Topcon SIRIUS Pro, the Huace P310 and the DJI platform Pro. Table 1-2 gives details of these commercial UAV photogrammetric survey systems.

Table 1-2 Thee commercial UAV photogrammetric survey system

UAV	GNSS	IMU	total accuracy	approximate price €
Topcon SIRIUS	Geodetic	tactical	< 10 cm	130,000
Huace P310	Geodetic	MEMS	depend on the GCPs, camera quality and image overlap	50,000
DJI platform Pro	navigation	MEMS	depend on the GCPs, camera quality and image overlap	1,300

Topcon SIRIUS UAV is already a sophisticated DGS, which involves a geodetic GNSS receiver, a tactical IMU, and a high quality camera, allowing an excellent accuracy (10 cm) of the DG products. However, it is an expensive photogrammetric system. The other UAVs don't have high grade IMUs, therefore they are not DGS, and the accuracy is still depending on the availability of GCPs, camera quality and image overlap.

This situation raised the idea to improve the integration of the GNSS and low cost MEMS IMU, to obtain the equivalent performance of the high grade POS, which can significantly reduce the cost of the aerial photogrammetric survey system, since the high grade IMU takes the most cost of DGS.

Several works show that the accuracy of a GNSS/IMU system can be improved by optimizing the integration method, exploiting different coupling strategies (*loosely*/*tightly*/*deeply*) and proper filtering (Yang 2008, Schmidt and Phillips 2011, Liu *et al.* 2016, Watson *et al.* 2016, Xia *et al.* 2016), and/or incorporating additional information from other sensors such as: multi-antenna

(Tomé 2002, Dorn *et al.* 2016), radar, odometer (Quist and Beard 2016), terrain aiding, CCD (Charged Coupled devices) video camera and LRF (Laser Ranger Finder) (Wang *et al.* 2008, Chu *et al.* 2012). Some of these methods have great potential to estimate the relative movement of a mobile platform during GNSS signals blockage (Wang *et al.* 2008, Chu *et al.* 2012, Won *et al.* 2014).

GNSS/IMU and images fusion provides an optional method to improve the final accuracy of the position and orientation of a moving platform. For instance the sequential aerial triangulation method using the high correlated images can produce accurate results for low cost airborne applications (Choi and Lee 2013). This strategy is ideal for the small light aerial photogrammetric survey works, since the airborne vehicle has limited payload capacity and power supply restrictions.

Previous research on classical navigation strategies based on vision sensors, on the fact that the image sequences can be taken as additional self-contained spatial measurements which complement the GNSS/IMU information when there are GNSS data gaps. Relative position, velocity, and attitude can be retrieved from the image sequences, and can be used to correct the vehicle's navigation parameters when GNSS fails (Winkler *et al.* 2004, Wang *et al.* 2008, Chu *et al.* 2012). Several of these works refer to positioning accuracies of the order of a few meters (Wang *et al.* 2008, Chu *et al.* 2012, Won *et al.* 2014), and to an accuracy of the yaw angle of the order of several degrees, by comparing with the true trajectory (Chu *et al.* 2012), such accuracies do not meet the demand of precise geodetic navigation. Very few researches are focused on the improvement of the orientation accuracy given by low cost sensors. The study of Nagai *et al* (2009) shows that precise exterior parameters can be obtained by the integration of GNSS, IMU and the exterior orientations retrieved from the BBA (Bundle Block Adjustment), however, this work is still based on the high grade POS and high quality cameras, and without the high grade IMU, it is difficult to get satisfactory exterior orientation parameters.

In general, the orientation performance is very relevant for aerial photogrammetric applications, especially those supported in light airborne platforms.

1.2 Motivation

Since more than one decade, the AO/FCUP (Observatório Astronómico do Prof. Manuel de Barros / Faculdade de Ciências da Universidade do Porto) group has been focused on the implementation of low-cost systems based on the integration of GPS and inertial measurements for use in different types of platforms (airborne and terrestrial) and applications (Tomé 2002, Deurloo 2011, Madeira *et al.* 2014, Yan *et al.* 2017).

In the scope of this thesis, a **low cost DGS** was developed, which integrates a GNSS/a MEMS-IMU (POS) and a digital camera, with other accessories. Such a system can have a total weight of less than 5 kg, with a cost less than 2,500 Euros. It is a small light system, which is more flexible and affordable than the traditional aerial photogrammetric systems.

In this research, we seek for possible methodologies to significantly improve the weak performance of a low cost POS, without introducing additional loads to the airborne platform. The first choice was to use the information retrieved from the analysis of two consecutive images acquired from an on-board camera, processed using the SIFT/SFM (Scale-invariant Feature Transform, Structure From Motion) method, which can provide a rigorous relative geometric orientation (Lowe 1999, Lowe 2004, Snavely *et al.* 2008, Furukawa and Ponce 2010) and has a great potential as an argument in the GNSS/IMU integration system.

Our aim is to improve the orientation performance of a low-cost POS for aerial photogrammetry, which is using small light airborne vehicles. In this kind of application, GNSS outages are rare, and the images are exploited in view to improve the orientation parameters of the airborne platform and, consequently, the accuracy of the 3D information obtained from the photogrammetric survey without ground control points. The research work focus on the following three main aspects:

1) Develop a low cost POS with GNSS, MEMS-IMU, and low-cost camera. Validate the basic functions of aerial triangulation, direct georeferencing (forward intersection), and bundle adjustment method for optical aerial photogrammetry.

2) Validate the GNSS/MEMS-IMU integration navigation functions by applying a 15-state Kalman Filter, and by proving the equivalence of loosely and tightly Coupled Kalman Filter under the condition of good GNSS observation scenario, which lead to the decision of choosing the loosely coupled strategy for the airborne application in this thesis.

3) Implement a new GNSS/INS robust adaptive Kalman Filter augmented with the geometric information retrieved from consecutive images, which improve the orientation accuracy of the POS significantly.

1.3 Objective and main contributions of this thesis

The main objective of this thesis is to obtain better quality exterior orientation parameters with a low cost POS by integrating the image matching techniques and the navigation data, totally, or tightly, independent from the ground control points. To achieve that goal, improvement of a low cost POS was attempted through the implementation of a modified coupled Kalman Filter using a multi-sensor approach that integrates different types of data: GNSS, MEMS-IMUs and images from low cost cameras, which could be mounted in a small light aerial vehicle.

Main contribution of this thesis is therefore the implementation of a more affordable system methodology for airborne mapping without control points, while guaranteeing precision levels similar to those achieved with higher grade POS. One important aspect is that this approach should be also suitable for UAV applications. Exploiting MEMS IMUs for photogrammetry, trying to achieve equivalent performance as with higher grade IMUs, has the potential for a great reduction of the cost of airborne photogrammetry while the operation of these systems will be simplified because of the characteristics of the MEMS IMUs. This will facilitate the production of photogrammetric surveys in some blind areas. Blind area here means the places unable or difficult to reach, like some shelter areas, such as the urban zones, valleys, and also refer to some isolated areas, such as the earth disaster environments, and small islands. The results obtained in this research show that the cost of both the aerial (IMU and airplane) and the terrain (ground control points) will be decreased, making precise aerial photogrammetry more affordable.

1.4 Thesis outline

After this introduction chapter, chapter 2 gives a brief review to actual GNSS scenario, the GNSS measurements and the principle of the standard GNSS positioning and precise positioning.

Chapter 3 presents the details of the POS systems, and the algorithms of the backward intersection, forward intersection, and bundle adjustment of photogrammetry, and a practical test using a commercial software which was used to validate the solutions from the algorithm developed in this thesis.

Chapter 4 gives the introduction to theory and algorithm of the Kalman Filter and then discusses the loosely and tightly coupled strategies in detail. The inertial mechanical navigation equations and the process of the applying of the GNSS/IMU Kalman Filter are also described in this chapter.

Chapter 5 gives the prove process of the equivalence of the loosely and tightly coupled strategies under the condition of good GNSS observation scenario; proposes a GNSS/MEMS-IMU/Imaging coupled Kalman Fitlter, and the image-robust-adaptive methodology developed is presented. All of these developments incorporate original and new research that goes beyond the state of the art. Measurements from the tests were used to show the equivalence of the loosely and tightly coupled strategies, then the GNSS/MEMS-IMU, GNSS/MEMS-IMU/Imaging and the image-robust-adaptive Kalman Filters are presented.

Chapter 6 presents the results from real airborne tests in different places in Portugal, which were used to validate the described algorithms and the software program developed. Results are analyzed and discussed.

Chapter 7 presents the main conclusions of this thesis and suggestions for future studies.

2 Global navigation satellite systems

A Global Navigation Satellite System can provide precise, continuous, and reliable solutions for position and velocity that enables many of the applications that we use in our daily lives, and it is also one of the key parts of a POS. In this chapter, a summary of the principles and technology for GNSS positioning and velocity determination is presented. In the this thesis, only the references to the actual status of the GNSS is made and, using GPS as an example, the basic algorithms for GNSS satellite positioning and velocity estimation are described briefly.

2.1 GNSS overview

A GNSS system includes 3 components: space segment, control segment, and user segment. Fig. 2-1 illustrates the GNSS system components. The space segment refers mainly to the satellites, which transmit the ranging signals and navigation messages. The control segment includes the control and monitoring stations, which are responsible for tracking satellites to provide orbit and clock corrections. The user segment refers to our GNSS receivers, which go from a geodetic-grade receiver to a cheap navigation receiver, or even a simple chip inside a smartphone.

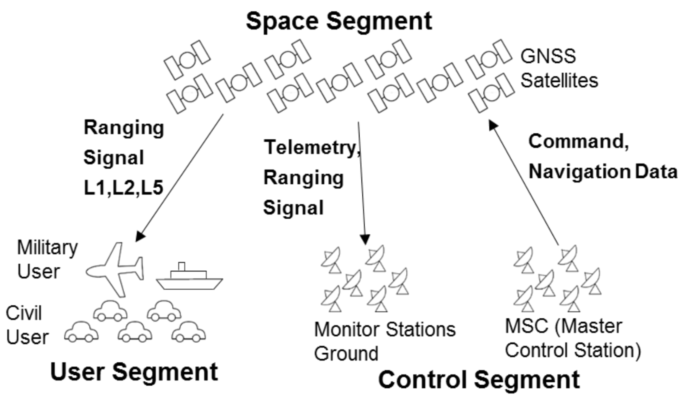

Fig. 2-1 GNSS system segments (Parkinson and Spilker 1996, Takasu 2013).

The most well-known GNSS operating worldwide is GPS (Global Positioning System). Other GNSS are GLONASS (GLObal'naya NAvigatsionnaya Sputnikovaya Sistema), Galileo and BDS (BeiDou Navigation Satellite System). The first GPS satellite was launched February, 1978 by the USA military, which marked the beginning of the GNSS era. Then in 1982 the Russian GLONASS constellation, operated by the Russian Military Space Forces (MSF), started to be implemented. Galileo is the GNSS that was created by the European Space Agency (ESA), the European Commission and Eurocontrol. The first Galileo satellite was launched on 28 December 2005, and the complete constellation, with 30 satellites, is planned to be fully implemented by 2020. China BDS consists of a limited test system and a full scale global navigation system. The first BDS satellite Beidou-1A was launched in October 2000 by China military, and is scheduled to be a global navigation system by 2020. After four decades of development, the GNSS has become an irreplaceable tool for positioning and navigation, not only for the military but also for the civilian, with many everyday life applications.

2.1.1 GPS

GPS is the most well-known navigation system, and the word “GPS” has been taken as synonym of the GNSS and been well known to public for many years. GPS was designed to be used by both military and civilian. Fig. 2-2 is an overview of the GPS constellation: at least 24 satellites in 6 orbital planes, 4 satellites in each plane, at an altitude of 20,200 km with 55 degree inclination. The U.S Air Force has launched more than 30 GPS satellites till the first quarter of 2017, 31 of which are operational.

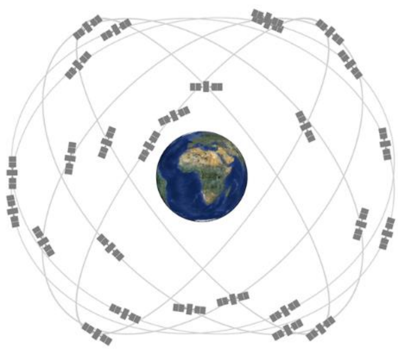

Fig. 2-2 Global Positioning System (U.S. Air Force website 2017).

GPS signals started to be broadcasted on two carrier frequencies: L1 1575.42 MHz (wavelength 19 cm) and L2 1227.60 MHz (wavelength 24.4 cm). The technology of CDMA (Code Division Multiple Access), in which all satellites use the same frequency, is used to transmit the signals. Each satellite has a unique PRN (Pseudo-Random Noise) code, and the satellites can be distinguished by its code when the GNSS receiver tracks the signals (Parkinson and Spilker 1996, Kaplan and Hegarty 2005, Dach 2015). There are two types of PRN codes also named “ranging codes”: a C/A (Coarse/Acquisition) code and a P (precise) code. C/A code is for civil use and it is modulated on the L1 frequency, while the P code is transmitted on the both L1 and L2 frequencies.

GPS modernization is an ongoing program that aims to upgrade the Global Positioning System with new, advanced capabilities to meet growing military, civil, and commercial needs, adding an additional L5 frequency, at 1176.45 MHz, and new ranging codes on the different carrier frequencies, generating new civil signals L1C, L2C and L5C, and the military M code (Parkinson and Spilker 1996, Kaplan and Hegarty 2005, Dach 2015). It was started in 2005 when the first GPS IIR-M satellite was put in operation. In December 2010 there were 9 GPS satellites broadcasting L2C (PRN01, 05, 07, 12, 15, 17, 25, 29, 31). The third civil signal, L5C, was implemented in the Block IIF satellites, which started to be launched in May 2010, and the last one was launched in February 2016. The fourth civil signal, L1C, was designed to enable interoperability between GPS and other satellite navigation systems, and is provided by Block III satellites, which are scheduled for launch at the beginning of 2018 (Subirana *et al.* 2013).

2.1.2 GLONASS

GLONASS is the Russian equivalent of GPS, which was also designed for military and civilian users. Fig. 2-3 is an overview of the GLONASS constellation: The satellite constellation is at an altitude of 19,390 km, and on inclination of 64.8 degree with almost 3 circular orbits, and 8 satellites in each orbit. Actually, 27 satellites are in orbit, 24 of which are operational. Due to its inclination, GLONASS has a better visibility at high latitudes.

Fig. 2-3 GLONASS constellation (Russia Space System website 2017).

GLONASS also started to broadcast signals on two carrier frequencies of the L band: L1 centered at 1602.00 MHz (wavelength 18.7 cm), and L2 centered at 1246.00 MHz (wavelength 24.1 cm). GLONASS uses FDMA (Frequency Division Multiple Access) technology to broadcast the signals, which means that all GLONASS satellites use the same PRN code, but each satellite has a unique carrier frequency (Parkinson and Spilker 1996, Kaplan and Hegarty 2005, Dach 2015).

GLONASS modernization was planned to broadcast a new third carrier frequency G3 at

1202.025 MHz (wavelength 25.0 cm), using the new GLONASS-k satellites, which started to be launched in February 2011, and the last one was launched in November 2014. This signal provides a new civil C/A2 and military P2 codes, and is especially suitable for SoL (Safety-of-Life) applications (Parkinson and Spilker 1996, Kaplan and Hegarty 2005, Dach 2015). The change to the CDMA protocol, instead of FDMA was initiated with the GLONASS-K, providing CDMA signals at the G3 frequency, in the L3 band (close to the Galileo E5b carrier) (Kaplan and Hegarty 2005, Subirana *et al.* 2013, Dach 2015), this aims also at augmenting GLONASS interoperability. A modernized GLONASS-K satellite, plaining to be launched, also transmit on the L5 frequency at 1176.45 MHz, the same as the modernized GPS signal L5 and Galileo signal E5a.

2.1.3 Galileo

Galileo is a joint program of the European Commission and the European Space Agency, its purpose is to implement a satellite navigation and timing system under civilian control, independent from none-European navigation systems, to promote the benefit of space for society and the EU economy, to provide integrity services and support for Search and Rescue (SAR) Services. Fig. 2-4 is an overview of the Galileo constellation: there are 3 orbit planes, at the altitude of 23,222 km with an inclination of 59 degree, and 8 satellites were designed in each plane (Kaplan and Hegarty 2005, Dach 2015). On 15th, December 2016 it was announced that Galileo start to provide position service globally. At present, there are 18 Galileo satellites in orbit, and the system will by fully developed by 2020.

Fig. 2-4 Galileo constellation (European GNSS Service Centre Websites 2017)

Similar to GPS, Galileo uses CDMA technology to transmit the signals. Galileo transmits 10 different navigation signals on four signal bands: E5a (1176.450 MHz), E5b (1207.140 MHz), E6 (1278.750 MHz), and E1(1575.420 MHz), which are internationally allocated for radio navigation satellite services (RNSS), allowing the combination of information from both the GPS and Galileo systems, to let the user receiver achieve better performance than employing either system separately (Kaplan and Hegarty 2005, Subirana *et al.* 2013, Dach 2015).

2.1.4 BDS

Similar to GLONASS and Galileo, China BDS is a program that was designed for lowering or removing the dependence on the GNSS from other countries. Fig. 2-5 is an overview of the BDS constellation. For the designed full operation system, there are five Geostationary Earth Orbit satellites, twenty-seven Medium Earth Orbit satellites and three Inclined Geosynchronous Satellite Orbit satellites (Beidou Navigation Office 2016). The GEO satellites are operating in orbit at an altitude of 35,786 km and positioned at 58.75°E, 80°E, 110.5°E, 140°E and 160°E respectively, and the MEO satellites are operating in orbit at an altitude of 21,528 km and an inclination of 55° to the equatorial plane. The IGSO (Inclined Geosynchronous Satellite Orbit) satellites are operating in orbit at an altitude of 35,786 km and an inclination of 55° to the equatorial plane (Beidou Navigation Office 2016). The first BDS satellite was launched in 2000, and the designed number of satellite is 35. Ten satellites became operational in December 2011, and till 12th, June 2016, 32 satellites have been launched into space, and the system will by fully developed by 2020.

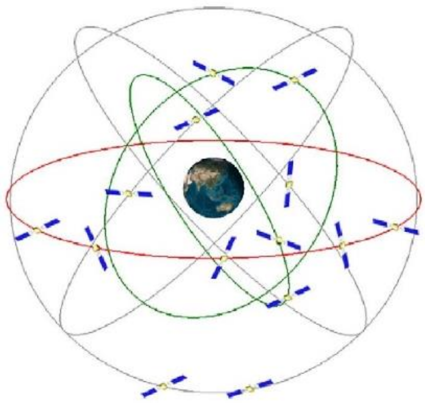

Fig. 2-5 BDS constellation (Beidou Navigation Office website 2017).

Like GPS, Galileo and the modernized GLONASS signals, BDS uses CDMA technology to transmit the signals. BDS phase II/III satellites are designed to transmit three radio frequencies in L band, B1 (1561.098 MHz in BDS II and 1575.42MHz in BDS III), B2 (1207.14 MHz in BDS II and 1191.795 MHz in BDS III), B3 (1268.52 MHz in BDS II and 1268.52 MHz in BDS III) bands (Parkinson and Spilker 1996, Kaplan and Hegarty 2005, Dach 2015), this aims also guarantee the ability of BDS interoperability

Besides these global satellite navigation systems, there are several regional Satellite Based

Augmentation Systems (SBAS), such as the American Wide Area Augmentation System (WAAS, 3 commercial geostationary satellites) (Kaplan and Hegarty 2005), the European Geostationary Navigation Overlay Service (EGNOS, 3 geostationary satellites) and the Japanese Multi-Functional Transport Satellite (MTSAT, 2 geostationary satellites), etc. There are also some Regional Navigation Satellite System (RNSS), such as the Japanese Quasi-Zenith Satellite System (QZSS, 4 satellites), the Indian Regional Navigation Satellite System (IRNSS, 7 satellites), contributing to improve the positioning and timing services for the general public in the respective regions.

The research in this thesis was intended to rely on multi-GNSS positioning, however, due to the delays in the implementation of Galileo and BDS, and to the protocol used by GLONASS, the measurements used in the time frame of this work were only GPS. For that reason we give a brief overview of GPS measurements, and process models, as they were used to get the estimation of position and velocity to feed GNSS/IMU filter for application to photogrammetry.

The construction of GNSS systems has become an important policy for many countries, because they not only support military applications, but mostly due to the importance for civilian use. In the future it might be expected that not only the existing GPS, GLONASS, and the newly launched BDS and Galileo, continue to be updated but also other new GNSS systems may be implemented. In principle, the more GNSS satellites observed, the more reliable the positioning will be.

2.2 Measurement models

As discussed in the previous section, the GNSS space segment is responsible for transmitting the ranging signals and navigation messages. In this section, taking GPS as an example, the signals structure and observations models, and the correction model for the main errors of the GPS observations are introduced.

The GNSS signals have a type of modulation wave as shown in Fig. 2-6. Three type of measurements can be retrieved from the GNSS signals: the code pseudo-range, the carrier phase, and the Doppler observation.

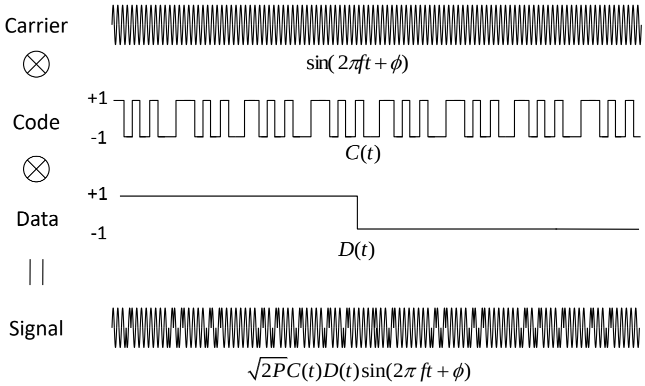

Fig. 2-6 GNSS signal structure (Parkinson and Spilker 1996, Takasu 2013).

Pseudo-range observation, defined as the time difference between satellite transmission time and the user receiving time, multiplied by the light speed in vacuum, can be referred to the C/A or the P code. The observation of the pseudo-range in error free condition can be written as:

$$P_r^k = c\left(\overline{t}_r - \overline{t}^k\right) \tag{2-1}$$

where, $\overline{t}_r$ is the signal reception time measured by the receiver clock, $\overline{t}^k$ is the signal transmission time given by the satellite clock, P_r^k is the true distance between the satellite and the GNSS receiver, and c is the light speed in vacuum.

When the GNSS signal travels from satellite to receiver, there are different factors that contribute to disturb the signal, such as the ionosphere, the troposphere and multipath, as represented schematically in Fig. 2-7.

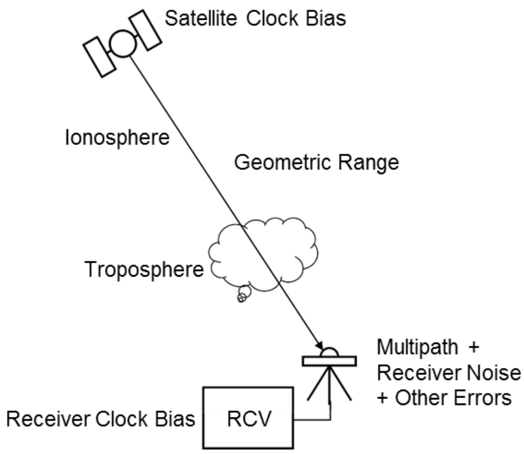

Fig. 2-7 The travel of the GNSS signal (Parkinson and Spilker 1996, Takasu 2013).

The pseudo-range observation, considering just the main errors that affect the measurements, can be expressed as:

$$\begin{aligned} P_r^k &= c\left[(t_r + dt_r) - (t^k + dt^k)\right] + \eta \\ &= c\left(t_r - t^k\right) + c\left(dt_r - dt^k\right) + \eta \\ &= \rho_r^k + c\left(dt_r - dt^k\right) + T_r^k + I_r^k + \delta d_{multi} + \eta \end{aligned} \tag{2-2}$$

where, dt_r is the receiver clock error, dt^k is the satellite clock error, T_i^k represents the elevation-dependent tropospheric error, I_r^k is the frequency-dependent ionospheric error, δd_{muti} is the multipath error and η refers to the residual errors.

The pseudo-range observation is typically given in meters. The positioning accuracy using the pseudo-range observation can reach a few meters. In the GPS case, the measurement accuracy of the P code is around 0.3 m, while the C/A code is 3~4 m, and the positioning accuracy using the combination of P code and C/A code is around 2~3 m in horizontal direction, and 5 m in vertical.

The carrier-phase is a measurement on the beat frequency between the received carrier of the satellite signal and a receiver-generated reference frequency (Parkinson and Spilker 1996, Gurtner 2007). The phase range can be obtained by multiplying the carrier-phase and the carrier wavelength λ, given in m. Similar to Equation (2-2), the carrier-phase observation can be expressed as (Parkinson and Spilker 1996, Kaplan and Hegarty 2005, Takasu 2013, Dach 2015):

$$\begin{aligned} \Phi_r^k &= \lambda_i \phi_r^k \\ &= \lambda_i\left[\phi_r(t_r) - \phi^k(t^s) + N_r^k + \varepsilon_\phi\right] \\ &= c(t_r - t^k) + c(dt_r - dt^k) + \lambda_i N_r^k + \lambda\varepsilon_\phi \\ &= \rho_r^k + c\left(dt_r - dt^k\right) - I_r^k + T_r^k + \lambda_i N_r^k + \varepsilon_\Phi \end{aligned} \tag{2-3}$$

where, $\phi_r(t)$ is the phase (cycle) of receiver local oscillator and $\phi^k(t)$ is the phase (cycle) of the transmitted navigation signal at the time t, N^k is the carrier-phase integer ambiguity.

There are ambiguities in the carrier phase as Equation (2-3) shows. To use the carrier phase observation to do the calculation of the position, the integer ambiguities need to be estimated correctly. The most common method to resolve the ambiguities problem is the LAMBDA method, which uses a Z-transformation to de-correlate the ambiguities, and the integer minimization problem is then attacked by a discrete search over an ellipsoidal region (Parkinson and Spilker 1996, Kaplan and Hegarty 2005, Takasu 2013, Dach 2015).

The quick strategy of integer ambiguities is still a hot topic at the area of GNSS solution, because the more precise and quick the solution of the integer ambiguities is, the more accurate position results will be.

The phase can be used to obtain the satellite-receiver distance with an accuracy of a few centimeters, as the accuracy of the GPS carrier phase determination is around a few millimeter, and the resulting positioning accuracy using the GPS carrier phase can reach the centimeter level or even better.

The Doppler measurement is defined as the time derivative of the carrier phase and gives the frequency shift caused by the relative receiver-satellite motion (Parkinson and Spilker 1996, Kaplan and Hegarty 2005, Dach 2015). The unit for the Doppler measurement are Hz.

The classical Doppler equation, relating the observed and the transmitted frequencies is of the form (Parkinson and Spilker 1996, Kaplan and Hegarty 2005, Dach 2015):

$$f_r = f_t\left[1-\frac{1}{c}\left(v^k - v\right)\cdot\frac{r^k - r}{\left|r^k - r\right|}\right] \tag{2-4}$$

where, $r_s = (x^k, y^k, z^k)$ is the satellite position vector, $r = (x, y, z)$ is the receiver position vector, and $(v^k - v)$ is the relative velocity vector between the satellite and the receiver.

Then the Doppler shift can be obtained as (Parkinson and Spilker 1996, Kaplan and Hegarty 2005, Dach 2015):

$$\begin{aligned} f_r - f_t &= -\frac{f_t}{c}\left(v^k - v\right)\cdot\frac{r^k - r}{\left|r^k - r\right|} \\ &= -\frac{f_t}{c}\dot{\rho} \end{aligned} \tag{2-5}$$

where, the range rate $\dot{\rho}$ is the dot product of $\left(v^k - v\right)\cdot\frac{r^k - r}{\left|r^k - r\right|}$ which, if multiplied by the signal wavelength, can be written as (Parkinson and Spilker 1996, Kaplan and Hegarty 2005, Dach 2015):

$$\dot{\rho} = -\lambda\left(f_r - f\right) \tag{2-6}$$

Considering the effect of the receiver and satellite clock drift, the Doppler observation equation can be expressed as (Parkinson and Spilker 1996, Kaplan and Hegarty 2005, Dach 2015):

$$D_r^k = \dot{\rho}_r^k + cd\dot{t}_r - cd\dot{t}^k + \dot{\eta} \tag{2-7}$$

where, $\dot{\rho}_r^k$ is the satellite-receiver distance rate, $cd\dot{t}_r$ is the receiver clock shift, and $cd\dot{t}^k$ is the satellite clock shift.

The Doppler observation can be used to estimate the velocity, with an accuracy of a few cm/s.

As shown in the observation equations of (2-2), (2-3) and (2-7), there are several errors, such as the clock error of the GNSS satellite and user receiver, the tropospheric delay, the ionospheric delay, and the ambiguities, which influence the final accuracy of the estimation of position and velocity. Beside these errors, other factors, such as the corrections of the GNSS receiver and antenna, Earth Rotation Parameters, satellite orbit accuracy and ocean tide, also should be taken into account for the precise positioning applications. Here we will mainly discuss the satellite and receiver clock errors corrections, tropospheric and ionospheric delay correction using in this thesis.

Satellite clock error is the difference between the satellite internal clock and the reference GNSS time, and the receiver clock error refers to the difference between the receiver internal clock and the reference GNSS time.

The satellite clock error can be obtained from the precise clock files, and the accuracy, for GPS, can reach 0.075~0.1 nanoseconds (Dach 2015); The precise clock files are available after around two weeks. Broadcast ephemeris provides the satellite clock parameters, which are then used for the calculation of clock errors as (Parkinson and Spilker 1996, Kaplan and Hegarty 2005, Dach 2015):

$$\delta t = a_{f_0} + a_{f_1}\left(t - t_{oc}\right) + a_{f_2}\left(t - t_{oc}\right)^2 + \Delta t_{rel} \qquad \text{(2-8)}$$

where, a_{f_0} is the clock bias (s), a_{f_1} is the clock drift (s/s), a_{f_2} is the frequency drift (s/s), t_{oc} is the clock parameters reference epoch (s), t is the current epoch (s), the relativistic correction can be expressed as (in seconds):

$$\Delta t_{rel} = F \cdot ecc \cdot \sqrt{a}\sin\left(E\right) \qquad \text{(2-9)}$$

where, F = - 4.442807633 × 10^{10} s/m^2, ecc is the orbit eccentricity, $\sqrt{a}$ is the square root of the orbit semi-major axis, E is the eccentric anomaly of the satellite.

The satellite and receiver clock errors can be eliminated through the Double Difference method (Hofmann-Wellenhof *et al.* 2001), which will be referred in the next section.

For the removal of the ionospheric delay, the ionosphere-free combination, LC (linear combination) of the dual frequency observation of the carrier phase and the pseudo-range is commonly used. The ionosphere-free expressions of the pseudo-range and carrier phase observation can be written as (Parkinson and Spilker 1996, Kaplan and Hegarty 2005, Dach 2015):

$$P_{LC} = C_1 P_1 + C_2 P_2 \qquad \text{(2-10)}$$

$$\Phi_{LC} = C_1\Phi_1 + C_2\Phi_2 \tag{2-11}$$

where, C_1 and C_2 are the coefficients of the ionosphere free LC, and can be calculated as:

$$C_1 = \frac{f_1^2}{f_1^2 - f_2^2} \tag{2-12}$$

$$C_2 = \frac{-f_2^2}{f_1^2 - f_2^2} \tag{2-13}$$

where, f_1 and f_2 are the frequencies of the measurements.

The tropospheric delay can be estimated through an semi-empiric method, which normally is set by using the statistics of long term meteorological data on the ground. The tropospheric delay models used include: Hopfield, Saastamoinen, etc. (Parkinson and Spilker 1996, Kaplan and Hegarty 2005, Dach 2015). The tropospheric error in the Hopfield model can be expressed as (Parkinson and Spilker 1996, Kaplan and Hegarty 2005):

$$\begin{aligned}
T_r^k &= ZHD \bullet M_d(E) + ZWD \bullet M_w(E) \\
ZHD &= 155.2 \times 10^{-7} \frac{P_s}{T_s}(h_d - h_s) \\
ZWD &= 155.2 \times 10^{-7} \frac{4810}{T_s^2} e_s (h_w - h_s) \\
h_d &= 40136 + 148.72(T_s - 273.16)
\end{aligned} \tag{2-14}$$

where, P_s is the pressure in $mbar$; T_s is the temperature in $Kelvin$ degrees; e_s is the partial pressure of water vapor in $mbar$; h_s is the height of the station in m, and h_w =11000 m; M is the mapping function; E is the azimuth, units are expressed in radians.

The tropospheric error in the Saastamoinen model can be obtained as (Saastamoinen, 1972, Kaplan and Hegarty 2005, Dach 2015):

$$\begin{aligned}
T_r^k &= ZHD + ZWD \\
ZHD &= 0.0022767 \frac{P_s}{f(\varphi, h)} \\
WD &= 0.0022767 \frac{e_s}{f(\varphi, h)} \left(\frac{1225}{T_s} + 0.05\right) \\
f(\varphi, h) &= 1 - 0.00266 \cos 2\varphi - 0.00028H
\end{aligned} \tag{2-15}$$

where, φ is the latitude of the station in radians, and H is the ellipsoid height in km.

These critical errors in the GNSS measurements determinate the accuracy of the final positioning results, and must be corrected or estimated precisely to obtain reliable positions.

2.3 Position and velocity estimation using GPS

In this section, the principle of satellite positioning and velocity estimation is resumed exemplified for GPS. Identical procedures can be applied for the other GNSS systems as they are all based on similar principles and signals.

Table 2-1 The ephemeris products list (Dach 2015).

Orbit Type	Quality	Delay of Availability	Available at
Broadcast Orbits	~1 m	Real-time	Broadcast message
CODE Ultra Rapid Orbits	<5 cm	Real-time	CODE through FTP
CODE Rapid Orbits	<2.5 cm	After 12 hours	CODE through FTP
CODE Final Orbits	<2.5 cm	After 5–11 days	CODE, IGS Data Centers
IGS Ultra Rapid Orbit (pred)	~5 cm	Real-time	IGS Data Centers and CBIS
IGS Ultra Rapid Orbit (obs)	<3 cm	After 3 hours	IGS Data Centers and CBIS
IGS Rapid Orbit	<2.5 cm	After 17 hours	IGS Data Centers and CBIS
IGS Final Orbit	<2.5 cm	After ~13 days	IGS Data Centers and CBIS

CODE: Center for Orbit Determination in Europe. IGS: International GNSS Service.

As we know, we can get the information of satellite position and velocity from the broadcast ephemeris in real time or from precise ephemeris later in time. The broadcast ephemeris are updated every 6 hours, and the precision of the ephemeris degrades with time until the next update comes. The ultra-rapid precise ephemeris (e.g. CODE ultra and IGS ultra) can be obtained in almost real time, and the rapid precise product normally comes after 12 hours. The final precise products are available after two weeks. Table 2-1 summaries the quality and possible source for each type of ephemeris.

The GPS broadcast ephemeris presented in the navigation message, consists of the Keplerian elements and associated perturbation factors. We refer to Appendix A for details on the position and velocity estimations of the GPS satellites from the broadcast ephemeris. The sampling rate for the obtained precise ephemeris is 15 minutes, and for precise clock is 30 seconds, which needs to be interpolated to the epoch of the signal transmission. The Lagrange interpolation is one of the most widely adopted techniques for the ephemeris interpolation (Parkinson and Spilker 1996, Kaplan and Hegarty 2005, Dach 2015).

2.3.1 Standard position and velocity estimation

Standard position and velocity estimation means use the pseudo-range and Doppler observations to calculate the position and velocity of the receiver. Expanding Equation (2-2) in the first order yields (Parkinson and Spilker 1996, Kaplan and Hegarty 2005, Dach 2015):

$$P_i^k = \rho_{i0}^k + \frac{\partial P_i^k}{\partial x}\left(x - x_0\right) + \frac{\partial P_i^k}{\partial y}\left(y - y_0\right) + \frac{\partial P_i^k}{\partial z}\left(z - z_0\right) \quad (2\text{-}16)$$

where, i indicates the receiver, and k indicates the satellite, and the geometric range ρ_{i0}^{k} can be computed by:

$$\rho_{i0}^{k} = \sqrt{(x_{i0} - x^{k})^{2} + (y_{i0} - y^{k})^{2} + (z_{i0} - z^{k})^{2}} \qquad (2\text{-}17)$$

where, (x_{io}, y_{io}, z_{io}) are the initial coordinates of the receiver, and (x, y, z) are the coordinates of the k^{th} satellite obtained using the equations from Appendix A.

If substitute the Equation (2-16) into the simplified code pseudo-range equation (2-2), and use i, k to represent the i^{th} receiver and the k^{th} satellite, the equation becomes:

$$P_{i}^{k} - \rho_{i0}^{k} + cdt^{k} = a_{x_i}^{k} \Delta x_i + a_{y_i}^{k} \Delta y_i + a_{z_i}^{k} \Delta y_i + cdt_i \qquad (2\text{-}18)$$

or, using matrix notation with l representing the measurements:

$$\begin{aligned} l_{i}^{k} &= a_{x_i}^{k} dx_i + a_{y_i}^{k} dy_i + a_{z_i}^{k} dz_i + cdt_i \\ &= \begin{bmatrix} a_{x_i}^{k} & a_{y_i}^{k} & a_{z_i}^{k} & 1 \end{bmatrix} \begin{bmatrix} dx_i \\ dy_i \\ dz_i \\ cdt_i \end{bmatrix} \end{aligned} \qquad (2\text{-}19)$$

where, $a_{x_i}^{k} = \dfrac{dx_i^k}{\rho_{0,i}^{k}}$, $a_{y_i}^{k} = \dfrac{dy_i^k}{\rho_{0,i}^{k}}$, $a_{z_i}^{n} = \dfrac{dz_i^k}{\rho_{0,i}^{k}}$, and $dx_i^k = x_i - x^k$, $dy_i^k = y_i - y^k$, $dz_i^k = z_i - z^k$.

Similarly, for the Doppler measurement, we can expand the Equation (2-7) in first order Taylor series (Parkinson and Spilker 1996, Kaplan and Hegarty 2005, Dach 2015)::

$$\begin{aligned} D_i^k = \dot{\rho}_{i0}^{k} &+ \frac{\partial D_i^k}{\partial x}(x - x_0) + \frac{\partial D_i^k}{\partial y}(y - y_0) + \frac{\partial D_i^k}{\partial z}(z - z_0) + \\ &\frac{\partial D_i^k}{\partial v_x}(v_x - v_{x0}) + \frac{\partial D_i^k}{\partial v_y}(v_y - v_{y0}) + \frac{\partial D_i^k}{\partial v_z}(v_z - v_{z0}) \end{aligned} \qquad (2\text{-}20)$$

or:

$$\dot{l}_i^k = \dot{\rho}_{i0}^{k} + b_{x_i}^{k} dx + b_{y_i}^{k} dy + b_{z_i}^{k} dy + b_{vx_i}^{k} dv_x + b_{vy_i}^{k} dv_y + b_{vz_i}^{k} dv_z + e_{d,i}^{k} \qquad (2\text{-}21)$$

where,

$$b_{x_i}^{k} = \frac{dv_{x_i^k}}{\rho_{0,i}^{k}} + \frac{dx_i^k dv}{(\rho_{0,i}^{k})^3}, \quad b_{y_i}^{k} = \frac{dv_{y_i^k}}{\rho_{0,i}^{k}} + \frac{dy_i^k dv}{(\rho_{0,i}^{k})^3}, \quad b_{z_i}^{k} = \frac{dv_{z_i^k}}{\rho_{0,i}^{k}} + \frac{dz_i^k dv}{(\rho_{0,i}^{k})^3},$$

$$b_{v_{x_i}}^{k} = \frac{dx_i^k}{\rho_{0,i}^{k}}, \quad b_{v_{y_i}}^{k} = \frac{\Delta y_i^k}{\rho_{0,i}^{k}}, \quad b_{v_{z_i}}^{n} = \frac{\Delta z_i^k}{\rho_{0,i}^{k}},$$

$dv_{x_i^k} = v_{x,i} - v^k$, $dv_{y_i^k} = v_{y,i} - v^k$, $dv_{z_i^k} = v_{z,i} - v^k$, $\dot{\rho}_{i0}^k = \dfrac{dv}{\rho_{0,i}^k}$, and

$dv = dx_i^k dv_{x_i^k} + dy_i^k dv_{y_i^k} + dz_i^k dv_{z_i^k}$.

In a GPS standalone positioning and velocity estimation process, the measurement model of the code pseudo-range and Doppler observations can be defined by combining the pseudo-range and Doppler equations (2-19) and (2-21) together as (Parkinson and Spilker 1996, Kaplan and Hegarty 2005, Dach 2015):

$$\begin{cases} l_i^k = a_{x_i}^k dx + a_{y_i}^k dy + a_{z_i}^k dy + e_{l,i}^k \\ \dot{l}_i^k = b_{x_i}^k dx + b_{y_i}^k dy + b_{z_i}^k dy + b_{vx_i}^k dv_x + b_{vy_i}^k dv_y + b_{vz_i}^k dv_z + e_{d,i}^k \end{cases} \tag{2-22}$$

or in a detailed form as:

$$\begin{bmatrix} l_i^1 \\ l_i^2 \\ \vdots \\ l_i^n \\ \dot{l}_i^1 \\ \dot{l}_i^2 \\ \vdots \\ \dot{l}_i^n \end{bmatrix}_{2n\times 1} = \begin{bmatrix} a_{x_i}^1 & a_{y_i}^1 & a_{z_i}^1 & 0 & 0 & 0 \\ a_{x_i}^2 & a_{y_i}^2 & a_{z_i}^2 & 0 & 0 & 0 \\ \vdots & \vdots & \vdots & \vdots & \vdots & \vdots \\ a_{x_i}^n & a_{y_i}^n & a_{z_i}^n & 0 & 0 & 0 \\ b_{x_i}^1 & b_{y_i}^1 & b_{z_i}^1 & b_{v_{x_i}}^1 & b_{v_{y_i}}^1 & b_{v_{z_i}}^1 \\ b_{x_i}^2 & b_{y_i}^2 & b_{z_i}^2 & b_{v_{x_i}}^2 & b_{v_{y_i}}^2 & b_{v_{z_i}}^2 \\ \vdots & \vdots & \vdots & \vdots & \vdots & \vdots \\ b_{x_i}^n & b_{y_i}^n & b_{z_i}^n & b_{v_{x_i}}^n & b_{v_{y_i}}^n & b_{v_{z_i}}^n \end{bmatrix}_{2n\times 6} \begin{bmatrix} dx \\ dy \\ dz \\ dv_x \\ dv_y \\ dv_z \end{bmatrix}_{6\times 1} + \underset{2n\times 1}{e_i^k} \tag{2-23}$$

Then the equation (2-23) can be rewritten as:

$$\boldsymbol{L} = \boldsymbol{A\Delta X} + \boldsymbol{e} \tag{2-24}$$

The Least-Squares method is the most common estimation procedure in geomatics and the estimation of the unknown parameters is based purely on the measurements. The equation (2-24) can be solved by the Least-square method as resumed in Appendix B.

2.3.2 Precise positioning strategies

The most common strategies for precise positioning using the GPS signals are Differential Positioning and Precise Point Positioning (PPP). In a RTK (Real-time Kinematic) differential strategy, a known GNSS static reference station is used to provide corrections, such as tropospheric and ionospheric corrections, to the rover receiver. The observations, both of the reference station and the rover station, are combined together using certain mathematical models, in such a way that some errors, such as clock or ionospheric errors, can be substantially reduced or estimated. PPP strategy uses only one GNSS receiver to obtain precise coordinates, by including additional unknown parameters in the observation equations for the estimation.

There are different possibilities to combine observations from two stations (Parkinson and Spilker 1996, Subirana *et al.* 2013, Xu 2014), and the most widely used is the Double Difference strategy, which plays a very import role in minimizing the effect of clock errors, both of the satellites and receivers

Using Equation (2-2), the pseudo-range observation of the i^{th} reference station to k^{th} satellite can be written as:

$$P_i^k = \rho_i^k + c\delta t^k - c\delta t_i + T_i^k + I_i^k + \eta_i^k \tag{2-25}$$

similarly, for the j^{th} rover station we can write:

$$P_j^k = \rho_j^k + c\delta t^k - c\delta t_j + T_j^k + I_j^k + \eta_j^k \tag{2-26}$$

Differencing the equation (2-25) and (2-26) yields:

$$P_i^k - P_j^k = \rho_i^k - \rho_j^k + c\left(dt_i - dt_j\right) + \left(T_i^k - T_j^k\right) + \left(I_i^k - I_j^k\right) + \eta_{ij}^k \tag{2-27}$$

The satellite clock error in equation (2-25) and (2-26) has thus been eliminated through the double difference.

If the rover stations are close to the reference station, the effect of the troposphere and ionosphere in the GNSS signals are nearly identical. Therefore Equation (2-27) can be rewritten without the corresponding terms:

$$P_i^k - P_j^k = \rho_i^k - \rho_j^k + c\left(dt_i - dt_j\right) + \eta_{ij}^k \tag{2-28}$$

Similarly to Equation (2-28), the difference equation for the l^{th} satellite can be written as:

$$P_i^l - P_j^l = \rho_i^l - \rho_j^l + c\left(dt_i - dt_j\right) + \eta_{ij}^l \tag{2-29}$$

where, the satellite clock error is also eliminated. If we now take the difference of Equations (2-28) and (2-29), the double difference equation for receivers i and j, satellites k and l, can be obtained as:

$$\begin{aligned}\left(P_i^k - P_j^k\right) - \left(P_i^l - P_j^l\right) &= \left(\rho_i^k - \rho_j^k\right) - \left(\rho_i^l - \rho_j^l\right) + c\left(dt_i - dt_j\right) - c\left(dt_i - dt_j\right) + \eta_{ij}^{kl} \\ &= \left(\rho_i^k - \rho_j^k\right) - \left(\rho_i^l - \rho_j^l\right) + \eta_{ij}^{kl}\end{aligned} \tag{2-30}$$

where, the receiver clock errors have also been removed.

Similar to the standard position process we can use the equation (2-2) and (2-30), taking four satellite k, l, m, n into account, and form the double difference observation equations:

$$\begin{bmatrix} l_{ij}^{kl} \\ l_{ij}^{km} \\ l_{ij}^{kn} \end{bmatrix} = \begin{bmatrix} a_{x_j}^{l} - a_{x_j}^{k} & a_{y_j}^{l} - a_{y_j}^{k} & a_{z_j}^{l} - a_{z_j}^{k} \\ a_{x_j}^{m} - a_{x_j}^{k} & a_{y_j}^{m} - a_{y_j}^{k} & a_{z_j}^{m} - a_{z_j}^{k} \\ a_{x_j}^{n} - a_{x_j}^{k} & a_{y_j}^{n} - a_{y_j}^{k} & a_{z_j}^{n} - a_{z_j}^{k} \end{bmatrix} \begin{bmatrix} dx_j \\ dy_j \\ dz_j \end{bmatrix} \tag{2-31}$$

or in an abbreviate form as:

$$\boldsymbol{L} = \boldsymbol{A}\boldsymbol{\Delta x} \tag{2-32}$$

Using the Least-Square method, the solution of Equation (2-32) can be obtained by:

$$\boldsymbol{\Delta x} = \left(\boldsymbol{A}^{T}\boldsymbol{P}\boldsymbol{A}\right)^{-1}\boldsymbol{A}^{\mathrm{T}}\boldsymbol{P}\boldsymbol{L} \tag{2-33}$$

where, $\boldsymbol{P}$ is the weight matrix of the double difference of GNSS measurements and can be calculated as $\boldsymbol{P} = (\boldsymbol{V}_{DD})^{-1}$, where $\boldsymbol{V}_{DD}$ is the covariance matrix, that can be calculated as (Parkinson and Spilker 1996, Kaplan and Hegarty 2005, Dach 2015):

$$\boldsymbol{V}_{DD} = \boldsymbol{\sigma}^{2}\boldsymbol{B}_{DD}\boldsymbol{B}_{SD}\left(\boldsymbol{B}_{SD}\right)^{\mathrm{T}}\left(\boldsymbol{B}_{DD}\right)^{\mathrm{T}} \tag{2-34}$$

where, $\boldsymbol{\sigma}$ is the covariance matrix of the GNSS measurements and the matrices $\boldsymbol{B}_{DD}$ and $\boldsymbol{B}_{SD}$ are defined as:

$$\boldsymbol{B}_{SD} = \begin{bmatrix} 1 & -1 & 0 & 0 & \cdots \\ 0 & 0 & 1 & -1 & \cdots \\ 0 & 0 & 0 & 0 & \cdots \\ \vdots & \vdots & \vdots & \vdots & \ddots \end{bmatrix}, \text{ and } \boldsymbol{B}_{DD} = \begin{bmatrix} 1 & -1 & 0 & 0 & \cdots \\ 1 & 0 & -1 & 0 & \cdots \\ 1 & 0 & 0 & -1 & \cdots \\ \vdots & \vdots & \vdots & \vdots & \ddots \end{bmatrix}$$

The equations for the double difference strategy using the carrier phase observation have a similar structure as equation (2-31) to (2-34), but with the integer ambiguities items involved in. The solution of ambiguities is not discussed in detail in this thesis, as GPS processing is not our main focus, and they were completed by the open source software of “RTKLIB”. Details about resolving the ambiguities can be found in several articles and reference books such as (Parkinson and Spilker 1996, Kaplan and Hegarty 2005, Dach 2015).

Unlike the Double Difference strategy, the PPP method only needs observations from one GNSS receiver, using the precise ephemeris and clock products from IGS, CODE or other services, and accurate corrected model of antenna type, tropospheric delay, ocean tides, etc., to achieve precise positioning results. This method has the advantage of high efficiency, and becomes a good option to process the data from big GNSS networks.

In this thesis, we generally adopted the PPP strategy to process the GPS data based on the use of the open source software “RTKLIB”. Normally, the precise ephemeris and clock files from IGS were used, the elevation mask was set to 15°, the Ionosphere-free linear combination was used to correct the ionospheric delay, the Saastamoinen model was used to correct the tropospheric delay, and the LAMBDA method was applied to solve the integer ambiguities.

2.4 GNSS processing software

There are many GNSS processing software, commercial or academic source. Within the academic environments, the most famous are Bernese GNSS, GAMIT/GLOBALK and GIPSY-OASIS (GIPSY).

The Bernese GNSS Software is a scientific, high-precision, multi-GNSS data processing software developed at the Astronomical Institute of the University of Bern (AIUB) (Dach 2015), which supports both strategies of relative positioning and PPP. Bernese is a commercial software, which is being used by many universities and research institutes.

GAMIT/GLOBK was developed by MIT, Scripps Institution of Oceanography, and Harvard University with support from the National Science Foundation. GAMIT has a collection of programs to process phase data to estimate three-dimensional relative positions of ground stations and satellite orbits, atmospheric zenith delays, and earth orientation parameters. The software was designed to run under any UNIX operating system. GLOBK uses a Kalman filter whose primary purpose is to combine various geodetic solutions such as GPS, VLBI, and SLR experiments. It accepts as data, or "quasi-observations" the estimates and covariance matrices for station coordinates, earth-orientation parameters, orbital parameters, and source positions generated from the analysis of the primary observations (Herring *et al.* 2008). The core processing strategy of this software is Double difference. GAMIT/GLOBALK is free available for the none-commercial used worldwide.

GIPSY-OASIS **(**GIPSY) is a package for GNSS positioning and Orbit Analysis Simulation Software**,** which was developed by the Jet Propulsion Laboratory (JPL), and maintained by the Near Earth Tracking Applications and Systems groups. GIPSY supports multi satellite systems as GPS, GLONASS, DORIS, as well as Satellite Laser Ranging (SLR) . The core processing strategy of GPPSY is PPP. GIPSY is not an open-source software but it is possible to have it freely available for academic purposes.

There are also three other outstanding open source GNSS softwares that are very popular for the researchers, such as RTKLIB, GPS ToolKit (GPSTk) and GNSS-Lab (gLAB) .

RTKLIB consists of a portable program library and several APs (application programs) utilizing the library that was built in standard C languages. RTKLIB supports the GNSS data processing of GPS, GLONASS, Galileo, QZSS, BDS and SBAS, with both models of real-time and post-processing. RTLlib also support the proprietary messages from many GNSS receivers, like NovAtel, Trimble, Hemisphere, ublox, etc. (Takasu 2013).

GPS ToolKit is an open source library and suite of applications freely available, and it is a cross-platform resource, built via ISO-standard C++ programming language, that researchers can use to easily implement their own processing software (Salazar *et al.* 2010). The GPS ToolKit is sponsored by Space and Geophysics Laboratory, within the Applied Research Laboratories at the University of Texas at Austin. The GPS ToolKit includes a core library, auxiliary libraries, and executable applications, which provides a bundle of functions to solve the GNSS equations (Harris and Mach 2007, Salazar, et al. 2010).

GNSS-Lab is a software tool suite developed via ISO-standard C++ programming language, by the research group of Astronomy and Geomatics from the Universitat Politecnica de Catalunya (UPC) in the frame of an European Space Agency project, which is also an open-source and interactive educational multipurpose package to process and analyze GNSS data (Subirana *et al.* 2013). GNSS-Lab also supports the processing of the GNSS observations from GPS, Galileo and GLONASS, and includes both standalone and PPP strategies, and can be adapted to the standard formats of GNSS data.

All these software packages allow us to reach position accuracies of a few centimeters or even better.

There are also many excellent GNSS commercial processing software provided by the GNSS receiver manufacturers, such as the NovAtel waypoint software, Trimble Business Center. These commercial software are designed for the purpose of the geodetic survey engineering, and the accuracy can also reach the centimeter level.

In this thesis, we mainly used the RTKLIB software to obtain the precise kinematic GPS positions in our airborne tests.

3 Direct Geo-referencing

The development of the direct geo-referencing technique is reducing the cost of aerial triangulation, as it allows for reducing the number of GCPs, which makes the photogrammetric survey cheaper and more efficient than the conventional aerial triangulation. Here we are focus on the direct georeferencing system, whose core equipment includes a GNSS/INS integrated system and a remote sensor. This chapter is designed to give an introduction to photogrammetric surveys with GNSS/INS aiding. First, the principles of the photogrammetry are referred, such as backward/forward intersection, and the bundle adjustment. Then, the process of GNSS/INS aiding photogrammetry survey is explained in detail, particularly the relationship between the position and orientation defined in different frames as they are used in photogrammetry and navigation applications. At last, the direct georeferencing and the automatic matching methods for the image feature points, such as area based matching and SIFT/SFM methods, are introduced.

3.1 DGS overview

A typical Direct Georeferencing System is composed of GNSS/INS (POS), and Sensor. The position and orientation information are provided by the GNSS/INS integration, the cameras or other sensors, like Lidar (Light Detection and Ranging) and SAR/InSAR (Synthetic Aperture Radar Interferometry), measure the geometric relationship form the sensor to the mapped surface of the ground. The GNSS/INS and the sensors must be rigidly fixed with respect to each other, and relative position and attitude have to be measured or calibrated correctly. It is important to note that the dataset of the GNSS/INS and sensors must be synchronized to a unified time system, like UTC or GPS time. With the technique of extended aerial triangulation “ISO” (Integrated Sensor Orientation), which combines the advantages of conventional aerial triangulation and the direct measurement of the exterior orientation parameters, less or none GCPs are needed (Kremer and Kruck 2003).

IGI AEROcontrol and Applanix POS AV are the most common commercial POS worldwide. Fig. 3-1 is the overview of the IGI AEROcontrol POS system, which includes an IMU-IId, and a GNSS receiver, the post-processing software is AEROOffice. Fig. 3-2 shows the overview of the

Applanix POS AV, which includes the core IMU, GNSS receiver, and computer system (PCS), the post-processing software is POSpac. These fancy commercial POS products are mainly used at the applications of large to medium scale mapping works based on transport platform or other professional aerial platforms.

Fig. 3-1 IGI AEROcontrol.

Fig. 3-2 Applanix POS AV

With the development in technologies of GNSS, INS, sensors, and with the booming of the light small aerial platform, particular the UAVs, more and more DGS products are being brought in to the market, and the size is smaller, the cost is less, the manipulation method is easier, and the accuracy is becoming equivalent or even better sometimes than the existing ones. These new-coming light DGS products are mainly used at the large scale mapping works based on UAVs or other small light type aerial platforms.

3.2 Photogrammetry image processing

Within an image processing system, the image information can be expressed with pixel coordinates and the pixel gray values. The pixel coordinate system has the origin located at the top left corner, and the directions of x and y axis are right and down respectively. If the pixel size is known, coordinates (x_c, y_c) can be calculated by using the pixel coordinate multiplied by the pixel size. The image coordinate system in photogrammetry has normally a different definition: the origin is in the center of the image, and the direction of x and y axis are right and up, as shown in Fig. 3-3. The coordinates in photogrammetry definition can be calculated as:

$$\begin{cases} x = -\dfrac{1}{2}d_x + x_c \\ y = \quad \dfrac{1}{2}d_y - y_c \end{cases} \tag{3-1}$$

where, dx and dy mean the frame length of x-axis and y-axis of the images.

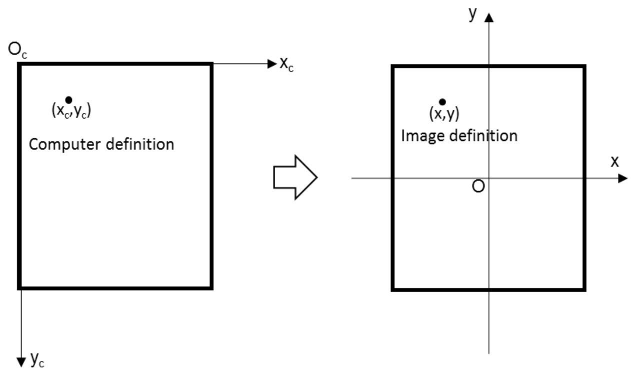

Fig. 3-3 the image coordinate system definition of computer and photogrammetry.

The photogrammetric treatment of image data requires the knowledge of the interior orientation parameters of the camera and the exterior orientation parameters of all images, or the relative and absolute orientation parameters of stereo-models. The interior orientation parameters refer to the position of the principal point in the image plane, (x_0, y_0), the focal length and the geometric distortions characteristic of the lens system. The principle point and the camera focal length is shown in Fig. 3-4.

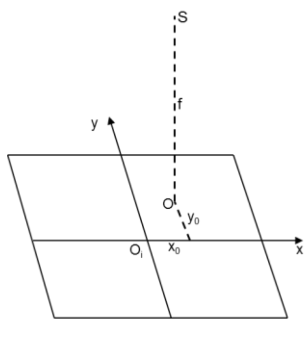

Fig. 3-4 The interior parameters.

The exterior orientation parameters are the absolute coordinates of the camera projection center, (X_s, Y_s, Z_s) and the orientation angle of the camera $(\omega, \varphi, \kappa)$ regarding the exposure instant.

One of the objectives of the photogrammetric work is using the geometric information in the images to rebuild the real position of the objects in the earth surface, the process can be explained as shown in Fig. 3-5.

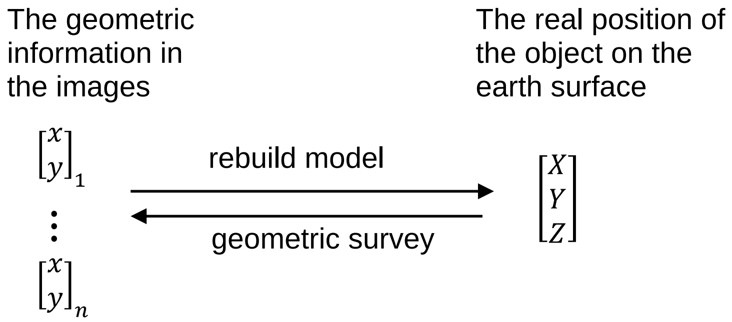

Fig. 3-5 the objective of the photogrammetry work.

We can build the geometric relationship between the real coordinates (X, Y, Z) of the point in the world and its image coordinates (x, y, z) at virtual photo coordinate system $S\text{-}xyz$, as “collinearity condition”, shown as in Fig. 3-6, and can be presented as (Luhmann *et al.* 2014, Wolf *et al.* 2014):

$$\frac{\upsilon}{X_A - X_s} = \frac{\nu}{Y_A - Y_s} = \frac{\omega}{Z_A - Z_s} = \frac{1}{\lambda} \tag{3-2}$$

or in another form as:

$$\begin{bmatrix} \upsilon \\ \nu \\ \omega \end{bmatrix} = \frac{1}{\lambda} \begin{bmatrix} X_A - X_s \\ Y_A - Y_s \\ Z_A - Z_s \end{bmatrix} \tag{3-3}$$

where, λ is the scale factor, (υ, ν, ω) are the coordinates of image point in the virtual photo auxiliar coordinate system $S\text{-}XYZ$. For a point in local plane, $z = -f$, and the coordinates (υ, ν, ω) can be expressed as (Luhmann *et al.* 2014, Wolf *et al.* 2014):

$$\begin{bmatrix} \upsilon \\ \nu \\ \omega \end{bmatrix} = \boldsymbol{R} \begin{bmatrix} x \\ y \\ -f \end{bmatrix} = \begin{bmatrix} a_1 & a_2 & a_3 \\ b_1 & b_2 & b_3 \\ c_1 & c_2 & c_3 \end{bmatrix} \begin{bmatrix} x \\ y \\ -f \end{bmatrix} \tag{3-4}$$

Substituting Equation (3-3) into (3-4), we obtain the collinearity equations as (Luhmann *et al.* 2014, Wolf *et al.* 2014):

$$\begin{aligned} x_f - x_0 &= -f\,\frac{a_1(X - X_s) + b_1(Y - Y_s) + c_1(Z - Z_s)}{a_3(X - X_s) + b_3(Y - Y_s) + c_3(Z - Z_s)} \\ y_f - y_0 &= -f\,\frac{a_2(X - X_s) + b_2(Y - Y_s) + c_2(Z - Z_s)}{a_3(X - X_s) + b_3(Y - Y_s) + c_3(Z - Z_s)} \end{aligned} \tag{3-5}$$

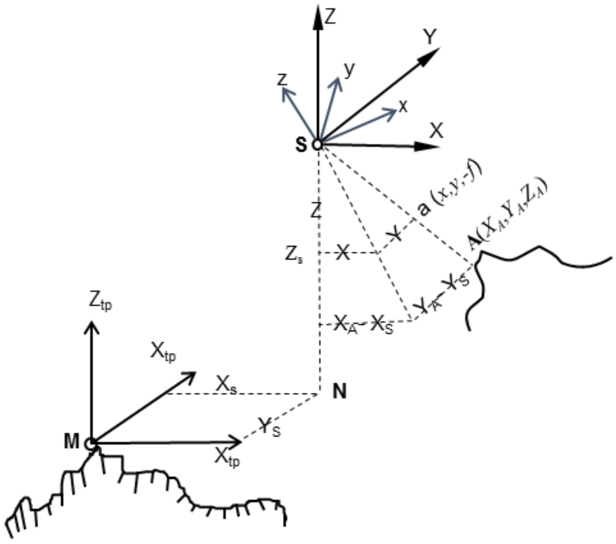

Fig. 3-6 Collinearity condition.

The orientation angles of the camera may have three different rotation orders, and consequently ***R*** has three different expressions.

1) the *φ-ω-κ* system takes Y-axis as the principle axis: first rotate *φ* with respect to Y-axis, then rotate *ω* with respect to X-axis, finally rotate *κ* with respect to Z-axis. Then ***R*** is expressed as (Wang and Xu 2010, Luhmann et al. 2014, Wolf et al. 2014):

$$\begin{aligned} a_1 &= \cos\varphi\cos\kappa - \sin\varphi\sin\omega\sin\kappa \\ a_2 &= -\cos\varphi\sin\kappa - \sin\varphi\sin\omega\cos\kappa \\ a_3 &= -\sin\varphi\cos\omega \\ b_1 &= \cos\omega\sin\kappa \\ b_2 &= \cos\omega\cos\kappa \\ b_3 &= -\sin\omega \\ c_1 &= \sin\varphi\cos\kappa + \cos\varphi\sin\omega\sin\kappa \\ c_2 &= -\sin\varphi\sin\kappa + \cos\varphi\sin\omega\cos\kappa \\ c_3 &= \cos\varphi\cos\omega \end{aligned} \tag{3-6}$$

2) the *ω-φ-κ* system takes X axis as the principle axis: first rotate *ω* with respect to X-axis, then rotate *φ* with respect to Y-axis, finally rotate *κ* with respect to Z-axis. Then ***R*** is expressed as (Wang and Xu 2010, Luhmann *et al.* 2014, Wolf *et al.* 2014):

$$
\begin{aligned}
a_1 &= \cos\varphi\cos\kappa \\
a_2 &= -\cos\varphi\sin\kappa \\
a_3 &= -\sin\varphi \\
b_1 &= \cos\omega\sin\kappa - \sin\omega\sin\varphi\cos\kappa \\
b_2 &= \cos\omega\cos\kappa + \sin\omega\sin\varphi\sin\kappa \\
b_3 &= -\sin\omega\cos\varphi \\
c_1 &= \sin\omega\sin\kappa + \cos\omega\sin\varphi\cos\kappa \\
c_2 &= \sin\omega\cos\kappa - \cos\omega\sin\varphi\sin\kappa \\
c_3 &= \cos\varphi\cos\omega
\end{aligned}
\tag{3-7}
$$

3) the A-α-κ system takes Z-axis as the principle axis: first rotate A with respect to Z-axis, then rotate α with respect to Y-axis, finally rotate κ with respect to X-axis. Then $\boldsymbol{R}$ is expressed as (Wang and Xu 2010, Luhmann *et al.* 2014, Wolf *et al.* 2014):

$$
\begin{aligned}
a_1 &= cosAcos\kappa + sinAcos\alpha sin\kappa \\
a_2 &= -cosAsin\kappa + sinAcos\alpha cos\kappa \\
a_3 &= -sinAsin\alpha \\
b_1 &= -sinAcos\kappa + cosAcos\alpha sin\kappa \\
b_2 &= sinAsin\kappa + cosAcos\alpha cos\kappa \\
b_3 &= -cosAsin\alpha \\
c_1 &= sin\alpha sin\kappa \\
c_2 &= sin\alpha cos\kappa \\
c_3 &= cos\alpha
\end{aligned}
\tag{3-8}
$$

The observations and unknown parameters of the collinearity equation (3-5) have a none-linear function relationship. In order to solve them they have to be linearized with Taylor expansion series as (Wang and Xu 2010, Luhmann *et al.* 2014, Wolf *et al.* 2014):

$$
\begin{aligned}
v_x &= \frac{\partial x}{\partial \phi}\Delta\varphi + \frac{\partial x}{\partial \omega}\Delta\omega + \frac{\partial x}{\partial \kappa}\Delta\kappa + \frac{\partial x}{\partial X_s}\Delta X_s + \frac{\partial x}{\partial Y_s}\Delta Y_s + \frac{\partial x}{\partial Z_s}\Delta Z_s \\
&\quad + \frac{\partial x}{\partial X}\Delta X + \frac{\partial x}{\partial Y}\Delta Y + \frac{\partial x}{\partial Z}\Delta Z + \frac{\partial x}{\partial x_0}\Delta x_0 + \frac{\partial x}{\partial y_0}\Delta y_0 + \frac{\partial x}{\partial f}\Delta f + x^0 - \left(x - x_0\right) \\
v_y &= \frac{\partial y}{\partial \phi}\Delta\varphi + \frac{\partial y}{\partial \omega}\Delta\omega + \frac{\partial y}{\partial \kappa}\Delta\kappa + \frac{\partial y}{\partial X_s}\Delta X_s + \frac{\partial y}{\partial Y_s}\Delta Y_s + \frac{\partial y}{\partial Z_s}\Delta Z_s \\
&\quad + \frac{\partial y}{\partial X}\Delta X + \frac{\partial y}{\partial Y}\Delta Y + \frac{\partial y}{\partial Z}\Delta Z + \frac{\partial y}{\partial x_0}\Delta x_0 + \frac{\partial y}{\partial y_0}\Delta y_0 + \frac{\partial y}{\partial f}\Delta f + y^0 - \left(y - y_0\right)
\end{aligned}
\tag{3-9}
$$

where, (x, y) are the observations and (x^0, y^0) are the approximate values, (v_x, v_y) are the corresponding corrections, $(\Delta X, \Delta Y, \Delta Z)$ are the coordinate corrections of the ground point, ΔX_s, ΔY_s, ΔZ_s, $\Delta\varphi$, $\Delta\omega$, $\Delta\kappa$ are the corrections of the interior parameters, and Δf is the correction of the focal length.

In this way the linearized equations are obtained, which are the core of the photogrammetric work, and almost all calculations are started with this equation. In the following sections, the process of backward intersection, forward intersection, and bundle adjustment will be discussed in detail.

3.2.1 Backward intersection based on Ground Control Points

The backward intersection method, the process with only one photo is called "space resection", and with blocks of photos is named as "Aerial Triangulation by Bundle Adjustment", is to determine the exterior orientation parameters, (X_s, Y_s, Z_s, φ, ω, κ), with the knowing of interior parameters (x_0, y_0, f), and the ground points coordinates (X, Y, Z). The process is shown as Fig. 3-7.

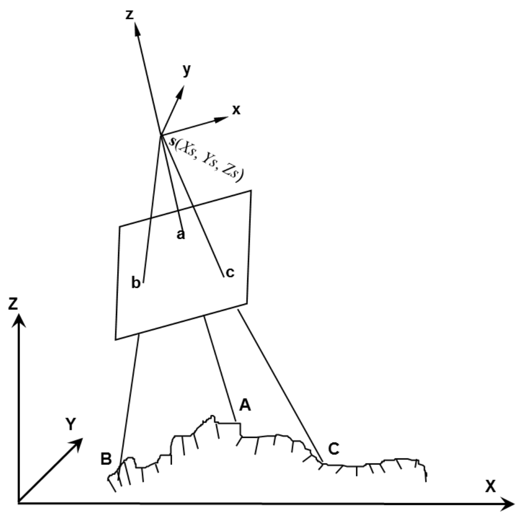

Fig. 3-7 The backward intersection method.

and, the equation (3-9) can be rewritten as (Wang and Xu 2010, Wolf *et al.* 2014):

$$
\begin{aligned}
v_x &= \frac{\partial x}{\partial \phi}\Delta\varphi + \frac{\partial x}{\partial \omega}\Delta\omega + \frac{\partial x}{\partial \kappa}\Delta\kappa + \frac{\partial x}{\partial X_s}\Delta X_s + \frac{\partial x}{\partial Y_s}\Delta Y_s + \frac{\partial x}{\partial Z_s}\Delta Z_s + x^0 - x \\
v_y &= \frac{\partial y}{\partial \phi}\Delta\varphi + \frac{\partial y}{\partial \omega}\Delta\omega + \frac{\partial y}{\partial \kappa}\Delta\kappa + \frac{\partial y}{\partial X_s}\Delta X_s + \frac{\partial y}{\partial Y_s}\Delta Y_s + \frac{\partial y}{\partial Z_s}\Delta Z_s + y^0 - y
\end{aligned}
\qquad (3\text{-}10)
$$

In order to calculate the partial derivatives, notation ($\overline{X}$, $\overline{Y}$, $\overline{Z}$) are introduced by following rules (Wang and Xu 2010, Wolf *et al.* 2014):

$$
\begin{aligned}
x - x_0 &= -f\,\frac{a_1(X - X_s) + b_1(Y - Y_s) + c_1(Z - Z_s)}{a_3(X - X_s) + b_3(Y - Y_s) + c_3(Z - Z_s)} = -f\,\frac{\overline{X}}{\overline{Z}} \\
y - y_0 &= -f\,\frac{a_2(X - X_s) + b_2(Y - Y_s) + c_2(Z - Z_s)}{a_3(X - X_s) + b_3(Y - Y_s) + c_3(Z - Z_s)} = -f\,\frac{\overline{Y}}{\overline{Z}}
\end{aligned}
\qquad (3\text{-}11)
$$

$$\begin{bmatrix} \overline{X} \\ \overline{Y} \\ \overline{Z} \end{bmatrix} = \begin{bmatrix} a_1 & b_1 & c_1 \\ a_2 & b_2 & c_2 \\ a_3 & b_3 & c_3 \end{bmatrix} \begin{bmatrix} X - X_s \\ Y - Y_s \\ Z - Z_s \end{bmatrix} = \boldsymbol{R}^{-1} \begin{bmatrix} X - X_s \\ Y - Y_s \\ Z - Z_s \end{bmatrix} \tag{3-12}$$

Then the partial derivatives in Equation (3-10) can be expressed as (Wang and Xu 2010, Wolf *et al.* 2014):

$$\begin{aligned}
a_{11} &= \frac{\partial x}{\partial X_s} = \frac{1}{\overline{Z}}\left(a_1 f + a_3 x\right) \\
a_{12} &= \frac{\partial x}{\partial Y_s} = \frac{1}{\overline{Z}}\left(b_1 f + b_3 x\right) \\
a_{13} &= \frac{\partial x}{\partial Z_s} = \frac{1}{\overline{Z}}\left(c_1 f + c_3 x\right) \\
a_{21} &= \frac{\partial y}{\partial X_s} = \frac{1}{\overline{Z}}\left(a_2 f + a_3 y\right) \\
a_{22} &= \frac{\partial y}{\partial Y_s} = \frac{1}{\overline{Z}}\left(b_2 f + b_3 y\right) \\
a_{23} &= \frac{\partial y}{\partial Z_s} = \frac{1}{\overline{Z}}\left(c_2 f + c_3 y\right)
\end{aligned} \tag{3-13}$$

because:

$$\begin{aligned}
\frac{\partial}{\partial \varphi}\begin{bmatrix} \overline{X} \\ \overline{Y} \\ \overline{Z} \end{bmatrix} &= \begin{bmatrix} 0 & -b3 & b2 \\ b3 & 0 & -b1 \\ -b2 & b1 & 0 \end{bmatrix} \begin{bmatrix} \overline{X} \\ \overline{Y} \\ \overline{Z} \end{bmatrix} \\
\frac{\partial}{\partial \omega}\begin{bmatrix} \overline{X} \\ \overline{Y} \\ \overline{Z} \end{bmatrix} &= \begin{bmatrix} \overline{Z} \sin\kappa \\ \overline{Y} \cos\kappa \\ -\overline{X} \sin\kappa - \overline{Y} \cos\kappa \end{bmatrix} \\
\frac{\partial}{\partial \kappa}\begin{bmatrix} \overline{X} \\ \overline{Y} \\ \overline{Z} \end{bmatrix} &= \begin{bmatrix} \overline{Y} \\ -\overline{X} \\ 0 \end{bmatrix}
\end{aligned} \tag{3-14}$$

then:

$$\begin{aligned}
a_{14} &= \frac{\partial x}{\partial \phi} = -\frac{f}{\left(\overline{Z}\right)^2}\left(\frac{\partial \overline{X}}{\partial \phi}\overline{Z} - \frac{\partial \overline{Z}}{\partial \phi}\overline{X}\right) = y \sin\omega \\
&\quad - \left[\frac{x}{f}\left(x \cos\kappa - y \sin\kappa\right) + f \cos\kappa\right] \cos\omega \\
a_{15} &= \frac{\partial x}{\partial \omega} = -\frac{f}{\left(\overline{Z}\right)^2}\left(\frac{\partial \overline{X}}{\partial \omega}\overline{Z} - \frac{\partial \overline{Z}}{\partial \omega}\overline{X}\right) = -f \sin\kappa - \frac{x}{f}\left(x \sin\kappa + y \cos\kappa\right)
\end{aligned}$$

$$a_{16} = \frac{\partial x}{\partial \kappa} = -\frac{f}{\left(\overline{Z}\right)^2}\left(\frac{\partial \overline{X}}{\partial \kappa}\overline{Z} - \frac{\partial \overline{Z}}{\partial \kappa}\overline{X}\right) = y$$

$$\begin{aligned}
a_{24} &= \frac{\partial y}{\partial \phi} = -\frac{f}{\left(\overline{Z}\right)^2}\left(\frac{\partial \overline{X}}{\partial \phi}\overline{Z} - \frac{\partial \overline{Z}}{\partial \phi}\overline{Y}\right) = -x\sin\omega \\
&\quad -\left[\frac{y}{f}\left(x\cos\kappa - y\sin\kappa\right) - f\sin\kappa\right]\cos\omega \\
a_{25} &= \frac{\partial y}{\partial \omega} = -\frac{f}{\left(\overline{Z}\right)^2}\left(\frac{\partial \overline{X}}{\partial \omega}\overline{Z} - \frac{\partial \overline{Z}}{\partial \omega}\overline{Y}\right) = -f\cos\kappa - \frac{y}{f}\left(x\sin\kappa + y\cos\kappa\right) \\
a_{26} &= \frac{\partial y}{\partial \kappa} = -\frac{f}{\left(\overline{Z}\right)^2}\left(\frac{\partial \overline{X}}{\partial \kappa}\overline{Z} - \frac{\partial \overline{Z}}{\partial \kappa}\overline{Y}\right) = -x
\end{aligned} \tag{3-15}$$

In general, the process of backward intersection discussed in this section is mainly for one single photos. In practical applications, there are at least two photos (a stereo pair), combing the GCPs and tie points, the process backward becomes the Aerial Triangulation by Bundle Adjustment.

3.2.2 Forward intersection based on stereo images

The forward intersection method is used to determine the ground points coordinates (X, Y, Z), with the knowledge of interior parameters (x_0, y_0, f) and exterior orientation parameters (X_s, Y_s, Z_s, φ, ω, κ). The process is shown as Fig. 3-8.

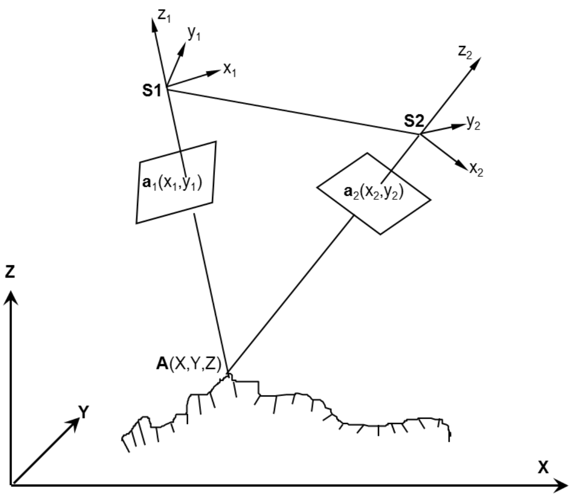

Fig. 3-8 The forward intersection method.

If the interior elements and exterior orientation elements of the camera are known, the collinearity equation can be illustrated as (Wang and Xu 2010):

$$\begin{aligned} l_1 X + l_2 Y + l_3 Z - l_x = 0 \\ l_4 X + l_5 Y + l_6 Z - l_y = 0 \end{aligned} \tag{3-16}$$

where,

$$\begin{aligned} &l_1 = fa_1 + (x - x_0)a_3, \quad l_2 = fb_1 + (x - x_0)b_3, \quad l_3 = fc_1 + (x - x_0)c_3 \\ &l_x = fa_1 X_s + fb_1 Y_s + fc_1 Y_s + (x - x_0)a_3 X_s + (x - x_0)b_3 Y_s + (x - x_0)c_3 Z_s \\ &l_4 = fa_2 + (\mathrm{y} - \mathrm{y}_0)a_3, \quad l_5 = fb_2 + (\mathrm{y} - \mathrm{y}_0)b_3, \quad l_6 = fc_2 + (\mathrm{y} - \mathrm{y}_0)c_3 \\ &l_y = fa_2 X_s + fb_2 Y_s + fc_2 Y_s + (\mathrm{y} - \mathrm{y}_0)a_3 X_s + (\mathrm{y} - \mathrm{y}_0)b_3 Y_s + (\mathrm{y} - \mathrm{y}_0)c_3 Z_s \end{aligned} \tag{3-17}$$

where,

$$\begin{aligned} a_1 &= \cos\varphi\cos\kappa - \sin\varphi\sin\omega\sin\kappa \\ a_2 &= -\cos\varphi\sin\kappa - \sin\varphi\sin\omega\cos\kappa \\ a_3 &= -\sin\varphi\cos\omega \\ b_1 &= \cos\omega\sin\kappa \\ b_2 &= \cos\omega\cos\kappa \\ b_3 &= -\sin\omega \\ c_1 &= \sin\varphi\cos\kappa + \cos\varphi\sin\omega\sin\kappa \\ c_2 &= -\sin\varphi\sin\kappa + \cos\varphi\sin\omega\cos\kappa \\ c_3 &= \cos\varphi\cos\omega \end{aligned} \tag{3-18}$$

With a conjugate point in a stereo pair, according to the equation (3-16), four collinearity equations can be obtained. And with n images, the equation (3-16) can be written as:

$$\begin{bmatrix} l_1^1 & l_2^1 & l_3^1 \\ l_4^1 & l_5^1 & l_6^1 \\ l_1^2 & l_2^2 & l_3^2 \\ l_4^2 & l_5^2 & l_6^2 \\ \vdots & \vdots & \vdots \\ l_1^n & l_2^n & l_3^n \\ l_4^n & l_5^n & l_6^n \end{bmatrix} \begin{bmatrix} X \\ Y \\ Z \end{bmatrix} = \begin{bmatrix} l_x^1 \\ l_y^1 \\ l_x^2 \\ l_y^2 \\ \vdots \\ l_x^n \\ l_y^n \end{bmatrix} \tag{3-19}$$

or in an abbreviate form as:

$$\boldsymbol{AX} = \boldsymbol{L} \tag{3-20}$$

The geo-reference coordinates of the corresponding terrain point (X, Y, Z) are the unknown parameters. This equation can resolved by the method of least square as:

$$\boldsymbol{X} = \left(\boldsymbol{A}^T \boldsymbol{P}_{ll} \boldsymbol{A}\right)^{-1} \boldsymbol{A}^T \boldsymbol{P}_{ll} \boldsymbol{L} \tag{3-21}$$

$$\boldsymbol{Q}_{XX} = \left(\boldsymbol{A}^T \boldsymbol{P}_{ll} \boldsymbol{A}\right)^{-1} \tag{3-22}$$

If the interior elements (x_0, y_0, f) are already known, the most important work becomes how to get precise exterior orientation parameters without GCPs.

3.2.3 Bundle adjustment

Bundle adjustment integrates the backward intersection and forward intersection into one step, which means that all the interior parameters, exterior orientation parameters, and the coordinates of the known/unknown ground points, are estimated together. The theoretical model of this method is more rigorous, and the accuracy is better than one separated backward intersection and forward intersection. The corresponding error equations for an image pair are taken as (Wang and Xu 2010, Wolf *et al.* 2014):

$$\begin{aligned} v_x &= \frac{\partial x}{\partial \varphi}\Delta\varphi + \frac{\partial x}{\partial \omega}\Delta\omega + \frac{\partial x}{\partial \kappa}\Delta\kappa + \frac{\partial x}{\partial X_s}\Delta X_s + \frac{\partial x}{\partial Y_s}\Delta Y_s + \frac{\partial x}{\partial Z_s}\Delta Z_s \\ &\quad + \frac{\partial x}{\partial X}\Delta X + \frac{\partial x}{\partial Y}\Delta Y + \frac{\partial x}{\partial Z}\Delta Z + x^0 - x \\ v_y &= \frac{\partial y}{\partial \varphi}\Delta\varphi + \frac{\partial y}{\partial \omega}\Delta\omega + \frac{\partial y}{\partial \kappa}\Delta\kappa + \frac{\partial y}{\partial X_s}\Delta X_s + \frac{\partial y}{\partial Y_s}\Delta Y_s + \frac{\partial y}{\partial Z_s}\Delta Z_s \\ &\quad + \frac{\partial y}{\partial X}\Delta X + \frac{\partial y}{\partial Y}\Delta Y + \frac{\partial y}{\partial Z}\Delta Z + y^0 - y \end{aligned} \tag{3-23}$$

The matrix form can be expressed as (Wang and Xu 2010, Wolf *et al.* 2014):

$$\begin{bmatrix} \boldsymbol{V}_1 \\ \boldsymbol{V}_2 \end{bmatrix} = \begin{bmatrix} \boldsymbol{A}_1 & \boldsymbol{0} & \vdots & \boldsymbol{B}_1 \\ \boldsymbol{0} & \boldsymbol{A}_2 & \vdots & \boldsymbol{B}_2 \end{bmatrix} \begin{bmatrix} \boldsymbol{t}_1 \\ \boldsymbol{t}_2 \\ \vdots \\ \boldsymbol{X} \end{bmatrix} - \begin{bmatrix} \boldsymbol{l}_1 \\ \boldsymbol{l}_2 \end{bmatrix} \tag{3-24}$$

or:

$$\boldsymbol{V} = \begin{bmatrix} \boldsymbol{A} & \vdots & \boldsymbol{B} \end{bmatrix} \begin{bmatrix} \boldsymbol{t} \\ \boldsymbol{X} \end{bmatrix} - \boldsymbol{L} \tag{3-25}$$

where,

$\boldsymbol{V}_1 = \begin{bmatrix} v_{x_1} & v_{y_1} \end{bmatrix}^{\mathrm{T}}$, $\boldsymbol{V}_2 = \begin{bmatrix} v_{x_2} & v_{y_2} \end{bmatrix}^{\mathrm{T}}$,

$\boldsymbol{A}_1 = \begin{bmatrix} a_{11} & a_{12} & a_{13} & a_{14} & a_{15} & a_{16} \\ a_{21} & a_{22} & a_{23} & a_{24} & a_{25} & a_{26} \end{bmatrix}_{left\ image}$, $\boldsymbol{A}_2 = \begin{bmatrix} a_{11} & a_{12} & a_{13} & a_{14} & a_{15} & a_{16} \\ a_{21} & a_{22} & a_{23} & a_{24} & a_{25} & a_{26} \end{bmatrix}_{right\ image}$,

$\boldsymbol{B}_1 = \begin{bmatrix} -a_{11} & -a_{12} & -a_{13} \\ -a_{21} & -a_{22} & -a_{23} \end{bmatrix}_{left\ image}$, $\boldsymbol{B}_2 = \begin{bmatrix} -a_{11} & -a_{12} & -a_{13} \\ -a_{21} & -a_{22} & -a_{23} \end{bmatrix}_{right\ image}$,

$$\boldsymbol{t}_1 = \begin{bmatrix} \Delta X_{s_1} & \Delta Y_{s_1} & \Delta Z_{s_1} & \Delta\varphi_1 & \Delta\omega_1 & \Delta\kappa_1 \end{bmatrix}^{\mathrm{T}}, \boldsymbol{t}_2 = \begin{bmatrix} \Delta X_{s_2} & \Delta Y_{s_2} & \Delta Z_{s_2} & \Delta\varphi_2 & \Delta\omega_2 & \Delta\kappa_2 \end{bmatrix}^{\mathrm{T}},$$

$$\boldsymbol{X} = \begin{bmatrix} \Delta X & \Delta Y & \Delta Z \end{bmatrix}^{\mathrm{T}}, \boldsymbol{l}_1 = \begin{bmatrix} l_{x_1} & l_{y_1} \end{bmatrix}^{\mathrm{T}}, \boldsymbol{l}_2 = \begin{bmatrix} l_{x_2} & l_{y_2} \end{bmatrix}^{\mathrm{T}}$$

The normal equation is (Wang and Xu 2010, Wolf *et al.* 2014):

$$\begin{bmatrix} \boldsymbol{A}^{\mathrm{T}}\boldsymbol{PA} & \boldsymbol{A}^{\mathrm{T}}\boldsymbol{PB} \\ \boldsymbol{B}^{\mathrm{T}}\boldsymbol{PA} & \boldsymbol{B}^{\mathrm{T}}\boldsymbol{PB} \end{bmatrix} \begin{bmatrix} \boldsymbol{t} \\ \boldsymbol{x} \end{bmatrix} = \begin{bmatrix} \boldsymbol{A}^{\mathrm{T}}\boldsymbol{PL} \\ \boldsymbol{B}^{\mathrm{T}}\boldsymbol{PL} \end{bmatrix} \tag{3-26}$$

or:

$$\begin{bmatrix} \boldsymbol{N}_{11} & \boldsymbol{N}_{12} \\ \boldsymbol{N}_{12}^{\mathrm{T}} & \boldsymbol{N}_{22} \end{bmatrix} \begin{bmatrix} \boldsymbol{t} \\ \boldsymbol{X} \end{bmatrix} = \begin{bmatrix} \boldsymbol{u}_1 \\ \boldsymbol{u}_2 \end{bmatrix} \tag{3-27}$$

where, $\boldsymbol{N}_{11} = \boldsymbol{A}^{\mathrm{T}}\boldsymbol{A}$, $\boldsymbol{N}_{12} = \boldsymbol{A}^{\mathrm{T}}\boldsymbol{B}$, and $\boldsymbol{N}_{22} = \boldsymbol{B}^{\mathrm{T}}\boldsymbol{B}$.

Then we get the two separated normal equations as (Wang and Xu 2010, Wolf *et al.* 2014):

$$\begin{aligned} \left(\boldsymbol{N}_{11} - \boldsymbol{N}_{12}\boldsymbol{N}_{22}^{-1}\boldsymbol{N}_{12}^{\mathrm{T}}\right)\boldsymbol{t} &= \left(\boldsymbol{u}_1 - \boldsymbol{N}_{12}\boldsymbol{N}_{22}^{-1}\boldsymbol{u}_2\right) \\ \left(\boldsymbol{N}_{22} - \boldsymbol{N}_{12}^{\mathrm{T}}\boldsymbol{N}_{11}^{-1}\boldsymbol{N}_{12}\right)\boldsymbol{X} &= \left(\boldsymbol{u}_2 - \boldsymbol{N}_{12}^{\mathrm{T}}\boldsymbol{N}_{11}^{-1}\boldsymbol{u}_1\right) \end{aligned} \tag{3-28}$$

The equations above are for an image pair, if taking into account more images, for instance, there are 4 images, 8 known GCPs and 2 unknown points, the equation (3-24) can be expanded as:

$$\underset{2mn\times 1}{\begin{bmatrix} \boldsymbol{V}_1^1 \\ \boldsymbol{V}_2^1 \\ \boldsymbol{V}_3^1 \\ \boldsymbol{V}_4^1 \\ \boldsymbol{V}_5^1 \\ \boldsymbol{V}_6^1 \\ \boldsymbol{V}_7^1 \\ \boldsymbol{V}_8^1 \\ \vdots \\ \boldsymbol{V}_1^n \\ \boldsymbol{V}_2^n \\ \boldsymbol{V}_3^n \\ \boldsymbol{V}_4^n \\ \boldsymbol{V}_5^n \\ \boldsymbol{V}_6^n \\ \boldsymbol{V}_7^n \\ \boldsymbol{V}_8^n \end{bmatrix}} = \begin{bmatrix} \boldsymbol{A}_1^1 & \cdots & \boldsymbol{0} & \boldsymbol{0} & \boldsymbol{0} \\ \boldsymbol{A}_2^1 & \cdots & \boldsymbol{0} & \boldsymbol{0} & \boldsymbol{0} \\ \boldsymbol{A}_3^1 & \cdots & \boldsymbol{0} & \boldsymbol{0} & \boldsymbol{0} \\ \boldsymbol{A}_4^1 & \cdots & \boldsymbol{0} & \boldsymbol{0} & \boldsymbol{0} \\ \boldsymbol{A}_5^1 & \cdots & \boldsymbol{0} & \boldsymbol{0} & \boldsymbol{0} \\ \boldsymbol{A}_6^1 & \cdots & \boldsymbol{0} & \boldsymbol{0} & \boldsymbol{0} \\ \boldsymbol{A}_7^1 & \cdots & \boldsymbol{0} & \boldsymbol{B}_7^1 & \boldsymbol{0} \\ \boldsymbol{A}_8^1 & \cdots & \boldsymbol{0} & \boldsymbol{0} & \boldsymbol{B}_8^1 \\ \vdots & \ddots & \vdots & \vdots & \vdots \\ \boldsymbol{0} & \cdots & \boldsymbol{A}_1^n & \boldsymbol{0} & \boldsymbol{0} \\ \boldsymbol{0} & \cdots & \boldsymbol{A}_2^n & \boldsymbol{0} & \boldsymbol{0} \\ \boldsymbol{0} & \cdots & \boldsymbol{A}_3^n & \boldsymbol{0} & \boldsymbol{0} \\ \boldsymbol{0} & \cdots & \boldsymbol{A}_4^n & \boldsymbol{0} & \boldsymbol{0} \\ \boldsymbol{0} & \cdots & \boldsymbol{A}_5^n & \boldsymbol{0} & \boldsymbol{0} \\ \boldsymbol{0} & \cdots & \boldsymbol{A}_6^n & \boldsymbol{0} & \boldsymbol{0} \\ \boldsymbol{0} & \cdots & \boldsymbol{A}_7^n & \boldsymbol{B}_7^n & \boldsymbol{0} \\ \boldsymbol{0} & \cdots & \boldsymbol{A}_8^n & \boldsymbol{0} & \boldsymbol{B}_8^n \end{bmatrix}_{2mn\times 6n \quad 2mn\times 3k} \underset{(6n+3k)\times 1}{\begin{bmatrix} \boldsymbol{t}_1 \\ \boldsymbol{t}_2 \\ \boldsymbol{t}_3 \\ \boldsymbol{t}_4 \\ \boldsymbol{X}_7 \\ \boldsymbol{X}_8 \end{bmatrix}} - \underset{2mn\times 1}{\begin{bmatrix} \boldsymbol{l}_1^1 \\ \boldsymbol{l}_2^1 \\ \boldsymbol{l}_3^1 \\ \boldsymbol{l}_4^1 \\ \boldsymbol{l}_5^1 \\ \boldsymbol{l}_6^1 \\ \boldsymbol{l}_7^1 \\ \boldsymbol{l}_8^1 \\ \vdots \\ \boldsymbol{l}_1^n \\ \boldsymbol{l}_2^n \\ \boldsymbol{l}_3^n \\ \boldsymbol{l}_4^n \\ \boldsymbol{l}_5^n \\ \boldsymbol{l}_6^n \\ \boldsymbol{l}_7^n \\ \boldsymbol{l}_8^n \end{bmatrix}} \tag{3-29}$$

where, $m = 8$, $n = 4$, $k = 2$.

From equations (3-24) and (3-29), we can see that all the parameters are estimated in a least squares process, which is the reason that the bundle adjustment method is more rigorous, and the accuracy of the final solution will better.

3.3 The process of GNSS/IMU aided photogrammetry

Normally the interior parameters are calculated by camera calibration, and the exterior orientation parameters are obtained from the Aerial Triangulation, which means a small calibration field is still needed to determinate the attitude differences between the camera and the IMUs, Fig. 3-9 is the overview of the photogrammetric project with a small calibration field. A "pure" POS without GCPs has the disadvantages of missing redundancy, because the wrong GNSS reference coordinates and the bad solution of the GNSS rover will directly affect the final results (Kremer and Kruck 2003).

The GNSS/IMU position $(X_{IMU}, Y_{IMU}, Z_{IMU})$ and orientation angles (ϕ, θ, ψ) derived are referred to the IMU center. Note that the notation φ used in photogrammetric frame means the pitch of the photogrammetric frame, and ϕ in the navigation frame means the roll. There are position offsets and orientation bore-sight between the camera and IMU as shown in Fig. 3-10.

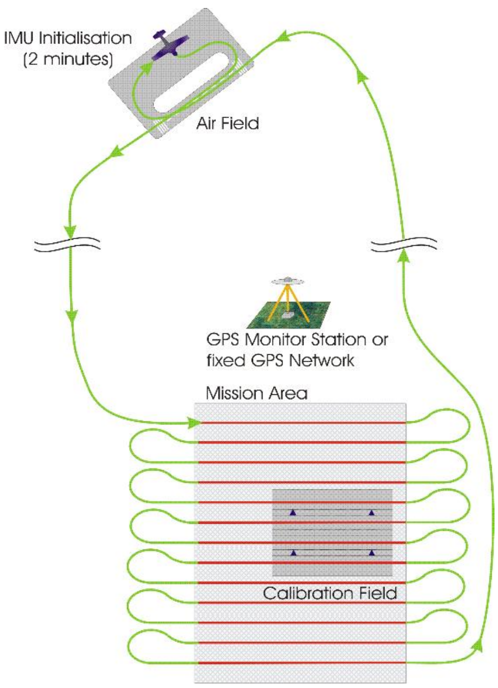

Fig. 3-9 Photogrammetric project with a small calibration field (IGI mbH Company. 2007).

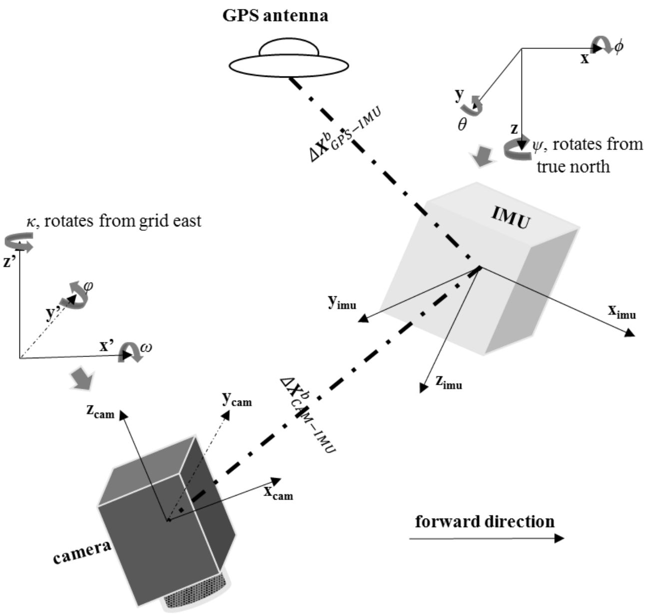

Fig. 3-10 Position offsets and orientation bore-sight between the camera and IMU.

The coordinates of the center of the camera in the navigation frame can be calculated as:

$$\boldsymbol{X}^n_{CAM} = \boldsymbol{X}^n_{IMU} + \boldsymbol{C}^n_b \Delta \boldsymbol{X}^b_{CAM-IMU} = \boldsymbol{X}^n_{GPS} - \boldsymbol{C}^n_b \Delta \boldsymbol{X}^b_{GPS-IMU} + \boldsymbol{C}^n_b \Delta \boldsymbol{X}^b_{CAM-IMU} \tag{3-30}$$

where, the item $\Delta \boldsymbol{X}^b_{GPS-IMU}$ represents the distance between the center of IMU and GPS, and $\Delta \boldsymbol{X}^b_{CAM-IMU}$ means the distance between IMU and camera. The two delta items are offset values measured directly and the term $\boldsymbol{C}^n_b$ is the Direction Cosine Matrix from IMU body frame b to navigation frame n, which is calculated using the orientation information (ϕ, θ, ψ). From Fig. 3-10 we can also see that the definitions of the orientation angles in the photogrammetry and navigation frames are different. First of all, in the navigation frame the directions of the $[X\ Y\ Z]_{IMU}$ axes are normally taken as front-right-down, while in photogrammetry the directions of $[X\ Y\ Z]_{CAM}$ are front-left-up, with both coordinate systems being right handed. Secondly, in the navigation frame ψ means the rotation angle about z-axis from true north direction, ϕ and θ mean, respectively, the rotation angle of the x- and y- axis; in the photogrammetric frame κ means the rotation angle about z'- axis from grid east direction, ω and φ are the rotation angles of x'- and y'- axis, respectively, and the transformation matrix from the navigation frame to the camera frame, $\boldsymbol{T}^s_n$, has the rotation order of ω-φ-κ or φ-ω-κ. In order to build the relationship between the IMU frame b and the camera frame s, at the IMU center we define a new body frame b_s, at which the axes directions are front-left-up like in the camera frame s, as shown in Fig. 3-11.

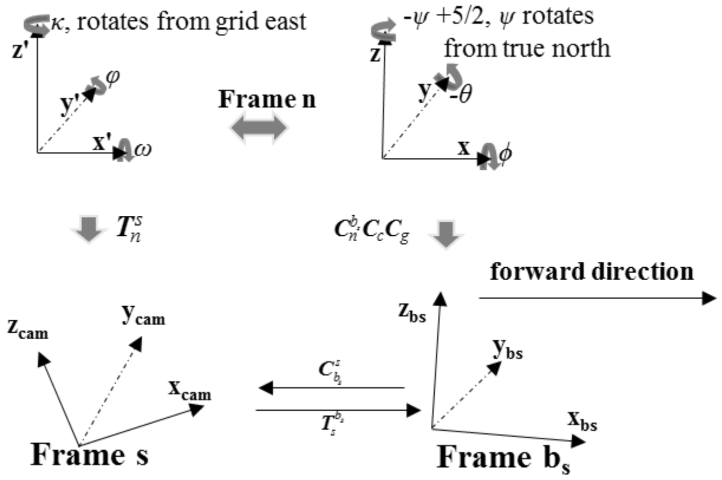

Fig. 3-11 The relationship between the camera frame s and the new body frame b_s.

From Fig. 3-11 we can see that $C_n^{b_s}$ and T_n^s can be connected by the following equation:

$$T_n^s = C_{b_s}^s C_n^{b_s} C_c C_g \tag{3-31}$$

or,

$$C_n^{b_s} = T_s^{b_s} T_n^s \left(C_c C_g\right)^{-1} \tag{3-32}$$

with

$$C_c = \begin{bmatrix} 0 & -1 & 0 \\ 1 & 0 & 0 \\ 0 & 0 & 1 \end{bmatrix}, \quad C_g = \begin{bmatrix} \cos\alpha & -\sin\alpha & 0 \\ \sin\alpha & \cos\alpha & 0 \\ 0 & 0 & 1 \end{bmatrix}$$

$$\begin{aligned} C_n^{b_s} &= \begin{bmatrix} 1 & 0 & 0 \\ 0 & \cos\phi & \sin\phi \\ 0 & -\sin\phi & \cos\phi \end{bmatrix} \begin{bmatrix} \cos\theta & 0 & \sin\theta \\ 0 & 1 & 0 \\ -\sin\theta & 0 & \cos\theta \end{bmatrix} \begin{bmatrix} \cos\psi & -\sin\psi & 0 \\ \sin\psi & \cos\psi & 0 \\ 0 & 0 & 1 \end{bmatrix} \\ &= \begin{bmatrix} \cos\theta\cos\psi & -\cos\theta\sin\psi & \sin\theta \\ -\sin\phi\sin\theta\cos\psi + \cos\phi\sin\psi & \sin\phi\sin\theta\sin\psi + \cos\phi\cos\psi & \sin\phi\cos\theta \\ -\cos\phi\sin\theta\cos\psi - \sin\phi\sin\psi & \cos\phi\sin\theta\sin\psi - \sin\phi\cos\psi & \cos\phi\cos\theta \end{bmatrix} \end{aligned}$$

here, α is the convergence angle between grid north and true north, $C_{b_s}^s$ and $T_s^{b_s}$ are the angle bore-sight transformation matrices between the b_s frame and the camera frame s in different directions, as Fig. 3-11 shows, which can be estimated through aerial triangulation. In the ideal status that the b_s frame is parallel to the s frame, then both $C_{b_s}^s$ and $T_s^{b_s}$ become the unit matrix $\boldsymbol{I}$.

In different rotation orders, T_n^s has different expressions. In the ω-φ-κ order, we have (Luhmann *et al.* 2014, Wolf *et al.* 2014):

$$
\begin{aligned}
\boldsymbol{T}_n^s &= \begin{bmatrix} \cos\kappa & \sin\kappa & 0 \\ -\sin\kappa & \cos\kappa & 0 \\ 0 & 0 & 1 \end{bmatrix} \begin{bmatrix} \cos\varphi & 0 & -\sin\varphi \\ 0 & 1 & 0 \\ \sin\varphi & 0 & \cos\varphi \end{bmatrix} \begin{bmatrix} 1 & 0 & 0 \\ 0 & \cos\omega & \sin\omega \\ 0 & -\sin\omega & \cos\omega \end{bmatrix} \\
&= \begin{bmatrix} \cos\kappa\cos\varphi & \sin\kappa\cos\omega + \cos\kappa\sin\varphi\sin\omega & \sin\kappa\sin\omega - \cos\kappa\sin\varphi\cos\omega \\ -\sin\kappa\cos\varphi & \cos\kappa\cos\omega - \sin\kappa\sin\varphi\sin\omega & \cos\kappa\sin\omega + \sin\kappa\sin\varphi\cos\omega \\ \sin\varphi & -\cos\varphi\sin\omega & \cos\varphi\cos\omega \end{bmatrix}
\end{aligned}
\tag{3-33}
$$

And in the φ-ω-κ order we have (Luhmann *et al.* 2014, Wolf *et al.* 2014):

$$
\begin{aligned}
\boldsymbol{T}_n^s &= \begin{bmatrix} \cos\kappa & \sin\kappa & 0 \\ -\sin\kappa & \cos\kappa & 0 \\ 0 & 0 & 1 \end{bmatrix} \begin{bmatrix} 1 & 0 & 0 \\ 0 & \cos\omega & \sin\omega \\ 0 & -\sin\omega & \cos\omega \end{bmatrix} \begin{bmatrix} \cos\varphi & 0 & -\sin\varphi \\ 0 & 1 & 0 \\ \sin\varphi & 0 & \cos\varphi \end{bmatrix} \\
&= \begin{bmatrix} \cos\kappa\cos\varphi + \sin\kappa\sin\omega\sin\varphi & \sin\kappa\cos\varphi & -\cos\kappa\sin\varphi + \sin\kappa\sin\omega\cos\varphi \\ -\sin\kappa\cos\varphi + \cos\kappa\sin\omega\sin\varphi & \cos\kappa\cos\varphi & \sin\kappa\sin\varphi + \cos\kappa\sin\omega\cos\varphi \\ \cos\omega\sin\varphi & -\sin\omega & \cos\omega\cos\varphi \end{bmatrix}
\end{aligned}
\tag{3-34}
$$

In GNSS/IMU aided aerial photogrammetry, if the navigation orientation angles (ϕ, θ, ψ) are known, $\boldsymbol{T}_n^s$ can be calculated with Equation (3-31), and in the order of ω-φ-κ the camera orientation angles can be retrieved using Equation (3-33) as:

$$
\begin{cases} \omega = atan2\left(-\boldsymbol{T}_n^s(3,2), \boldsymbol{T}_n^s(3,3)\right) \\ \varphi = asin\left(\boldsymbol{T}_n^s(3,1)\right) \\ \kappa = atan2\left(-\boldsymbol{T}_n^s(2,1), \boldsymbol{T}_n^s(1,1)\right) \end{cases}
\tag{3-35}
$$

In the order of φ-ω-κ the orientation angles can be retrieved with Equation (3-34) as:

$$
\begin{cases} \omega = \mathrm{asin}\left(-\boldsymbol{T}_n^s(3,2)\right) \\ \varphi = \mathrm{atan2}\left(\boldsymbol{T}_n^s(3,1), \boldsymbol{T}_n^s(3,3)\right) \\ \kappa = \mathrm{atan2}\left(\boldsymbol{T}_n^s(1,2), \boldsymbol{T}_n^s(2,2)\right) \end{cases}
\tag{3-36}
$$

If the camera orientation angles (ω, φ, κ) are known, $\boldsymbol{C}_n^{b_s}$ can be calculated with Equation (3-32), and the navigation orientation angles are retrieved as:

$$
\begin{cases} \phi = \mathrm{atan2}\left(\boldsymbol{C}_n^{b_s}(2,3), \boldsymbol{C}_n^{b_s}(3,3)\right) \\ \theta = \mathrm{asin}\left(\boldsymbol{C}_n^{b_s}(1,3)\right) \\ \psi = \mathrm{atan2}\left(-\boldsymbol{C}_n^{b_s}(1,2), \boldsymbol{C}_n^{b_s}(1,1)\right) \end{cases}
\tag{3-37}
$$

In general, with the knowledge of the exterior orientation parameters either from the backward intersection process or from the aiding of GNSS/INS integration, the Direct Geo-referencing system can use the method of the forward intersection or the bundle adjustment to acquire the coordinates of the ground points.

3.4 Automatic extraction of feature points of the image

The automatic methodology to detect the feature points of the images is another critical factor of photogrammetry, which determines the efficiency of process. Without a proper matching algorithm method, the speed of the output of the photogrammetry product will be not satisfied. This section will give the introduction of the principle of the feature matching, and two efficient feature methodologies will be discussed.

Before the era of digital photogrammetry, image coordinates were obtained manually by operators. Photogrammetric operators should use their eyes to locate the corresponding points on the images in stereo-plotter. With the development of digital photogrammetry systems, automatic methods have been introduced to detect the conjugate points, using the correlation of gray values. The gray matrix of an image can be expressed as (Wang and Xu 2010, Luhmann*,* *et al.* 2014, Wolf*, et al.* 2014):

$$\boldsymbol{g} = \begin{bmatrix} g_{0,0} & g_{0,1} & \cdots & g_{0,n-1} \\ g_{1,0} & g_{1,1} & \cdots & g_{1,n-1} \\ \vdots & \vdots & \ddots & \vdots \\ g_{m-1,0} & g_{m-1,1} & \cdots & g_{m-1,n-1} \end{bmatrix} \tag{3-38}$$

where, $g_{j,i}$ means the gray value of a small area of the images, and the corresponding image coordinates of the images can be calculated by (Wang and Xu 2010, Wolf *et al.* 2014):

$$\begin{aligned} x &= x_0 + i \cdot \Delta x \qquad (i = 0,1,\cdots n-1) \\ y &= y_0 + j \cdot \Delta y \qquad (j = 0,1,\cdots m-1) \end{aligned} \tag{3-39}$$

where, Δx and Δy, is the interval length of the samplings. (x_0, y_0) means the corresponding image coordinates of $g_{0,0}$.

If the target point is not at the center of the pixel, the gray value of the target point can be estimated through the bilinear resampling based on the previous gray matrix as (Wang and Xu 2010, Wolf *et al.* 2014):

$$g = \frac{1}{\Delta^2}\left[(\Delta - x_1)(\Delta - y_1)g_1 + (\Delta - y_1)x_1 g_2 + x_1 y_1 g_3 + (\Delta - x_1)y_1 g_4\right] \tag{3-40}$$

where, $\Delta = \Delta x = \Delta y$, and g_1, g_2, g_3, g_4 are the gray values around the target point g.

The gray value of the target point can be also calculated via cubic convolution method and closest pixel method (Luhmann *et al.* 2014, Wolf *et al.* 2014).

3.4.1 Area based matching method

The correlation of the gray values can be used to detect the location of the corresponding point on different images. Fig. 3-12 shows the search process of the corresponding point on two images, first, one small gray matrix $G(g_{ij})$ of $n\times n$ pixels around the interest point on the left image is calculated, and at the corresponding searching area of the right image the gray matrix $G'(g'_{ij})$ is estimated within $m\times l$ ($m>n$, $l>n$) pixels.

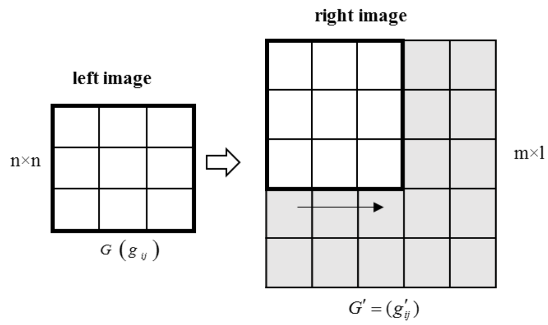

Fig. 3-12 The search process of the corresponding point at two images.

The mean values of the two gray matrices can be calculated as (Wang and Xu 2010, Luhmann *et al.* 2014, Wolf *et al.* 2014):

$$\bar{g} = \frac{1}{n^2}\sum_{i=1}^{n}\sum_{j=1}^{n} g_{i,j} \tag{3-41}$$

$$\bar{g}' = \frac{1}{n^2}\sum_{i=1}^{n}\sum_{j=1}^{n} g'_{i+k,j+h} \tag{3-42}$$

where, $\bar{g}$ means the gray value of the interest pixel group at the left images, and $\bar{g}'$ means the corresponding value at searching area of the right image.

The variances of two gray groups are (Wang and Xu 2010, Wolf *et al.* 2014):

$$\sigma_{gg} = \frac{1}{n^2}\sum_{i=1}^{n}\sum_{j=1}^{n} g^2{}_{i,j} - \bar{g}^2 \tag{3-43}$$

$$\sigma_{g'g'} = \frac{1}{n^2}\sum_{i=1}^{n}\sum_{j=1}^{n} g'_{i+k,j+h} - \bar{g}'^2_{kh} \tag{3-44}$$

And the covariance of them can be deduced as:

$$\sigma_{gg'} = \frac{1}{n^2}\sum_{i=1}^{n}\sum_{j=1}^{n} g_{i,j} g_{i+k,j+h} - \bar{g}\bar{g}' \qquad (3\text{-}45)$$

And the correlation coefficient can be written as:

$$\rho_k = \frac{\sigma_{gg'}}{\sqrt{\sigma_{gg}\sigma_{g'g'}}} \qquad (3\text{-}46)$$

Using the equation (3-46), the covariance of the interest areas of the left image and every search area of the right image can be calculated, and the total number the covariance is $m\text{-}n+1$. When ρ_k gets the maximal value, we take the center pixel of the search area as the corresponding point.

The area based matching method has some weakness when the matching points located at the low contrast area, and the success ratio won't be very high, particularly at the urban areas, because most interest area are artificial structures and buildings.

3.4.2 Feature Based Matching method

Beside the gray value matching method, the Feature Based Matching method, also named as Primitive Based Matching in computer vision, has been well developed since the seventies of last century.

SIFT/SFM method, Scale-invariant Feature Transform/Structure From Motion, one of the techniques studied in the discipline of computer vision, allows for detecting the features from overlapping images acquired by a moving camera (Lowe 1999, Lowe 2004, Snavely, et al. 2008, Furukawa and Ponce 2010). SIFT/SFM is a method for extracting distinctive invariant features from images that can be used to perform reliable matching between different views of an object or scene. The features are invariant to image scale and rotation and provide robust matching across a substantial range of affine distortion, change in 3D viewpoint, addition of noise, and change in illumination (Lowe 2004). This method includes several steps as Fig. 3-13:

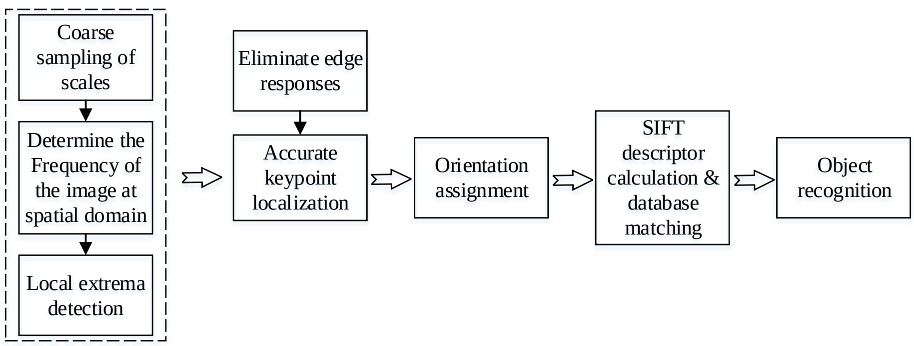

Fig. 3-13 Flowchart of the SIFT.

SFM (Structure from motion) technique can use two dimensional image sequences to build an impressive three-dimensional structure, which was also originated from computer vision field study (Dellaert *et al.* 2000, Andrew 2001), and became an efficient way to get the feature points in the area of photogrammetry. It became a low-cost, effective tool for geoscience applications (Westoby *et al.* 2012).

Traditional photogrammetric methods require the 3-D location and pose of the camera(s), or the 3-D location of ground control points to be known to facilitate scene triangulation and reconstruction. In contrast, the SFM method solves the camera pose and scene geometry simultaneously and automatically, using a highly redundant bundle adjustment based on matching features in multiple overlapping, offset images (Westoby *et al.* 2012). The SFM process can be illustrated by the following flowchart in *Fig. 3-14*.

Some commercial photogrammetric software have already introduced the algorithm of SIFT and SFM, such as “Agisoft PhotoScan” (Agisoft 2016) and “Acute 3D” produced by Bentley. Meanwhile there is also some open source software, such as “VisualSFM”, “Bundler”, “BigSFM “ and “SFMToolkit”. Some websites are also available to build the 3D models on-line with the SFM methodology, for free.

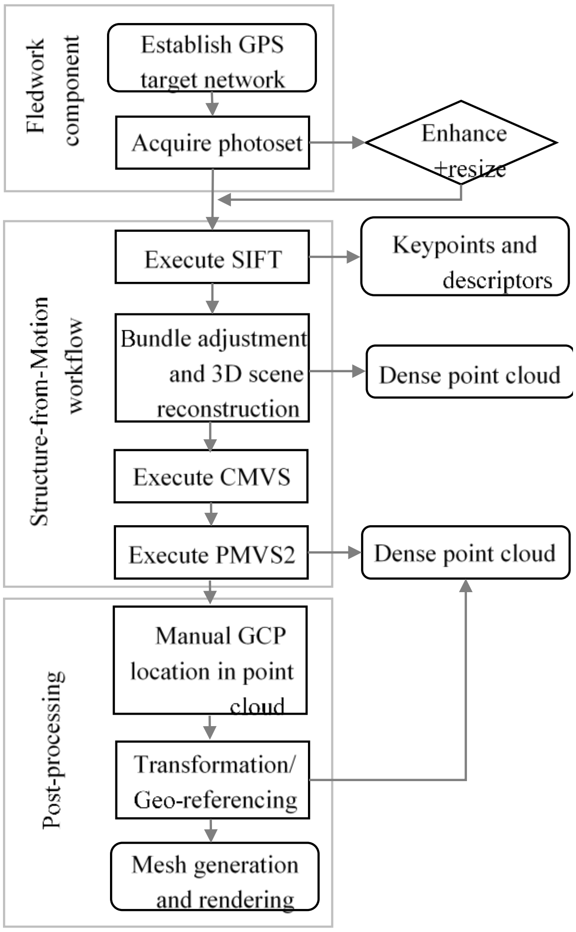

Fig. 3-14 From photograph to point-cloud: the Structure-from-Motion workflow (Westoby et al. 2012).

We managed to use the information of the orientation changes calculated by SIFT/SFM algorithm, with the help of the software of "Agisoft PhotoScan", as the additional update information for the integration of the GNSS, IMU and Images. Previous results showed that the accuracy of the relative attitude retrieved from the images has a good accurate and has a great potential to improve the performance of an integrated GNSS/IMU system (Yan *et al.* 2017).

3.5 Result and analysis

To combine the photogrammetry processes into the designed system of this thesis, the algorithms of the backward intersection, forward intersection, and the bundle adjustment are validated in practical works by the program languages of C/C++ and Matlab. In this section, two tests are presented, one was based on a commercial POS of IGI AEROcontrol, the other one was based on a low cost POS.

3.5.1 Test 1 – Anyang 2013

The first test was done on 26th December 2013, in Anyang, in the center region of China, with a transport aircraft as shown Fig. 3-15.

Fig. 3-15 The transport aircraft used in the test Anyang 2013.

During this test, the commercial POS, IGI AeroControl was used, and the accuracy of the exterior orientation parameters obtained via the software of IGI AeroOffice is shown as Table 3-1. From this table we can see that, the IGI AeroControl POS has an excellent performance of the obtained exterior orientation parameters.

Table 3-1 Statistics of the accuracy of the exterior orientation parameters obtained by the IGI AeroControl POS (Kremer and Kruck 2003).

position m	height m	roll/pitch °	yaw °
0.1	0.2	0.004	0.01

Fig. 3-16 The Overview of the TOPDC-4 camera.

The camera used was a TOPDC-4, which is a high quality camera. The overview is given in Fig. 3-16, and the specifications are given in Table 3-2.

Table 3-2 The specification of Camera TOPDC-4.

focal length (mm)	47
camera type	frame
media type	digital
pixel size (μm)	6.8×6.8
image size (pixels)	10000×14000
photo coordinate origin (pixels)	(5000, 7000)

The configuration of this test is as Fig. 3-17, the TOPDC-4 camera was mounted on an adapter platform, and the IGI AeroControl POS was mounted on the up-front of the camera.

Fig. 3-17 The configuration of the test of Anyang 2013.

The average flight height during this test was about 1000 m, the pixel size projected on the ground is around 14.5 cm, and the mean velocity was around 180 km/h. Fig. 3-18 shows the trajectory of this test. During this test, a bundle of high quality images were collected, however, only four of them are available for this thesis. The corresponding place is marked with a red ellipse.

The overlap rate of the four images is around 70%, and 15 Ground Control Points located in the four images are available, the coordinates of which were collected by the China National Administration of Surveying, Mapping and Geoinformation, which has an accuracy of 0.01 m in horizontal direction, and 0.03 m in vertical direction. The locations and the appearance of those points are shown in Fig. 3-19.

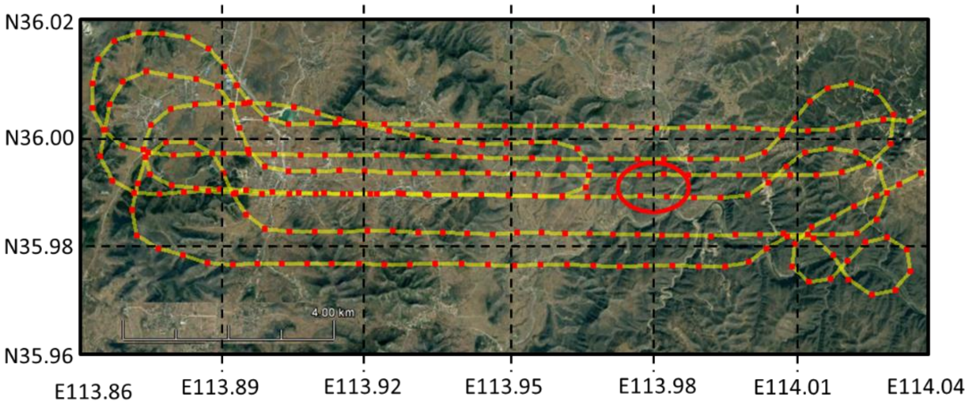

Fig. 3-18 Trajectory of the Anyang test 2013 projected in Google Earth

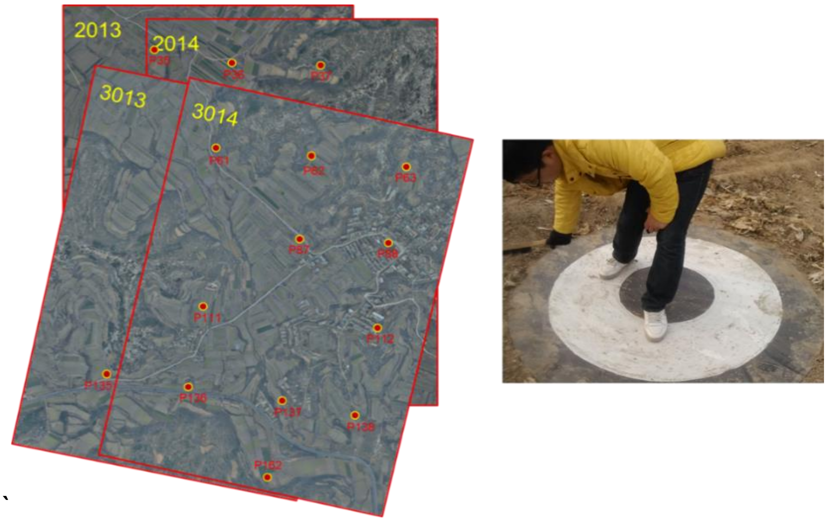

Fig. 3-19 The distribution and appearance of the GCPs of the four images.

For the assessment of the accuracy of the developed algorithms of aerial triangulation and direct georeferencing, the results from commercial photogrammetric packages like “Agisoft PhotoScan” and “ZI-Imaging ImageStation”, are used as the references.

Backward intersection test (AT)

“ZI-Imaging ImageStation” software has an outstanding function of aerial triangulation, hereby we take the output result of Aerial Triangulation as the reference to compare the result the developed backward intersection program. Table 3-3 gives the difference between the backward intersection output of the developed software and “ZI-Imaging ImageStation”.

From the table we can see that, the output of the backward intersection from the developed program is close to software “ZI-Imaging ImageStation”, the position difference is around 20 cm (with one vertical outlier in image 3014, bold text), and the attitude difference is within few hundredth of degrees.

Table 3-3 The difference between the backward intersection output of the of the developed software and “ZI-Imaging ImageStation”.

Photo ID	Backward intersection program -“ZI-Imaging ImageStation”.					
	ΔX_s /m	ΔY_s /m	ΔZ_s /m	$\Delta\omega$ /°	$\Delta\varphi$ /°	$\Delta\kappa$ /°
2013	0.009	-0.239	0.042	-0.011	0.019	-0.001
2014	-0.260	-0.219	0.010	0.017	0.019	-0.006
3013	-0.2152	0.246	0.258	0.050	-0.031	<0.001
3014	0.093	-0.020	**0.414**	0.037	-0.013	0.004

Forward intersection test (direct georeferencing)

To compare the performance of the programme of forward intersection, the software of “AGIsoft PhotoScan”, which has a good module of forward intersection, is introduced to compare the performance of the developed program. Four images are divided into two pairs for forward intersection, pair 2013-2014 and pair 3013-3014. The comparison results are shown in Table 3-4 and Table 3-5 The coordinates of the GCPs are taken as the references. From the tables we can see that, the accuracy performance of both the forward intersection program and “AGIsoft PhotoScan” software are below or close to 10 cm, except some outlier item (bold text in the tables), which means the developed software of forward intersection of this study is very accurate.

Table 3-4 The comparison of the result of forward intersection of image pair 2013-2014.

GCP ID	AGIsoft - GCPs			Forward intersection - GCPs		
	ΔE /m	ΔN /m	ΔU /m	ΔE /m	ΔN /m	ΔU /m
36	0.084	-0.160	-0.014	-0.112	0.088	0.074
37	0.099	0.015	-0.101	-0.003	0.113	-0.035
61	0.084	-0.059	0.115	0.003	0.065	-0.113
62	0.153	-0.002	0.003	0.042	0.145	-0.372
87	0.007	0.047	**0.285**	0.050	-0.144	**-0.539**
111	0.075	-0.162	-0.058	-0.073	0.136	-0.028
112	0.139	-0.006	0.074	-0.147	0.020	0.029

Table 3-5 The comparison of the result of forward intersection of image pair 3013-3014.

GCP ID	AGIsoft - GCPs			developed program - GCPs		
	ΔE /m	ΔN /m	ΔU /m	ΔE /m	ΔN /m	ΔU /m
61	0.110	-0.087	-0.105	0.036	-0.058	-0.084
62	0.055	0.064	0.066	0.024	-0.114	0.095
87	-0.088	-0.079	0.099	-0.073	-0.099	0.181
111	0.089	0.018	**-0.457**	-0.110	-0.125	**-0.344**
112	-0.137	0.041	0.200	-0.038	-0.099	0.150
137	0.074	-0.085	**0.269**	<0.001	-0.053	**0.386**

Bundle adjustment test

In this test, all four images are used for the test of the bundle adjustment, and 6 ground points were used as known points for the estimation of the exterior orientation parameters. Two grounds points (ID: 62 and 87) were used as the known points for the test the DG performance of the bundle adjustment, and distributions of ground points are as Fig. 3-20.

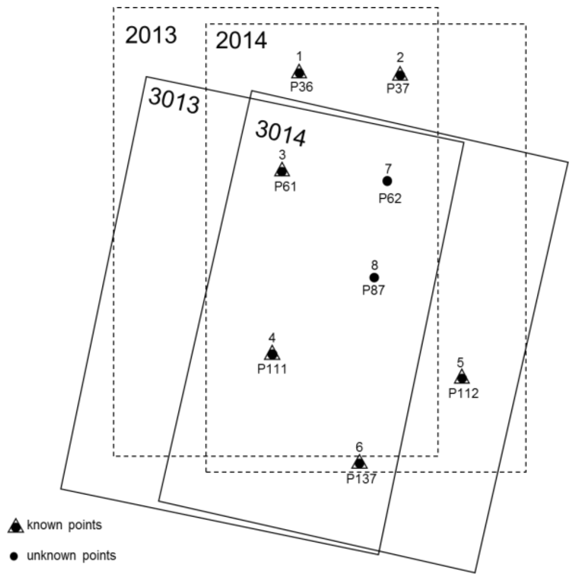

Fig. 3-20 The ground points used for the bundle adjustment test.

As in the previous tests, the exterior orientation parameters obtained by the software “ZI-Imaging ImageStation” are taken to compare the corresponding performance of the bundle adjustment, as shown in Table 3-6, while the coordinates collected by field work were used to test the accuracy of the direct geo-referencing behaviour, as shown in Table 3-7. From Table 3-6 we can see that the accuracy of exterior orientation parameters solution of bundle adjustment is also close to the software of “ZI-Imaging ImageStation”, and is equivalent to backward intersections refer to Table 3-3. From Table 3-4, Table 3-5 and Table 3-7 we can see that the accuracy of direct georeferencing is better than 6 cm, which is better than the forward intersection.

Table 3-6 The exterior orientation parameters difference between the bundle adjustment and “ZI-Imaging ImageStation” software.

Photo ID	bundle adjustment - “ZI-Imaging ImageStation”					
	ΔXs /m	ΔYs /m	ΔZs /m	$\Delta\omega$ / °	$\Delta\varphi$ / °	$\Delta\kappa$ / °
2013	-0.0982	-0.1800	-0.0194	0.0021	0.0141	-0.0034
2014	0.0360	0.0778	0.0252	-0.004	-0.0049	0.0007
3013	**-0.4257**	0.1754	0.2031	0.0682	-0.0249	-0.0007
3014	-0.0556	-0.05559	**0.4629**	0.0509	-0.0093	0.0019

Table 3-7 The coordinates difference between the bundle adjustment and GCPs.

GCD ID	bundle adjustment - GCPs		
	$\Delta X\ /m$	$\Delta Y\ /m$	$\Delta Z\ /m$
62	0.0349	0.0584	0.0139
87	0.0506	0.0431	-0.0172

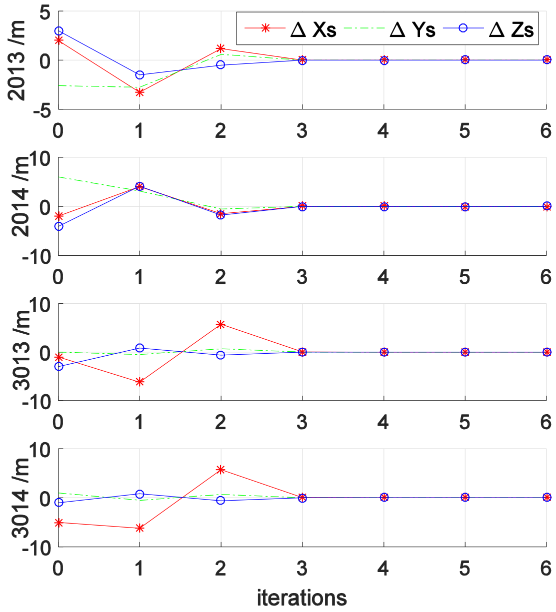

Fig. 3-21 The position exterior parameters convergence process.

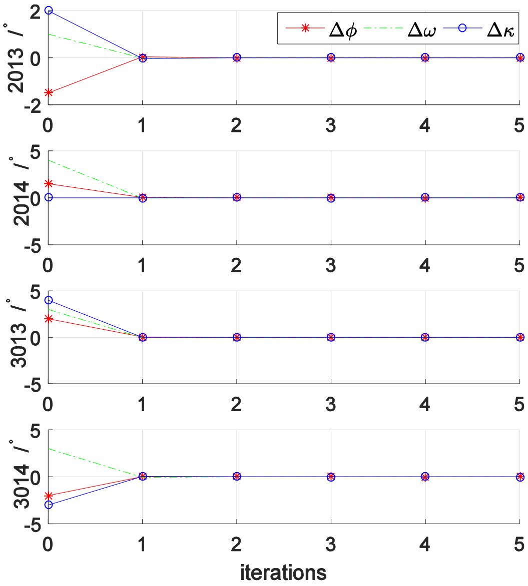

Fig. 3-22 The orientation exterior parameters convergence process.

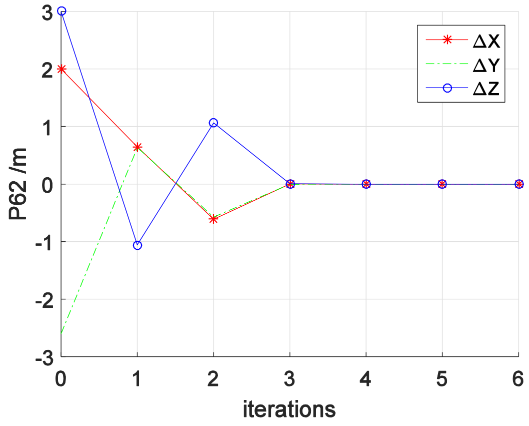

Fig. 3-23 The coordinates calculation convergence process of point 62.

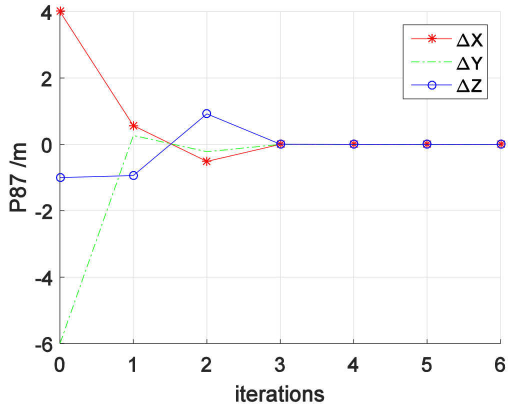

Fig. 3-24 The coordinates calculation convergence process of point 87.

Fig. 3-21 to Fig. 3-24 show the convergence process of the exterior orientation parameters calculation and the unknown points. From these figures we can see that, the calculation of exterior orientation parameters converge very fast, the difference of position exterior orientation parameters converge from several meters to zero in 3 iterations, the orientation elements converge from several degree to zero in 1-2 iterations, and the coordinates of the unknown points converge from several meters to zeros in 3-4 iterations.

3.5.2 Test 2 – Espinho 2016

The second test was done on 9th December 2016, near Espinho in the north of Portugal, using a small light airplane. The POS used this test, consists of a NovAtel dual frequency GNSS receiver, a tactical IMU, and a Litton LN-200. The accuracy of the exterior orientation parameters derived from the integration GNSS/Litton, using the software previously developed at OAUP, can reach a few centimeters for the position parameters, and can be better than 0.05° for the orientation parameters (Tomé 2002, Deurloo 2011). The Sony ICX-204AK CCD camera, which is a low cost camera, was used for images acquisition, and its specifications are given in Table 3-8.

Table 3-8 The specification of Camera Sony ICX-204AK CCD

focal length (mm)	6
pixel size ($\mu m \times \mu m$)	4.65×4.65
image size in pixels	1024×768

The configuration of this test was described in Fig. 3-25: the LN-200 was mounted inside the body of the airplane, the GPS antenna was installed on the top of the right wing, and the camera was rigidly attached beneath.

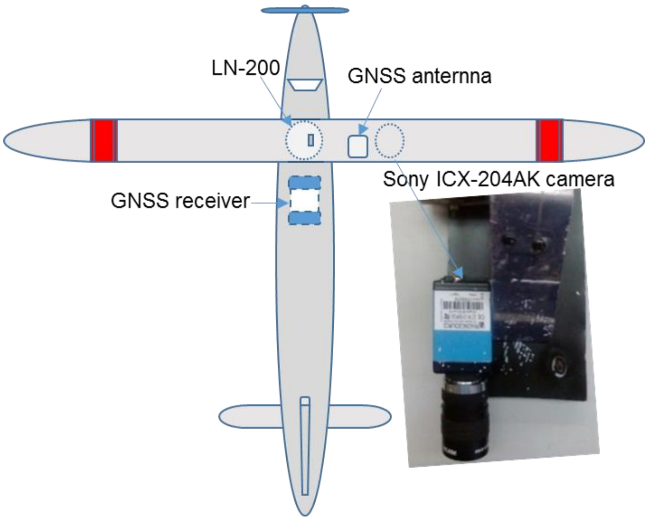

Fig. 3-25 The configuration of the test of Esphinho 2016

The average flight height during this test was about 375 m, and the mean velocity was around 180 km/h. The corresponding pixel size on the ground was of around 30 cm. There were 46 known ground points, 8 of them were obtained from the GPS RTK survey, with an accuracy of around 0.02 m in horizontal direction, and 0.05 m in vertical direction, which were used for the aerial triangulation; 38 points were collected from an orthophoto and a DEM available from a coastal survey of the Portuguese Geographic Institute, with an accuracy of around 0.20 m in horizontal direction, and 0.30 m in vertical direction, which were used for assessing the performance of the direct georeferencing. Those 46 ground control points are mainly distributed on the ground along the trajectory, and the place are marked with a yellow circle as shown in Fig. 3-26, and a subset of this data was chosen to be analysed. The overlap rate of the successive images along the red strip is 60%. A total of 20 images were selected to assess the performance of the developed methods in this chapter.

Fig. 3-26 Trajectory of the Espinho test 2016 projected in Google Earth, and the distribution of the ground points..

Backward intersection test (AT)

Fig. 3-27 gives the differences of GNSS/Litton and the "Agisoft PhotoScan" AT (only with GCPs) in this test, and Table 3-9 is the statistics of the difference (value and boresight were compensated).

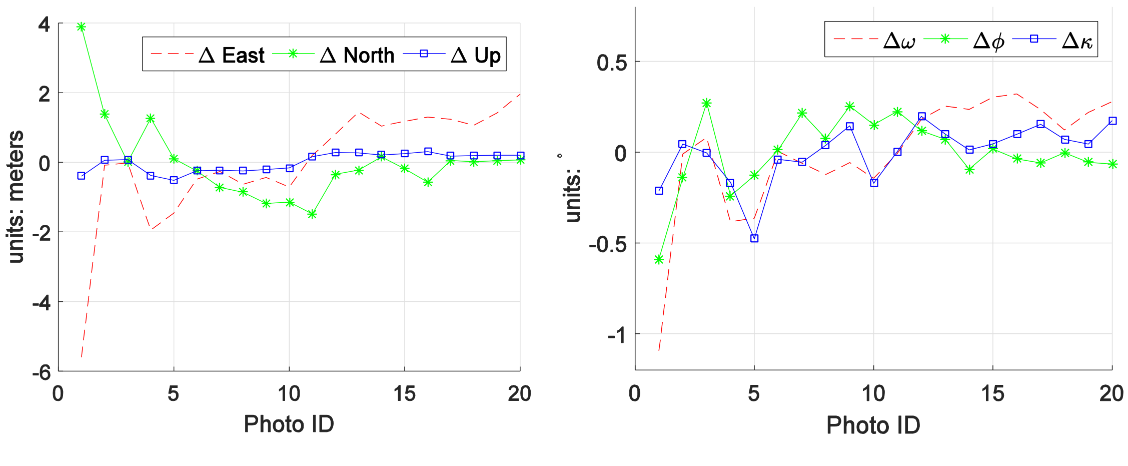

(a) position difference (b) orientation difference

Fig. 3-27 Differences of GNSS/Litton and the "AGIsoft PhotoScan" AT (only with GCPs)

Table 3-9 Statistics of differences between GNSS/Litton and the “AGIsoft PhotoScan” AT (only with GCPs)

	GNSS/Litton – AGIsoft AT					
	$\Delta E\ /m$	$\Delta N\ /m$	$\Delta U\ /m$	$\Delta\omega$ / °	$\Delta\varphi$ / °	$\Delta\kappa$ / °
min	-5.598	-1.485	-0.518	-1.093	-0.589	-0.477
max	**1.957**	**3.886**	0.307	0.320	0.271	0.197
std	**1.644**	**1.127**	**0.267**	**0.321**	**0.193**	**0.155**

From Fig. 3-27 and Table 3-9 we can see that, std (standard deviation) values of three orientation exterior parameters are 0.321°, 0.193° and 0.155°; in the up direction, the standard deviation value is 0.267 *m*, which means that, using the developed GNSS/Litton POS mounted on a small light airborne vehicle, the accuracy of the orientation and the position in up direction meet the demand of the requirement of the geodetic photogrammetry work. However, in the horizontal direction, the standard deviation values are 1.644 *m*, 1.127 *m*, which are much higher than the up direction, which is not enough for the geodetic photogrammetric applications.

The large mismatch of the horizontal positon between the GNSS/Litton POS and aerial triangulation doesn’t mean the GNSS/Litton POS has unsatisfied performance in the positioning, and this mismatch is mainly due the exposure time errors from the low cost cameras, which includes two parts, one is the unsynchronization error from the GNSS time system, and the other one is the exposure time delay. From our experience, the unsynchronization error is less than 1 *ms*. The mean velocity for this test was 180 *km/h,* for which corresponding position errors caused by time unsynchronization is 0.05 *m*; the exposure time delay is the time postpone of the digital images are completed after the camera exposure event, which are not constant values and sometimes may reach even more than 50 milliseconds, originating the positioning error that can reach 2.5 *m*, which is matching the mean values of 2~3 *m* mismatching in the horizontal direction between the GNSS/Litton POS and the aerial triangulation.

Forward intersection (direct georeferencing)

Because of the existing exposure time delay of this low cost cameras, the position exterior parameter is not proper to be taken as the input of the direct georeferencing. Therefore, the exterior orientation parameters obtained by the “Agisoft PhotoScan” AT based on the 46 ground points, was directly used as the input of the direct georeferencing program developed in this thesis. Points number from 801 to 838 of the ground points, were used as the reference to assess the performance of direct georeferencing. Fig. 3-28 gives the difference between the DG result and the GCPs, and the Table 3-10 gives the statistics of the difference.

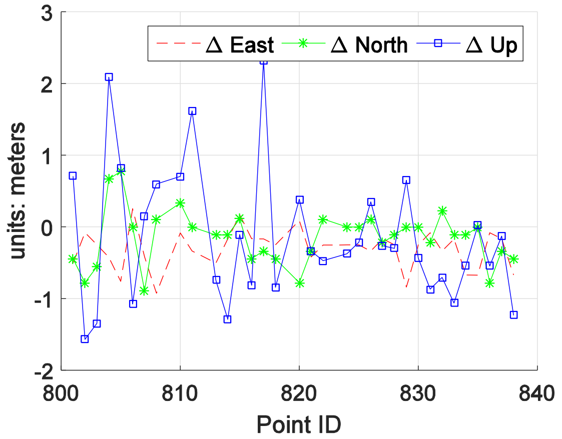

Fig. 3-28 Differences between direct georeferencing and the GCPs.

Table 3-10 Statistics of the differences between direct georeferencing and the GCPs

	DG-GCPs		
	ΔE /*m*	ΔN /*m*	ΔU /*m*
min	**-0.926**	**-0.890**	**-1.568**
max	0.252	**0.774**	2.324
mean	-0.306	-0.151	-0.142
rms	0.271	0.376	**0.931**

From Fig. 3-28 and Table 3-10 we can see that, the horizontal accuracy of our direct georefencing is, around 0.3 m in horizontal direction, and 0.93 m in the vertical direction, which are not very precise, mainly due to the reason of the quality of the GCPs.

3.6 Summary

During this chapter, the algorithm of backward intersection, forward intersection and bundle adjustment were discussed in detail. The principle and calculation process of the SIFT/SFM methodology are also studied, which will be mainly validated by the software of "Agisoft Photoscan", and will be discussed in later chapters.

These functions were programed and their results were validated in two tests. Results from the test of Anyang 2013 using a commercial POS show that, the accuracy of the developed program is comparable to the commercial photogrammetry software. Results from the test of Espinho 2016 using a developed POS show that, there is also a good matching of the exterior orientation parameters between the developed algorithm and aerial triangulation. However due to the existing exposure time delay of this low cost camera, it is still a challenge for using a low-cost Direct Georeferencing System to achieve the position and attitude information as precise as the commercial ones. We are aware of these problems of the exposal time error, but it is difficult to estimate them precisely at this moment.

Therefore, according to the obtained conclusion that the existing exposure time delay of the low cost camera, we make an assumption that the affection of the orientation parameters obtained by the proposed low cost POS is not as sensitive as position parameters, and some strategies to improve the orientation performance of the low cost POS will be discussed in later chapters

4 Kalman Filter

The Least-squares method is the most common way to estimate a state vector in geomatics, which is purely based on measurements, using usually a single estimation procedure to process all the dataset at once (some details are given in Appendix B). Unlike conventional Least-squares method, sequential Least-squares involves a set of iteration equations, which doesn't require the knowledge of the whole dataset, and can be easily validated in computer calculations. For applications with a large dataset, the conventional Least-squares method becomes not practical, and it is more efficient to use a sequential or recursive approach. As a typical sequential Least-squares method, Kalman Filter plays an important role in geodetic applications (Yang and Gao 2006, Savage 2016), particular in the integration of GNSS and IMU observations (Godha and Cannon 2007, Lee *et al.* 2016).

In this chapter, we give an introduction to the basic algorithm of the Kalman filter. The definitions of the essential reference frames, the inertial navigation equations, as well as different coupling strategies, loosely coupled and tightly coupled, for the integration of GNSS and Inertial observations are discussed in detail.

4.1 Reference frames

The fundamental of the technique of GNSS/IMU navigation involves a number of Cartesian coordinate reference frames. Each frame is an orthogonal, right-handed, coordinate system axis set. The main coordinate frames used in this thesis in the context of the GNSS/IMU integration are summarized in Fig. 4-1.

The inertial frame, i-frame, has its origin at the center of the Earth, and axes Ox_i, Oy_i, Oz_i (shown in Fig. 4-1), which are none-rotating with respect to the fixed stars. The pole axis Oz_i of the *i*-frame is coincident with the Earth Polar axis.

The Earth frame, e-frame, has its origin at the center of the Earth, and axes Ox_e, Oy_e, Oz_e (shown in Fig. 4-1) which are fixed with respect to the Earth. The axis Ox_e lies along the intersection of the plane of the Greenwich meridian with the Earth's equatorial plane and the pole axis Oz_e of the e-frame is along the Earth's pole axis. The Earth frame rotates at a rate $\omega_e = 7292115\times10^{-11}$

radians/second (NIMA 2000), with respect to the axis Oz_i of the inertial frame.

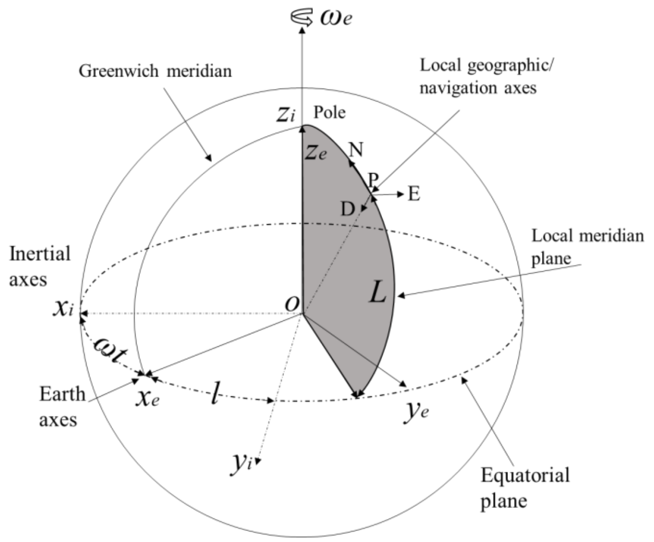

Fig. 4-1 Frames of reference (Titterton and Weston 2004)

The navigation frame, n-frame, has its origin at the location of the navigation system, point P (shown in Fig. 4-1), and axes that are aligned with the local directions north, east and local vertical (down) respectively. The turn rate of the n-frame, ω_{en}, with respect to the Earth-fixed frame, is governed by the motion of the point P with respect to the Earth. This is often referred to as the transport rate.

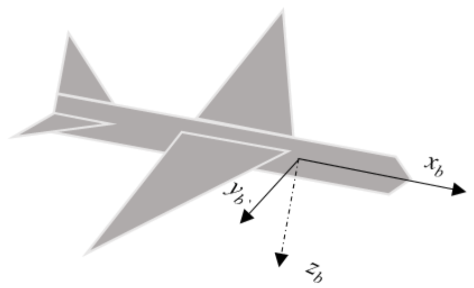

Fig. 4-2 A body frame

The body frame, b-frame, is an orthogonal axis set (shown in Fig. 4-2), which is aligned with the roll, pitch and yaw axes of the platform, in which the navigation system is installed.

4.2 Introduction to Kalman Filter

Similarly to the Least-square method, the Kalman Filter is designed for the case of a linear system, which is based on the knowledge of the measurements and the process dynamics. However, the extended Kalman Filter plays an important role for the case of a none-linear system, which is particularly useful for the integration of GNSS and inertial observations (Lin 2015, Lee et al. 2016).

Three basic assumptions are normally adopted for the derivation used in Kalman Filter (Gelb 1974):

1) the system has a linear model;

2) the state vector contains all information accumulated by the system before current epoch;

3) noise is “white” and has a Gaussian probability density distribution.

Based on these assumptions the Kalman Filter equations are presented/resumed in the following sections.

4.2.1 In linear systems

In a linear system, the mechanical expression of a general linear system can be represented by a first-order stochastic differential equation as:

$$\dot{\boldsymbol{x}}(t) = \boldsymbol{F}(t)\boldsymbol{x}(t) + \boldsymbol{G}(t)\boldsymbol{w}(t) \tag{4-1}$$

where, $\boldsymbol{x}(t)$ is the system state vector, $\boldsymbol{w}(t)$ is the zero-mean Gaussian white noise, with a power spectral density of $\boldsymbol{Q}$, $\boldsymbol{F}(t)$ is the system matrix, and $\boldsymbol{G}(t)$ is the noise mapping matrix.

A possible solution for Equation (4-1) can be derived as (Gelb 1974):

$$\boldsymbol{x}(t) = \boldsymbol{\Phi}(t, t_0)\boldsymbol{x}(t_0) + \int_{t_0}^{t} \boldsymbol{\Phi}(t,\tau)\boldsymbol{G}(t,\tau)\boldsymbol{w}(\tau)d\tau \tag{4-2}$$

where, $\boldsymbol{\Phi}(t, \tau)$ represents the state transition matrix that explains the linear system changes from time τ to t, and the state transition is the solution of the differential equation:

$$\frac{d}{dt}\boldsymbol{\Phi}(t,\tau) = \boldsymbol{F}(t)\boldsymbol{\Phi}(t,\tau) \tag{4-3}$$

if $\boldsymbol{F}(t)$ is considered as constant during the interval $\Delta t = t - \tau$, then the state transition matrix can be solved as (Gelb 1974):

$$\boldsymbol{\Phi}(t,\tau) = e^{\boldsymbol{F}(t)\Delta t} = \boldsymbol{I} + \boldsymbol{F}(t)\Delta t + \frac{1}{2!}\left(\boldsymbol{F}(t)\Delta t\right)^2 + \frac{1}{3!}\left(\boldsymbol{F}(t)\Delta t\right)^3 \tag{4-4}$$

Normally the available measurement of the system can be expressed as (Gelb 1974):

$$\boldsymbol{z}(t) = \boldsymbol{H}(t)\boldsymbol{x}(t) + \boldsymbol{v}(t) \tag{4-5}$$

where, $\boldsymbol{z}$ is the measurement vector and $\boldsymbol{H}$ is the measurement matrix, $\boldsymbol{v}$ represents the measurement noise, which is also a zero-mean Gaussian white noise, with power spectral density $\boldsymbol{R}$.

For the discrete sampling points, the mechanical equation becomes (Gelb 1974, Titterton and Weston 2004):

$$\boldsymbol{x}_i = \boldsymbol{\Phi}_{i-1}\boldsymbol{x}_{i-1} + \boldsymbol{u}_{i-1} \tag{4-6}$$

with the measurements:

$$\boldsymbol{z}_i = \boldsymbol{H}_i\boldsymbol{x}_i + \boldsymbol{v}_i \tag{4-7}$$

The best estimation of the state vector can be denoted as $\tilde{\boldsymbol{x}}_{i/i-1}$, since the system noise $\boldsymbol{u}_{i-1}$ has zero mean, then the prediction process can be given as (Titterton and Weston 2004):

$$\tilde{\boldsymbol{x}}_{i/i-1} = \boldsymbol{\Phi}_{i-1}\tilde{\boldsymbol{x}}_{i-1/i-1} \tag{4-8}$$

and the covariance matrix of the expected state vector at time t_i predicted from time t_{i-1} can be written as:

$$\boldsymbol{P}_{i/i-1} = \boldsymbol{\Phi}_{i-1}\boldsymbol{P}_{i-1/i-1}\boldsymbol{\Phi}_{i-1}{}^{\mathrm{T}} + \boldsymbol{G}\boldsymbol{Q}_{i-1}\boldsymbol{G} \tag{4-9}$$

Once the measurement z_i arrives, the process of the measurement update starts. The best estimation of the state at time t_i can be calculated as (Titterton and Weston 2004):

$$\tilde{\boldsymbol{x}}_{i/i} = \tilde{\boldsymbol{x}}_{i/i-1} + \boldsymbol{K}_i[\boldsymbol{z}_i - \boldsymbol{H}_i\tilde{\boldsymbol{x}}_{i/i-1}] \tag{4-10}$$

and its covariance matrix is given by:

$$\boldsymbol{P}_{i/i} = [\boldsymbol{I} - \boldsymbol{K}_i\boldsymbol{H}_i]\boldsymbol{P}_{i/i-1} \tag{4-11}$$

where the Kalman gain matrix is defined by:

$$\boldsymbol{K}_i = \boldsymbol{P}_{i/i-1}\boldsymbol{H}_i[\boldsymbol{H}_i\boldsymbol{P}_{i/i-1}\boldsymbol{H}_i{}^{\mathrm{T}} + \boldsymbol{R}_i]^{-1} \tag{4-12}$$

For the applying of a Kalman Filter, the linear mechanical navigation equation is essential. But for a none-linear system, the mechanical equation can be deal with an extended Kalman Filter, with the help of linearization.

4.2.2 In none-linear systems:

The Kalman Filter for the none-linear systems can be named as extended Kalman Filter, and the mechanical equation can be expressed as (Gelb 1974, Titterton and Weston 2004):

$$\frac{d\boldsymbol{x}}{dt} = \boldsymbol{f}(\boldsymbol{x},t)\boldsymbol{x}(t) + \boldsymbol{g}(\boldsymbol{x},t)\boldsymbol{w}(t) \tag{4-13}$$

With the discrete measurements equation given by:

$$\boldsymbol{z} = \boldsymbol{h}(x,t) + \boldsymbol{v}(t) \tag{4-14}$$

Equations (4-13) and (4-14) can be simplified as (Titterton and Weston 2004):

$$\begin{aligned} \frac{d\tilde{\boldsymbol{x}}}{dt} &= \boldsymbol{f}(\tilde{\boldsymbol{x}})\tilde{\boldsymbol{x}} + \boldsymbol{g}(\tilde{\boldsymbol{x}})\boldsymbol{w} \\ \tilde{\boldsymbol{z}} &= \boldsymbol{h}(\tilde{\boldsymbol{x}}) + \boldsymbol{v} \end{aligned} \tag{4-15}$$

where, $\boldsymbol{f}(\tilde{\boldsymbol{x}})$, $\boldsymbol{g}(\tilde{\boldsymbol{x}})$ and $\boldsymbol{h}(\tilde{\boldsymbol{x}})$ are the approximations by the linearization technique using Taylor series, i.e. the function $\boldsymbol{f}(\boldsymbol{x}, t)$ is approximated by:

$$\boldsymbol{f}(\boldsymbol{x},t) = \boldsymbol{f}(\tilde{\boldsymbol{x}}) + \frac{d\boldsymbol{f}}{dt}(\boldsymbol{x} - \tilde{\boldsymbol{x}}) + \frac{d^2\boldsymbol{f}}{dt^2}\frac{(\boldsymbol{x} - \tilde{\boldsymbol{x}})^2}{2} + \cdots \tag{4-16}$$

Substituting in the original equations, the differential equations governing the derivations can be written as (Brown and Hwang 1997):

$$\begin{aligned} \frac{d\delta\boldsymbol{x}}{dt} &= \boldsymbol{F}\delta\boldsymbol{x} + \boldsymbol{G}\boldsymbol{w} \\ \delta\boldsymbol{z} &= \boldsymbol{H}\delta\boldsymbol{x} + \boldsymbol{v} \end{aligned} \tag{4-17}$$

where, $\boldsymbol{F} = \frac{d\boldsymbol{f}}{dt}|_{\tilde{x}}$, $\boldsymbol{G} = \frac{d\boldsymbol{g}}{dt}|_{\tilde{x}}$ and $\boldsymbol{H} = \frac{d\boldsymbol{h}}{dt}|_{\tilde{x}}$.

The expressions for the time discrete points are similar to the equations (4-6) to (4-12).

The extended Kalman Filter is the theoretical foundation for our GNSS/IMU integration (see Chapter 5), as well as the integration development with other aiding sources/sensors. For implementing the extended Kalman Filter in the GNSS/IMU integration, the mechanical navigation equations based on the IMUs observation must be set rigorously.

4.3 Inertial mechanical navigation equations

In the Kalman Filter mechanical equations, the position, velocity and orientation computed in the navigation frame, combined with other information, such as sensors errors, are taken as the states of the filter. In this thesis, we have used a 15-dimensional state vector for the extended Kalman Filter described as:

$$\boldsymbol{x} = \begin{bmatrix} \boldsymbol{r}^n & \boldsymbol{v}^n & \boldsymbol{\phi}^n & \boldsymbol{b}_a & \boldsymbol{b}_\omega \end{bmatrix}^{\mathrm{T}} \tag{4-18}$$

where, the 15-dimensional state vector comprises: three position coordinates $\boldsymbol{r}^n = [L\ l\ h]^{\mathrm{T}}$ that refers to the latitude, longitude and height, three velocities $\boldsymbol{v}^n = [v_N\ v_E\ v_D]^{\mathrm{T}}$, which are the velocities in north, east and down directions, three orientation angles $\boldsymbol{\phi}^n = [\phi\ \theta\ \psi]^{\mathrm{T}}$, the Euler angles rotated from the navigation frame to the body frame, and six constant biases, $\boldsymbol{b}_a$ and $\boldsymbol{b}_\omega$.

An inertial measurement unit normally has three orthogonal gyroscopes and three accelerometers. The gyroscopes and accelerometers measure the axis rotation angle rates and the accelerations, respectively, with respect to the inertial space. However, the accelerometers can't separate the total acceleration, the acceleration with respect to the inertial space, from the true acceleration in space and the gravity acceleration, thus, the accelerometer measurement is the algebraic sum of the acceleration with respect to the inertial space and the gravitational acceleration (Jekeli and Kwon 2002, Titterton and Weston 2004). The axis rotation angles measured by the gyroscopes are used to calculated the orientation angles of the IMUs from the body frame to the navigation frame, then the velocity and the position in the navigation frame can be obtained by twice integrating the acceleration sensed by the accelerometers.

The three velocities parameters in the navigation frame can be defied as (Jekeli 2001a):

$$\boldsymbol{v}^n = \begin{bmatrix} v_N \\ v_E \\ v_D \end{bmatrix} = \begin{bmatrix} M+h & 0 & 0 \\ 0 & (N+h)\cos\varphi & 0 \\ 0 & 0 & -1 \end{bmatrix} \begin{bmatrix} \dot{L} \\ \dot{l} \\ \dot{h} \end{bmatrix} \tag{4-19}$$

Hence, the time derivative of the coordinates can be written as:

$$\dot{r}^n = \begin{bmatrix} \dot{L} \\ \dot{l} \\ \dot{h} \end{bmatrix} = \boldsymbol{D}^{-1} \begin{bmatrix} v_N \\ v_E \\ v_D \end{bmatrix} \tag{4-20}$$

where, $\boldsymbol{D}^{-1} = diag[1/(M+h)\ 1/(N+h)\cos\varphi\ {-1}]$,

and the corresponding parameters are defined in the WGS84 (World Geodetic System 1984) frame as (NIMA 2000, Titterton and Weston 2004):

the length of the semi-major axis,	$R = 6378137.0\ m$
the length of the semi-minor axis,	$r = R(1\text{-} f) = 6356752.3142\ m$
the flattening of the ellipsoid,	$f = (R - r) / R = 298.257223563$
the major eccentricity of the ellipsoid,	$\mathrm{e} = [f(2 - f)]^{1/2} = 8.1819190842622 \times 10^{-2}$

the meridian radius of curvature, $M = \frac{R\left(1 - \mathrm{e}^2\right)}{\sqrt[3/2]{1 - \mathrm{e}^2 \sin^2\phi}}$

the prime vertical radius of curvature, $N = \frac{R}{\sqrt{1 - \mathrm{e}^2 \sin^2\phi}}$

the navigation equation can be expressed as (Jekeli 2001b, Titterton and Weston 2004):

$$\dot{\boldsymbol{v}}^n = \boldsymbol{f}^n - \left(2\boldsymbol{\omega}_{ie}^n + \boldsymbol{\omega}_{en}^n\right) \times \boldsymbol{v}^n + \boldsymbol{g}^n \tag{4-21}$$

or in a component form as:

$$\begin{aligned}
\dot{v}_N &= f_N - 2\omega_e v_E \sin L + \frac{v_N v_D - v_E{}^2 \tan L}{R_0 + h} + \xi g \\
\dot{v}_E &= f_E + 2\omega_e \left(v_N \sin L + v_D \cos L\right) + \frac{v_E}{R_0 + h}\left(v_D + v_N \tan L\right) - \eta g \\
\dot{v}_D &= f_D - 2\omega_e v_E \cos L - \frac{v_E{}^2 + v_N{}^2}{R_0 + h} + g
\end{aligned} \tag{4-22}$$

where, ξ and η represent angular deflections in the direction of the local gravity vector with respect to the local vertical, owing to gravity anomalies, ω_e is the rotation velocity of the earth, R_0 is the radius of the earth, g represents the gravity anomalies. $\boldsymbol{f}^n = [f_N \quad f_E \quad f_D]^T$ represents the specific force vector in the navigation frame, $\boldsymbol{\omega}_{ie}^n = [\omega_e \cos L \;\; 0 \;\; -\omega_e \sin L]^T$ represents the earth rotation rate in the navigation frame. The earth rotation rate in the navigation frame with respect to the Earth-fixed frame $\boldsymbol{\omega}_{en}^n$ can be written as (Titterton and Weston 2004):

$$\boldsymbol{\omega}_{en}^n = \begin{bmatrix} \frac{v_E}{N + h} & \frac{-v_N}{M + h} & \frac{-v_E / \tan L}{M + h} \end{bmatrix}^T \tag{4-23}$$

The three attitude parameters, normally are expressed by the direction cosine matrix $\boldsymbol{C}_b^n$, and can be written as (Titterton and Weston 2004):

$$\boldsymbol{C}_b^n = \begin{bmatrix} \cos\theta\cos\psi & -\cos\phi\sin\psi + \sin\phi\sin\theta\cos\psi & \sin\phi\sin\psi + \cos\phi\sin\theta\cos\psi \\ \cos\phi\sin\psi & \cos\phi\cos\psi + \sin\phi\sin\theta\sin\psi & -\sin\phi\cos\psi + \cos\phi\sin\theta\sin\psi \\ -\sin\theta & \sin\phi\cos\theta & \cos\phi\cos\theta \end{bmatrix} \tag{4-24}$$

The attitude dynamic equation is defined as (Jekeli 2001b, Titterton and Weston 2004):

$$\dot{\boldsymbol{C}}_b^n = \boldsymbol{C}_b^n \boldsymbol{\Omega}_{nb}^b \tag{4-25}$$

where, $\boldsymbol{\Omega}$ represents the skew symmetric matrix from the vector $\boldsymbol{\omega}$, and $\boldsymbol{\omega}_{nb}^b$, which can be calculated by:

$$\boldsymbol{\omega}_{nb}^{b} = \boldsymbol{\omega}_{ib}^{b} - \boldsymbol{C}_{b}^{n}\left[\boldsymbol{\omega}_{ie}^{n} + \boldsymbol{\omega}_{en}^{n}\right] \tag{4-26}$$

where, $\boldsymbol{\omega}_{ib}^{b}$ are the outputs from the strapdown gyros.

In summary, the inertial mechanical navigation equations can be described by Equation (4-20), (4-21) and (4-25) as:

$$\begin{bmatrix} \dot{\boldsymbol{r}}^{n} \\ \dot{\boldsymbol{v}}^{n} \\ \dot{\boldsymbol{C}}_{b}^{n} \end{bmatrix} = \begin{bmatrix} \boldsymbol{D}^{-1}\boldsymbol{v}^{n} \\ \boldsymbol{f}^{n} - \left(2\boldsymbol{\omega}_{ie}^{n} + \boldsymbol{\omega}_{en}^{n}\right)\times\boldsymbol{v}^{n} + \boldsymbol{g}^{n} \\ \boldsymbol{C}_{b}^{n}\boldsymbol{\Omega}_{nb}^{b} \end{bmatrix} \tag{4-27}$$

With the observation of the IMUs, and the knowledge of the corresponding Earth parameters, the position, velocity and orientation, in a total of 9 parameters of the state vector, can be calculated through the equation (4-27) with the integral of time. The other 6 parameters, the sensor biases, will be kept as constant until the update measurement happens, the process will be discussed in the following sections.

4.4 Applying the Kalman Filter

The parameters of interest, such as position, velocity and orientation of our dynamic system can be initially estimated through a dedicated configuration of the mechanical navigation as Equation (4-27). However, this equation is not linear, therefore, to apply the Kalman Filter, the mechanical equation of the navigation system has to be linearized through the equation (4-15), which becomes the extended Kalman Filter. The setup of the extended Kalman Filter includes two parts: a predict process and a measurement update. The prediction process is used for the prediction of the errors of the corresponding states of position, velocity and orientation associated with the IMUs observations. In the measurement update phase, these errors can be estimated using the updated measurements which, in the approach proposed in this thesis, mainly refer to the GNSS and image geometric information. The details of the prediction process and update measurement for a 15-state GNSS/IMU extended Kalman Filter are given below.

4.4.1 The prediction process

During the linearization process, the related error states corresponding to Equation (4-18) are:

$$\delta\boldsymbol{x} = \left[\delta\boldsymbol{r}^{n} \quad \delta\boldsymbol{v}^{n} \quad \delta\boldsymbol{\phi}^{n} \quad \varepsilon\boldsymbol{b}_{a} \quad \varepsilon\boldsymbol{b}_{\omega}\right]^{\mathrm{T}} \tag{4-28}$$

For the application of the Kalman Filter, the noise of the state vectors must be “white”, and the system model of the state vectors must be linear. For a none-linear system, the dynamic predict equation can be written as:

$$\dot{\boldsymbol{x}} = \boldsymbol{f}\left(\boldsymbol{x}\right) + \boldsymbol{D}\boldsymbol{\omega} \tag{4-29}$$

where $\boldsymbol{D}$ is the input vector noise mapping matrix, $\boldsymbol{\omega}$ is the process noise and $\boldsymbol{f}(\boldsymbol{x})$ is a none-linear vector function.

According to Equation (4-17), using the first order Taylor series expression, the error dynamic equation can be written in a linear form as (Brown and Hwang 1997):

$$\delta\dot{\boldsymbol{x}} = \boldsymbol{F}\delta\boldsymbol{x} + \boldsymbol{G}\boldsymbol{w} \tag{4-30}$$

where system matrix $\boldsymbol{F} = \left.\frac{\partial f}{\partial x}\right|_{x=\hat{x}}$ represents the partial derivatives of the states, and $\boldsymbol{G}$ is the noise mapping matrix of the state error. Detailed expressions for $\boldsymbol{F}$ and $\boldsymbol{G}$ can be written as (Shin 2001, Titterton and Weston 2004):

$$\boldsymbol{F} = \begin{bmatrix} \frac{\partial \dot{\boldsymbol{r}}_e^n}{\partial \boldsymbol{r}_e^n} & \frac{\partial \dot{\boldsymbol{r}}_e^n}{\partial \boldsymbol{v}_e^n} & \boldsymbol{0} & \boldsymbol{0} & \boldsymbol{0} \\ \frac{\partial \dot{\boldsymbol{v}}_e^n}{\partial \boldsymbol{r}_e^n} & \frac{\partial \dot{\boldsymbol{v}}_e^n}{\partial \boldsymbol{v}_e^n} & \frac{\partial \dot{\boldsymbol{v}}_e^n}{\partial \boldsymbol{\phi}^n} & \boldsymbol{C}_b^n & \boldsymbol{0} \\ \frac{\partial \dot{\boldsymbol{\phi}}^n}{\partial \boldsymbol{r}_e^n} & \frac{\partial \dot{\boldsymbol{\phi}}^n}{\partial \boldsymbol{v}_e^n} & \frac{\partial \dot{\boldsymbol{\phi}}^n}{\partial \boldsymbol{\phi}^n} & \boldsymbol{0} & \boldsymbol{C}_b^n \\ \boldsymbol{0} & \boldsymbol{0} & \boldsymbol{0} & \boldsymbol{0} & \boldsymbol{0} \\ \boldsymbol{0} & \boldsymbol{0} & \boldsymbol{0} & \boldsymbol{0} & \boldsymbol{0} \end{bmatrix}_{15\times15} \quad \boldsymbol{G} = \begin{bmatrix} \boldsymbol{0} & \boldsymbol{0} \\ \boldsymbol{C}_b^n & \boldsymbol{0} \\ \boldsymbol{0} & -\boldsymbol{C}_b^n \\ \boldsymbol{0} & \boldsymbol{0} \\ \boldsymbol{0} & \boldsymbol{0} \end{bmatrix}_{15\times6} \tag{4-31}$$

Then, for our type of application we can use the typical Kalman Filter dynamic equation in a time discrete form as the equations (4-8) and (4-9):

$$\begin{aligned} \delta\boldsymbol{x}_{i/i-1} &= \boldsymbol{\Phi}_{i-1}\delta\boldsymbol{x}_{i\text{-}1/i-1} \\ \boldsymbol{P}_{i/i-1} &= \boldsymbol{\Phi}_{i-1}\boldsymbol{P}_{i-1/i-1}\boldsymbol{\Phi}_{i-1}{}^{\mathrm{T}} + \boldsymbol{Q}_{i-1} \end{aligned} \tag{4-32}$$

where, the subscript i is the current index of discrete samplings; $\boldsymbol{\Phi}_{i\text{-}1}$ is the prediction of the system matrix, which can be approximated by a third order equation according to Equation (4-4):

$$\boldsymbol{\Phi}_{i-1} \approx \boldsymbol{I} + \boldsymbol{F}_{i-1}\Delta t + \frac{1}{2!}(\boldsymbol{F}_{i-1}\Delta t)^2 + \frac{1}{3!}(\boldsymbol{F}_{i-1}\Delta t)^3 \tag{4-33}$$

and, $\boldsymbol{P}$ is the covariance matrix; $\boldsymbol{Q}_{\mathrm{i}} = E[\boldsymbol{u}_{\mathrm{i}}\boldsymbol{u}_{\mathrm{i}}{}^{\mathrm{T}}]$ is the process noise matrix, which can be approximated by (Deurloo 2011, Brown and Hwang 1997):

$$\boldsymbol{Q}_{i-1} \approx \boldsymbol{G}_{i-1}\boldsymbol{Q}\Delta t\boldsymbol{G}_{i-1}^{\mathrm{T}} \tag{4-34}$$

where, $\boldsymbol{Q}$ is the so called Spectral Density Matrix, which can have the form (Shin 2001, Brown and Hwang 1997):

$$\boldsymbol{Q} = diag\left(\sigma_{a_x}^2 \quad \sigma_{a_y}^2 \quad \sigma_{a_z}^2 \quad \sigma_{\omega_x}^2 \quad \sigma_{\omega_y}^2 \quad \sigma_{\omega_z}^2\right)_{6\times 6} \tag{4-35}$$

where, σ_a and σ_ω are the standard deviations for the accelerometers and gyros noise, which are specified as random walk.

In the Kalman Filter predict process, the 15-dimensional state vector is calculated through equations (4-32). Because of the random walk characteristics of the drift error of the IMUs, the errors of the states grow with the time.

4.4.2 Measurement update

To correct these growing errors continuous update observations are necessary and, usually, GNSS, odometers, known gravity or terrestrial information, as well as images derived information, can be used to make these updates.

According to the equations of (4-10) to (4-12), the measurement update equations can be resumed as:

$$\delta\boldsymbol{x}_{i/i} = \delta\boldsymbol{x}_{i/i-1} + \boldsymbol{K}_i[\delta\boldsymbol{z}_i - \boldsymbol{H}_i\delta\boldsymbol{x}_{i/i-1}] \tag{4-36}$$

$$\boldsymbol{P}_{i/i} = [\boldsymbol{I} - \boldsymbol{K}_i\boldsymbol{H}_i]\boldsymbol{P}_{i/i-1} \tag{4-37}$$

$$\boldsymbol{K}_i = \boldsymbol{P}_{i/i-1}\boldsymbol{H}_i[\boldsymbol{H}_i\boldsymbol{P}_{i/i-1}\boldsymbol{H}_i^{\mathrm{T}} + \boldsymbol{R}_i]^{-1} \tag{4-38}$$

where, $\boldsymbol{K}$ is the argument matrix and $\boldsymbol{R}$ is the covariance matrix of the measurements.

In this thesis, one main update source for the Kalman Filter is the GNSS measurement. There are several implemented strategies for the integration of the IMUs prediction and GNSS measurement update, but the most used are loosely coupled and tightly coupled. The main difference between the two strategies is that loosely coupled is using the processed GNSS solutions, which are positions and velocities, while tightly coupled is directly using the GNSS raw pseudo-range, pseudo-range derivative, and carrier phase observations. These two coupled strategies are usually considered as GNSS aided INS. There is also a deeper coupled strategy, named deeply or ultra-tightly coupled, which is using the INS predictions to help tracking the GNSS weak signals, and can be considered as INS aided GNSS (Yang 2008). Because this last approach belongs to the area of the design of the high sensitivity GNSS, which is not the topic of this thesis, we will not discuss them here. We are focus on GNSS aided INS, and a description of the loosely and tightly coupled approaches is given below.

Loosely coupled Kalman Filter

In the loosely coupled strategy, two separated filters are used: one filter is to obtain the GNSS positions and velocities, and the other one is for the GNSS/IMU integration. Once the GNSS filter outputs the results of position and velocity, the filter for the integration GNSS/IMU starts to work. Fig. 4-3 shows a scheme of the steps of the loosely coupled Kalman Filter.

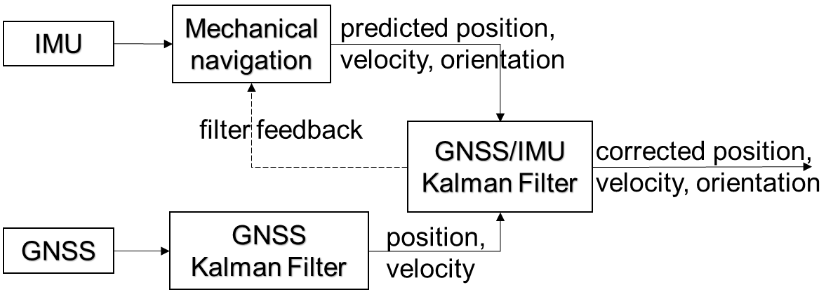

Fig. 4-3 Scheme of the loosely coupled Kalman Fitler.

The measurement observation for Equation (4-36) yields:

$$\delta \boldsymbol{z}_i^1 = \begin{bmatrix} \boldsymbol{r}_{gnss}^n - \boldsymbol{r}_{imu}^n \\ \boldsymbol{v}_{gnss}^n - \boldsymbol{v}_{imu}^n \end{bmatrix}_{6\times1} = \underset{6\times15}{\boldsymbol{H}_1}\,\underset{15\times1}{\delta\boldsymbol{x}_{i/i-1}} + \underset{6\times1}{\boldsymbol{v}_1} \tag{4-39}$$

where, the design matrix is defined as:

$$\boldsymbol{H}_1 = \begin{bmatrix} \boldsymbol{I}_{3\times3} & \boldsymbol{0}_{3\times3} & \boldsymbol{0}_{3\times3} & \boldsymbol{0}_{3\times3} & \boldsymbol{0}_{3\times3} \\ \boldsymbol{0}_{3\times3} & \boldsymbol{I}_{3\times3} & \boldsymbol{0}_{3\times3} & \boldsymbol{0}_{3\times3} & \boldsymbol{0}_{3\times3} \end{bmatrix} \tag{4-40}$$

and, $\boldsymbol{r}_{gnss}^n$ and $\boldsymbol{v}_{gnss}^n$ are, respectively, the position and velocity vectors in the navigation frame calculated from GNSS. $\boldsymbol{r}_{imu}^n$ and $\boldsymbol{v}_{imu}^n$ are the position and velocity predictions for the same instant obtained from the inertial navigation equation; $\boldsymbol{v}_1$ is the zero mean Gaussian noise of the GNSS position and velocity output. Normally the covariance matrix $\boldsymbol{R}_1$ of the observations using Equation (4-38) is defined according to the quality of the GNSS solutions, and the values are set with a fixed matrix. During the airborne tests analyzed in this thesis, the GNSS visibility was good, therefore $\boldsymbol{R}_1$ can be set as a diagonal matrix with an experimental diagonal elements given by:

$$\boldsymbol{R}_1 = diag\left((0.1\,m)^2 \quad (0.1\,m)^2 \quad (0.15\,m)^2 \quad (0.05\,m/s)^2 \quad (0.05\,m/s)^2 \quad (0.05\,m/s)^2 \right) \tag{4-41}$$

In general, the loosely coupled Kalman Filter is suited for the case when there are more than 4 GNSS satellites observed. The filter cannot keep the robustness if there is a long time with lack of GNSS satellites.

Tightly coupled Kalman Filter

Unlike the loosely coupled strategy, in the tightly coupled strategy, the GNSS raw observation of pseudo-range, pseudo-range derivative and carrier phase are directly used, as the update source of the Kalman Filter. Fig. 4-4 is the scheme of the loosely coupled Kalman Fitler.

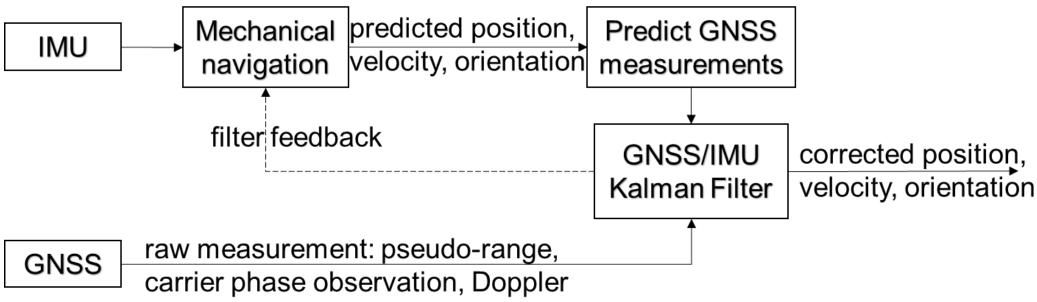

Fig. 4-4 Scheme of the tightly coupled Kalman Fitler.

The measurement observation for Equation (4-36) yields:

$$\delta \mathbf{z}_i^2 = \begin{bmatrix} \boldsymbol{\rho}_i^k - \boldsymbol{\rho}_{i,imu}^k \\ \cdots \\ \dot{\boldsymbol{\rho}}_i^k - \dot{\boldsymbol{\rho}}_{i,imu}^k \\ \cdots \end{bmatrix}_{2n\times 1} \tag{4-42}$$

where, n means the number of observed satellites, $\boldsymbol{\rho}_i^k$ means the real observation from the i^{th} receiver to the k^{th} satellite, $\dot{\boldsymbol{\rho}}_i^k$ means the real derivative of the pseudo-range or carrier phase observation, $\boldsymbol{\rho}_{i,imu}^k$ and $\dot{\boldsymbol{\rho}}_{i,imu}^k$ represents the predicted observations from the IMU prediction process.

According to Equation (2-22), the structure of the observations can be expressed in a detailed way as:

$$\begin{aligned} P_i^k &= a_{x_i}^k \delta x + a_{y_i}^k \delta y + a_{z_i}^k \delta y + cdt_i + e_{\rho,i}^k \\ \Phi_i^k &= a_{x_i}^k \delta x + a_{y_i}^k \delta y + a_{z_i}^k \delta y + cdt_i - I_r^s + T_r^s + \lambda_i N_r^s + + e_{f,i}^k \\ \dot{P}_i^k &= b_{x_i}^k \delta x + b_{y_i}^k \delta y + b_{z_i}^k \delta y + b_{vx_i}^k \delta v_x + b_{vy_i}^k \delta v_y + b_{vz_i}^k \delta v_z + cd\dot{t}_i + e_{d,i}^k \end{aligned} \tag{4-43}$$

and with the difference equation with IMU predictions as:

$$
\begin{aligned}
P_i^k &= \rho_i^k - \rho_{i,imu}^k + cdt^k \\
\Phi_i^k &= \phi_i^k - \phi_{i,imu}^k \\
\dot{P}_i^k &= \dot{\rho}_i^k - \dot{\rho}_{i,imu}^k + cd\dot{t}^k \approx \dot{\rho}_i^k - \dot{\rho}_{i,x}^k
\end{aligned}
\tag{4-44}
$$

where, ρ_i^k means the pseudo-range observation from the i^{th} receiver to the k^{th} satellite, ϕ_i^k means the carrier phase observation, $\dot{\rho}_i^k$ means the derivative of the pseudo-range or carrier phase observation, $\rho_{i,imu}^k$ and $\dot{\rho}_{i,imu}^k$ represents the predicted observations from the IMU prediction process.

If the correction items for clocks, troposphere, ionosphere, ambiguities, etc., are estimated or minimized, the equation (4-43) can be simplified as (Angrisano 2010):

$$
\begin{cases}
l_i^k = a_{x_i}^k \delta x + a_{y_i}^k \delta y + a_{z_i}^k \delta y + e_{l,i}^k \\
\dot{l}_i^k = b_{x_i}^k \delta x + b_{y_i}^k \delta y + b_{z_i}^k \delta y + b_{vx_i}^k \delta v_x + b_{vy_i}^k \delta v_y + b_{vz_i}^k \delta v_z + e_{d,i}^k
\end{cases}
\tag{4-45}
$$

or in a matrix form, with n satellites observations:

$$
\underset{2n\times 1}{\begin{bmatrix} l_i^1 \\ l_i^2 \\ \vdots \\ l_i^n \\ \dot{l}_i^1 \\ \dot{l}_i^2 \\ \vdots \\ \dot{l}_i^n \end{bmatrix}} = \underset{2n\times 6}{\begin{bmatrix} a_{x_i}^1 & a_{y_i}^1 & a_{z_i}^1 & 0 & 0 & 0 \\ a_{x_i}^2 & a_{y_i}^2 & a_{z_i}^2 & 0 & 0 & 0 \\ \vdots & \vdots & \vdots & \vdots & \vdots & \vdots \\ a_{x_i}^n & a_{y_i}^n & a_{z_i}^n & 0 & 0 & 0 \\ b_{x_i}^1 & b_{y_i}^1 & b_{z_i}^1 & b_{v_{x_i}}^1 & b_{v_{y_i}}^1 & b_{v_{z_i}}^1 \\ b_{x_i}^2 & b_{y_i}^2 & b_{z_i}^2 & b_{v_{x_i}}^2 & b_{v_{y_i}}^2 & b_{v_{z_i}}^2 \\ \vdots & \vdots & \vdots & \vdots & \vdots & \vdots \\ b_{x_i}^n & b_{y_i}^n & b_{z_i}^n & b_{v_{x_i}}^n & b_{v_{y_i}}^n & b_{v_{z_i}}^n \end{bmatrix}} \underset{6\times 1}{\begin{bmatrix} \delta x \\ \delta y \\ \delta z \\ \delta v_x \\ \delta v_y \\ \delta v_z \end{bmatrix}} + \underset{2n\times 1}{e_i^k}
\tag{4-46}
$$

In an abbreviate way this equation can be written as:

$$
\underset{2n\times 1}{\boldsymbol{z}_e} = \underset{2n\times 6}{\boldsymbol{H}_e} \underset{6\times 1}{\delta \boldsymbol{x}_e} + \underset{2n\times 1}{\boldsymbol{e}}
\tag{4-47}
$$

where, $a_{x_i}^k = \dfrac{\Delta x_i^k}{\rho_{0,i}^k}$, $a_{y_i}^k = \dfrac{\Delta y_i^k}{\rho_{0,i}^k}$, $a_{z_i}^n = \dfrac{\Delta z_i^k}{\rho_{0,i}^k}$, $\Delta x_i^k = x_i - x^k$, $\Delta y_i^k = y_i - y^k$, $\Delta z_i^k = z_i - z^k$,

$\rho_{0,i}^k = \sqrt{(\Delta x_i^k)^2 + (\Delta y_i^k)^2 + (\Delta z_i^k)^2}$; $b_{x_i}^k = \dfrac{\Delta v_{x_i^k}}{\rho_{0,i}^k} + \dfrac{\Delta x_i^k dv}{(\rho_{0,i}^k)^3}$, $b_{y_i}^k = \dfrac{\Delta v_{y_i^k}}{\rho_{0,i}^k} + \dfrac{\Delta y_i^k dv}{(\rho_{0,i}^k)^3}$, $b_{z_i}^k = \dfrac{\Delta v_{z_i^k}}{\rho_{0,i}^k} + \dfrac{\Delta z_i^k dv}{(\rho_{0,i}^k)^3}$,

$b_{v_{x_i}}^k = \dfrac{\Delta x_i^k}{\rho_{0,i}^k}$, $b_{v_{y_i}}^k = \dfrac{\Delta y_i^k}{\rho_{0,i}^k}$, $b_{v_{z_i}}^n = \dfrac{\Delta z_i^k}{\rho_{0,i}^k}$, $\Delta v_{x_i^k} = v_{x,i} - v^k$, $\Delta v_{y_i^k} = v_{y,i} - v^k$, $\Delta v_{z_i^k} = v_{z,i} - v^k$,

$dv = \Delta x_i^k \Delta v_{x_i^k} + \Delta y_i^k \Delta v_{y_i^k} + \Delta z_i^k \Delta v_{z_i^k}$, and $\boldsymbol{H}_e = \begin{bmatrix} \boldsymbol{A} & \boldsymbol{0}_{n\times 3} \\ \boldsymbol{B}^r & \boldsymbol{B}^v \end{bmatrix}_{2n\times 6}$.

The error update equation using the tightly coupled strategy yields:

$$\underset{2n\times1}{\delta\boldsymbol{z}_e^2} = \underset{2n\times1}{\boldsymbol{z}_e} - \underset{2n\times15}{\boldsymbol{H}_2}\,\underset{15\times1}{\delta\boldsymbol{x}_{i/i-1}} = \underset{2n\times15}{\boldsymbol{H}_2}\,\underset{15\times1}{\delta\boldsymbol{x}_{i/i-1}} + \underset{2n\times1}{\boldsymbol{v}_2} \tag{4-48}$$

where, the design matrix can be written as:

$$\begin{aligned} \underset{2n\times15}{\boldsymbol{H}_2} &= \underset{2n\times6}{\boldsymbol{H}_e}\,\underset{6\times6}{\boldsymbol{H}_n^e}\,\underset{2n\times15}{\boldsymbol{H}_n} \\ \boldsymbol{H}_n &= \begin{bmatrix} \boldsymbol{I}_{15\times15} \\ \boldsymbol{0}_{(2n-15)\times15} \end{bmatrix} \end{aligned} \tag{4-49}$$

and, $\boldsymbol{v}_2$ is the zero mean Gaussian noise of the GNSS raw observation.

At the update observation stage of the tightly coupled Kalman Filter, the error states δz_e are in the Earth-fixed coordinate frame, while the error states δz in our GNSS/INS navigation application are in the local geographic navigation frame, so it is mandatory to build the connection of the two different frames. The position and velocity coordinates defined in the Earth-fixed coordinate frame and in the local geographic navigation frame can be related through (Jekeli 2001a):

$$\delta\boldsymbol{r}^e = \boldsymbol{C}_n^e\boldsymbol{D}\delta\boldsymbol{r}^n \tag{4-50}$$

$$\delta\boldsymbol{v}^e = \boldsymbol{C}_n^e\delta\boldsymbol{v}^n \tag{4-51}$$

where, $\delta\boldsymbol{r}^e = [\delta x\ \delta y\ \delta z]^{\mathrm{T}}$, $\delta\boldsymbol{r}^e = [\delta v_x\ \delta v_y\ \delta v_z]^{\mathrm{T}}$, $\delta\boldsymbol{r}^n = [\delta L\ \delta l\ \delta h]^{\mathrm{T}}$, $\delta\boldsymbol{v}^n = [\delta v_N\ \delta v_E\ \delta v_D]^{\mathrm{T}}$, and

$$\boldsymbol{C}_n^e = \begin{bmatrix} -\sin L\cos l & -\sin l & -\cos L\cos l \\ -\sin L\sin l & \cos l & -\cos L\sin l \\ \cos L & 0 & -\sin L \end{bmatrix}^{-1} \tag{4-52}$$

then,

$$\underset{6\times6}{\boldsymbol{H}_n^e} = \begin{bmatrix} \boldsymbol{C}_n^e\boldsymbol{D} & \\ & \boldsymbol{C}_n^e \end{bmatrix}_{6\times6} \tag{4-53}$$

The measurement observation for Equation (4-36) yields:

$$\delta\boldsymbol{z}_i = \boldsymbol{H}_2^{-1}\delta\boldsymbol{z}_e = \boldsymbol{H}_2^{-1}\boldsymbol{z}_e - \delta\boldsymbol{x}_{i/i-1} \tag{4-54}$$

The covariance matrix $\boldsymbol{R}_2$ of the observation used in Equation (4-38) is defined according to the covariance of the GNSS raw observations, and in this thesis cases it was set as:

$$\boldsymbol{R}_2 = \boldsymbol{H}_2^{-1}\begin{bmatrix} \boldsymbol{R}_l & \\ & \boldsymbol{R}_l \end{bmatrix}_{2n\times2n}\left(\boldsymbol{H}_2^{-1}\right)^{\mathrm{T}} \tag{4-55}$$

where, $\boldsymbol{R}_l = \boldsymbol{I}_{n\times n}\times(0.05\ m)^2$, and $\boldsymbol{R}_i = \boldsymbol{I}_{n\times n}\times(0.01\ m/s)^2$.

In general, Kalman Filter is the core part of our algorithm developed in this thesis, and the critical technical details, such as the matrices setting of sates vectors and measurement vector, the choosing of the proper integration strategy (loosely or tightly) and the covariance matrices setting, which are discussed in the following chapter.

5 Development of a GNSS/MEMS-IMU/Imaging Kalman Filter algorithm

In this chapter, the developments for the implementation of the GNSS/MEMS-IMU/Imaging Kalman Filter will be presented. The algorithm is based on a loosely coupled integration of GNSS, IMU and the relative orientation retrieved from images. Comparing with the tightly coupled strategy, the loosely coupled has a simpler structure and the process is much faster (Godha 2006, Ding 2008).

For the development of this work, a geodetic GNSS receiver, a MEMS-IMUs, and low cost cameras were mounted and tested in aerial platforms. The performance of the low cost GNSS/MEMS-IMU integration can't satisfy the requirements for precise geodetic photogrammetry surveys, because the orientation errors are too large. In order to further improve the performance of GNSS/MEMS-IMU integration, the precise geometric information retrieved from images acquired simultaneously by a low cost camera was used as an additional update information, this allowed a significant improvement in the determination of the exterior orientation parameters. To further improve the performance of the new method, a robust adaptive Kalman Filter was introduced, with the determination of the adaptive factor and the robust factor accomplished by the innovation information and the threshold value of the orientation changes between consecutive images respectively. This is the main innovation introduced in this thesis, and will be presented in detail in this chapter.

The equivalence of the loosely and tightly coupled strategies is proved and validated through a practical airborne test. We then adopted the loosely coupled Kalman Filter for integration of GNSS and IMU as the core method for our airborne application, due to its simple structure and robust characteristics. We start by proving the equivalence of the GNSS loosely and tightly coupled strategies under the condition of good GNSS observation scenario. This is important in our type of applications because, in an airborne environment, the GNSS is always in a good situation, therefore, we could use the loosely coupled as the main strategy to integrate the GNSS and IMU.

5.1 Equivalence of GNSS/INS loosely and tightly coupled Kalman Filter under the condition of good GNSS observation scenario

The loosely and tightly coupled strategies are using the GNSS information in different ways, leading to two different structures: the loosely coupled strategy includes two separate filters: GNSS positioning filter and GNSS/INS integration filter; the tightly coupled strategy uses only one centralized filter. The loosely coupled has the disadvantage that the system may diverge if there is a too long time without enough GNSS satellites, while the tightly coupled shows much better performance during GNSS outages, as it has been shown by many researchers (Mohamed and Schwarz 1999, Babu and Wang 2004, Kreye *et al.* 2004, Bhatti *et al.* 2007, Yang 2008, Angrisano 2010, Khan and Qin 2016). However, which one has a better performance under the condition of enough GNSS satellites observing (theoretically > 4 satellites each epoch) is a question worth to discuss.

Some researchers hold the opinion that the loosely coupled strategy has a simple and smaller structure and the process is faster than the tightly coupled, and this separated Kalman Filter is more robust because one of the systems of the GNSS or the INS can keep working in the case that the other one fails (Godha 2006, Ding 2008), but others argue that the process noise of loosely coupled will be added twice and will affect the performance of the whole system (Angrisano 2010). Different arguments are given, with respect to which coupling strategy, tightly or loosely, allows a better solution, based on practical or simulated tests under the case of enough GNSS observations (Bernal *et al.* 2009, Angrisano 2010, Tawk *et al.* 2014). However, previous studies were based on the fact that the determination of the covariance of the GNSS position and velocity solution for the loosely coupled strategy, and the GNSS raw observation for tightly coupled strategy, are separated, like the equations of (4-41) and (4-55). The separated settings of the update observation are indeed leading to the different performance of the loosely and tightly coupled strategy. However, through building relationship between the covariance of the GNSS position and velocity solution and GNSS raw observations, we can show that the performance of the loosely coupled and tightly coupled strategy are equivalent under the condition of enough GNSS observations.

5.1.1 The equivalence of the loosely and tightly coupled strategies

Under the condition of more than four satellites observed, according to the Least-squares method, the solution of equation (4-48) for GNSS standalone positioning and velocity estimation is:

$$\begin{aligned}
&\underset{15\times1}{\delta\boldsymbol{x}_{i/i-1}} = (\underset{15\times2n}{\boldsymbol{H}_2^{\mathrm{T}}}\,\underset{2n\times2n}{\boldsymbol{W}}\,\underset{2n\times15}{\boldsymbol{H}_2})^{-1}\,\underset{15\times2n}{\boldsymbol{H}_2^{\mathrm{T}}}\,\underset{2n\times2n}{\boldsymbol{W}}\,\underset{2n\times1}{\delta\boldsymbol{z}_e^2} \\
&\underset{15\times15}{\boldsymbol{Q}_{xx}} = (\underset{15\times2n}{\boldsymbol{H}_2^{\mathrm{T}}}\,\underset{2n\times2n}{\boldsymbol{W}}\,\underset{2n\times15}{\boldsymbol{H}_2})^{-1} = \underset{15\times15}{\boldsymbol{N}^{-1}} \\
&\underset{2n\times2n}{\boldsymbol{Q}_{ll}} = \underset{2n\times15}{\boldsymbol{H}_2}\,\underset{15\times15}{\boldsymbol{N}^{-1}}\,\underset{15\times2n}{\boldsymbol{H}_2^{\mathrm{T}}} = \underset{2n\times15}{\boldsymbol{H}_2}\,\underset{15\times15}{\boldsymbol{Q}_{xx}}\,\underset{15\times2n}{\boldsymbol{H}_2^{\mathrm{T}}}
\end{aligned} \tag{5-1}$$

where, $\boldsymbol{W}$ represents the weight matrix of the GNSS observations, and can be given as:

$$\boldsymbol{W} = diag(\sigma_1^{-2}, \sigma_2^{-2}, \ldots, \sigma_m^{-2}) \tag{5-2}$$

where, σ_i is the a-priori standard deviation of the i^{th} measurement error.

and, $\boldsymbol{Q}_{xx}$ and $\boldsymbol{Q}_{ll}$ represent the covariance matrix of the unknown parameters vector and the correction of the observation vectors. During the loosely and tightly coupled strategies, the corresponding update covariance matrices can be notated as $\boldsymbol{R}_1$ and $\boldsymbol{R}_2$ and, according to the equations (4-39) and (4-48), the relationship with $\boldsymbol{Q}_{xx}$ and $\boldsymbol{Q}_{ll}$ can be deduced as:

$$\begin{aligned}
&\underset{15\times15}{\boldsymbol{Q}_{xx}} = \underset{15\times6}{\boldsymbol{H}_1^{\mathrm{T}}}\,\underset{6\times6}{\boldsymbol{R}_1}\,\underset{6\times15}{\boldsymbol{H}_1} \\
&\underset{2n\times2n}{\boldsymbol{Q}_{ll}} = \underset{2n\times2n}{\boldsymbol{R}_2}
\end{aligned} \tag{5-3}$$

If taking the equation (5-3) into (5-1), then the relationship between $\boldsymbol{R}_1$ and $\boldsymbol{R}_2$ can be deduced as:

$$\underset{2n\times2n}{\boldsymbol{R}_2} = \underset{2n\times15}{\boldsymbol{H}_2}\,\underset{15\times6}{\boldsymbol{H}_1^{\mathrm{T}}}\,\underset{6\times6}{\boldsymbol{R}_1}\,\underset{6\times15}{\boldsymbol{H}_1}\,\underset{15\times2n}{\boldsymbol{H}_2^{\mathrm{T}}} \tag{5-4}$$

Some studies show that the performance of the two coupling strategies are different (Bernal *et al.* 2009, Angrisano 2010, Tawk *et al.* 2014, Niu *et al.* 2015), which is mainly because the architectures of the two systems they used are separated, and the respective covariance matrices $\boldsymbol{R}_1$ and $\boldsymbol{R}_2$ are chosen independently, so their relationship were not build as in Equation (5-4).

Loosely and tightly coupled strategies are equivalent under the condition that enough GNSS satellites are observed. Initially, because two strategies have the same performance at both prediction process and update process of the Kalman Filter. From Section 4.4 we can see that both coupling strategies in this thesis are using the same prediction process, and in this section we show the equivalence proof at the update process of Kalman Filter.

At the update process of the Kalman Filter, the loosely coupled strategy can be described by the following equations:

$$\underset{15\times6}{\boldsymbol{K}_i^1} = \underset{15\times15}{\boldsymbol{P}_{i/i-1}}\,\underset{15\times6}{\boldsymbol{H}_1^{\mathrm{T}}}[\underset{6\times15}{\boldsymbol{H}_1}\,\underset{15\times15}{\boldsymbol{P}_{i/i-1}}\,\underset{15\times6}{\boldsymbol{H}_1^{\mathrm{T}}} + \underset{6\times6}{\boldsymbol{R}_1}]^{-1} \tag{5-5}$$

$$\underset{15\times1}{\delta\boldsymbol{x}_{i/i}^{1}} = \underset{15\times1}{\delta\boldsymbol{x}_{i/i-1}} + \underset{15\times6}{\boldsymbol{K}_i^{1}}[\underset{6\times1}{\delta\boldsymbol{z}_i^{1}} - \underset{6\times15}{\boldsymbol{H}_1}\underset{15\times1}{\delta\boldsymbol{x}_{i/i-1}}] \tag{5-6}$$

$$\underset{15\times15}{\boldsymbol{P}_{i/i}^{1}} = [\underset{15\times15}{\boldsymbol{I}} - \underset{15\times6}{\boldsymbol{K}_i^{1}}\underset{6\times15}{\boldsymbol{H}_1}]\underset{15\times15}{\boldsymbol{P}_{i/i-1}} \tag{5-7}$$

and the tightly coupled strategy at the update process uses these equations:

$$\underset{15\times2n}{\boldsymbol{K}_i^{2}} = \underset{15\times15}{\boldsymbol{P}_{i/i-1}}\underset{15\times2n}{\boldsymbol{H}_2^{\mathrm{T}}}[\underset{2n\times15}{\boldsymbol{H}_2}\underset{15\times15}{\boldsymbol{P}_{i/i-1}}\underset{15\times2n}{\boldsymbol{H}_2^{\mathrm{T}}} + \underset{2n\times2n}{\boldsymbol{R}_2}]^{-1} \tag{5-8}$$

$$\underset{15\times1}{\delta\boldsymbol{x}_{i/i}^{2}} = \underset{15\times1}{\delta\boldsymbol{x}_{i/i-1}} + \underset{15\times2n}{\boldsymbol{K}_i^{2}}[\underset{2n\times1}{\delta\boldsymbol{z}_e^{2}} - \underset{2n\times15}{\boldsymbol{H}_2}\underset{15\times1}{\delta\boldsymbol{x}_{i/i-1}}] \tag{5-9}$$

$$\underset{15\times15}{\boldsymbol{P}_{i/i}^{2}} = [\underset{15\times15}{\boldsymbol{I}} - \underset{15\times2n}{\boldsymbol{K}_i^{2}}\underset{2n\times15}{\boldsymbol{H}_2}]\underset{15\times15}{\boldsymbol{P}_{i/i-1}} \tag{5-10}$$

Then, the equivalence proof is based on the proving of the following equations:

$$\underset{15\times1}{\delta\boldsymbol{x}_{i/i}^{1}} = \underset{15\times1}{\delta\boldsymbol{x}_{i/i}^{2}} \tag{5-11}$$

$$\underset{15\times15}{\boldsymbol{P}_{i/i}^{1}} = \underset{15\times15}{\boldsymbol{P}_{i/i}^{2}} \tag{5-12}$$

hold.

According to the equations of (5-6) and (5-9), Equation (5-11) and (5-12) can be written as:

$$\underset{15\times1}{\cancel{\delta\boldsymbol{x}_{i/i-1}}} + \underset{15\times6}{\boldsymbol{K}_i^{1}}\underset{6\times1}{\delta\boldsymbol{z}_i^{1}} - \underset{15\times6}{\boldsymbol{K}_i^{1}}\underset{6\times15}{\boldsymbol{H}_1}\underset{15\times1}{\delta\boldsymbol{x}_{i/i-1}} = \underset{15\times1}{\cancel{\delta\boldsymbol{x}_{i/i-1}}} + \underset{15\times2n}{\boldsymbol{K}_i^{2}}\underset{2n\times1}{\delta\boldsymbol{z}_i^{2}} - \underset{15\times2n}{\boldsymbol{K}_i^{2}}\underset{2n\times15}{\boldsymbol{H}_2}\underset{15\times1}{\delta\boldsymbol{x}_{i/i-1}} \tag{5-13}$$

$$\underset{15\times15}{\cancel{\boldsymbol{I}}}\underset{15\times15}{\cancel{\boldsymbol{P}_{i/i-1}}} - \underset{15\times6}{\boldsymbol{K}_i^{1}}\underset{6\times15}{\boldsymbol{H}_1}\underset{15\times15}{\boldsymbol{P}_{i/i-1}} = \underset{15\times15}{\cancel{\boldsymbol{I}}}\underset{15\times15}{\cancel{\boldsymbol{P}_{i/i-1}}} - \underset{15\times2n}{\boldsymbol{K}_i^{2}}\underset{2n\times15}{\boldsymbol{H}_2}\underset{15\times15}{\boldsymbol{P}_{i/i-1}} \tag{5-14}$$

If we remove the equal items from the two sides of the equations, the proof of Equation (5-13) and (5-14) become:

$$\underset{15\times6}{\boldsymbol{K}_i^{1}}\underset{6\times15}{\boldsymbol{H}_1} = \underset{15\times2n}{\boldsymbol{K}_i^{2}}\underset{2n\times15}{\boldsymbol{H}_2} \tag{5-15}$$

$$\underset{15\times6}{\boldsymbol{K}_i^{1}}\underset{6\times1}{\delta\boldsymbol{z}_i^{1}} = \underset{15\times2n}{\boldsymbol{K}_i^{2}}\underset{2n\times1}{\delta\boldsymbol{z}_i^{2}} \tag{5-16}$$

From the equations (5-5) and (5-8), the following equations can be deduced:

$$\underset{15\times6}{\boldsymbol{K}_i^{1}}[\underset{6\times15}{\boldsymbol{H}_1}\underset{15\times15}{\boldsymbol{P}_{i/i-1}}\underset{15\times6}{\boldsymbol{H}_1^{\mathrm{T}}} + \underset{6\times6}{\boldsymbol{R}_1}] = \underset{15\times15}{\boldsymbol{P}_{i/i-1}}\underset{15\times6}{\boldsymbol{H}_1^{\mathrm{T}}} \tag{5-17}$$

$$\underset{15\times2n}{\boldsymbol{K}_i^{2}}[\underset{2n\times15}{\boldsymbol{H}_2}\underset{15\times15}{\boldsymbol{P}_{i/i-1}}\underset{15\times2n}{\boldsymbol{H}_2^{\mathrm{T}}} + \underset{2n\times2n}{\boldsymbol{R}_2}] = \underset{15\times15}{\boldsymbol{P}_{i/i-1}}\underset{15\times2n}{\boldsymbol{H}_2^{\mathrm{T}}} \tag{5-18}$$

using the equation (5-18), we can obtain:

$$\underset{15\times15}{\boldsymbol{P}_{i/i-1}} = \underset{15\times2n}{\boldsymbol{K}_i^2}[\underset{2n\times15}{\boldsymbol{H}_2}\,\underset{15\times15}{\boldsymbol{P}_{i/i-1}}\,\underset{15\times2n}{\boldsymbol{H}_2^{\mathrm{T}}} + \underset{2n\times2n}{\boldsymbol{R}_2}][\underset{2n\times15}{\boldsymbol{H}_2^{\mathrm{T}}}]^{-1} \tag{5-19}$$

if substituting it into Equation (5-17), it becomes:

$$\begin{aligned}
&\underset{15\times6}{\boldsymbol{K}_i^1}[\underset{6\times15}{\boldsymbol{H}_1}\,\underset{15\times15}{\boldsymbol{P}_{i/i-1}}\,\underset{15\times6}{\boldsymbol{H}_1^{\mathrm{T}}} + \underset{6\times6}{\boldsymbol{R}_1}] = \underset{15\times2n}{\boldsymbol{K}_i^2}[\underset{2n\times15}{\boldsymbol{H}_2}\,\underset{15\times15}{\boldsymbol{P}_{i/i-1}}\,\underset{15\times2n}{\boldsymbol{H}_2^{\mathrm{T}}} + \underset{2n\times2n}{\boldsymbol{R}_2}][\underset{2n\times15}{\boldsymbol{H}_2^{\mathrm{T}}}]^{-1}\underset{15\times6}{\boldsymbol{H}_1^{\mathrm{T}}}\\
&\underset{15\times6}{\boldsymbol{K}_i^1}\,\underset{6\times15}{\boldsymbol{H}_1}\,\underset{15\times15}{\cancel{\boldsymbol{P}_{i/i-1}}}\,\underset{15\times6}{\cancel{\boldsymbol{H}_1^{\mathrm{T}}}} + \underset{15\times6}{\boldsymbol{K}_i^1}\,\underset{6\times6}{\boldsymbol{R}_1} = \underset{15\times2n}{\boldsymbol{K}_i^2}\,\underset{2n\times15}{\boldsymbol{H}_2}\,\underset{15\times15}{\cancel{\boldsymbol{P}_{i/i-1}}}\,\underset{15\times6}{\cancel{\boldsymbol{H}_1^{\mathrm{T}}}} + \underset{15\times2n}{\boldsymbol{K}_i^2}\,\underset{2n\times2n}{\boldsymbol{R}_2}[\underset{2n\times15}{\boldsymbol{H}_2^{\mathrm{T}}}]^{-1}\underset{15\times6}{\boldsymbol{H}_1^{\mathrm{T}}}
\end{aligned} \tag{5-20}$$

if we assume that Equation (5-15) holds, then:

$$\underset{15\times2n}{\boldsymbol{K}_i^2} = \underset{15\times6}{\boldsymbol{K}_i^1}\,\underset{6\times15}{\boldsymbol{H}_1}[\underset{15\times2n}{\boldsymbol{H}_2}]^{-1} \tag{5-21}$$

if substituting this into Equation (5-20), and removing the equal items of two sides, Equation (5-20) can be rewritten as:

$$\underset{6\times6}{\boldsymbol{R}_1} = \underset{6\times15}{\boldsymbol{H}_1}[\underset{15\times2n}{\boldsymbol{H}_2}]^{-1}\,\underset{2n\times2n}{\boldsymbol{R}_2}[\underset{2n\times15}{\boldsymbol{H}_2^{\mathrm{T}}}]^{-1}\underset{15\times6}{\boldsymbol{H}_1^{\mathrm{T}}} \tag{5-22}$$

If we use Equation (5-4) into (5-22), it can be rewritten as:

$$\begin{aligned}
&\underset{6\times6}{\boldsymbol{R}_1} = \underset{6\times15}{\boldsymbol{H}_1}[\underset{15\times2n}{\cancel{\boldsymbol{H}_2}}]^{-1}\,\underset{2n\times15}{\cancel{\boldsymbol{H}_2}}\,\underset{15\times6}{\boldsymbol{H}_1^{\mathrm{T}}}\,\underset{6\times6}{\boldsymbol{R}_1}\,\underset{6\times15}{\boldsymbol{H}_1}\,\underset{15\times2n}{\cancel{\boldsymbol{H}_2^{\mathrm{T}}}}[\underset{2n\times15}{\cancel{\boldsymbol{H}_2^{\mathrm{T}}}}]^{-1}\underset{15\times6}{\boldsymbol{H}_1^{\mathrm{T}}}\\
&\underset{6\times6}{\boldsymbol{R}_1} = \underset{6\times15}{\boldsymbol{H}_1}\,\underset{15\times6}{\boldsymbol{H}_1^{\mathrm{T}}}\,\underset{6\times6}{\boldsymbol{R}_1}\,\underset{6\times15}{\boldsymbol{H}_1}\,\underset{15\times6}{\boldsymbol{H}_1^{\mathrm{T}}}
\end{aligned} \tag{5-23}$$

From Equation (4-40) we can obtain:

$$\underset{6\times15}{\boldsymbol{H}_1}\,\underset{15\times6}{\boldsymbol{H}_1^{\mathrm{T}}} = \underset{6\times6}{\boldsymbol{I}} \tag{5-24}$$

then, Equation (5-23) becomes $\boldsymbol{R}_1 = \boldsymbol{R}_1$, and therefore, Equation (5-22) holds. So the assumption of Equation (5-15) is correct, and Equation (5-12) is correct.

Once we show that Equation (5-12) holds, then we can write:

$$\underset{15\times6}{\boldsymbol{K}_i^1} = \underset{15\times2n}{\boldsymbol{K}_i^2}\,\underset{2n\times15}{\boldsymbol{H}_2}[\underset{15\times6}{\boldsymbol{H}_1}]^{-1} \tag{5-25}$$

Then, to prove the equation (5-16) is true, we need to prove that the following equations are true:

$$\begin{aligned}
&\underset{15\times2n}{\cancel{\boldsymbol{K}_i^2}}\,\underset{2n\times15}{\boldsymbol{H}_2}[\underset{15\times6}{\boldsymbol{H}_1}]^{-1}\underset{6\times1}{\delta\boldsymbol{z}_i^1} = \underset{15\times2n}{\cancel{\boldsymbol{K}_i^2}}\,\underset{2n\times1}{\delta\boldsymbol{z}_i^2}\\
&\underset{2n\times1}{\delta\boldsymbol{z}_i^2} = \underset{2n\times15}{\boldsymbol{H}_2}[\underset{15\times6}{\boldsymbol{H}_1}]^{-1}\underset{6\times1}{\delta\boldsymbol{z}_i^1}
\end{aligned} \tag{5-26}$$

Using Equation (4-39), we can write:

$$\underset{15\times 6}{[\boldsymbol{H}_1]^{-1}}\left(\underset{6\times 1}{\delta \boldsymbol{z}_i^1} - \underset{6\times 1}{\boldsymbol{v}_1}\right) = \underset{15\times 1}{\delta \boldsymbol{x}_{i/i-1}} \tag{5-27}$$

Then Equation (5-26) can be written as:

$$\underset{2n\times 1}{\delta \boldsymbol{z}_e^2} = \underset{2n\times 15}{\boldsymbol{H}_2}\,\underset{15\times 1}{\delta \boldsymbol{x}_{i/i-1}} + \underset{2n\times 1}{\boldsymbol{v}} \tag{5-28}$$

which is identical to Equation (4-48).

Therefore we show that the assumption of Equation (5-16) is also correct.

5.1.2 Validation test

In order to show the equivalence of the two strategies, loosely and tightly coupled approaches, a real dataset together with simulated observations were used from a test done in Espinho in August 2013, which will be described in Chapter 6. The validation steps are shown in Fig. 5-1.

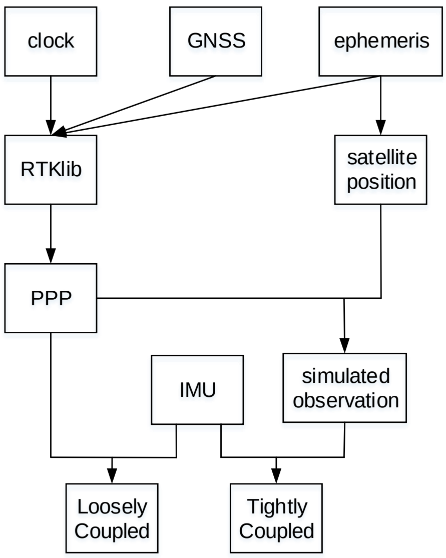

Fig. 5-1 The flow chart of Loosely/Tightly Coupled Strategies.

During the test, the GPS solution for the loosely coupled strategy was obtained with “RTKlib” software using the PPP approach, and the precise GPS ephemeris and clocks were used. The covariance matrix of the loosely coupled, $\boldsymbol{R}_1$, was computed using Equation (5-22), where the covariance matrix of tightly coupled, $\boldsymbol{R}_2$, was used. Then the connection of the two coupled strategies was built. For the tightly coupled strategy, the raw Doppler observation given in observation file was used, but due to the additional work needed for the integer ambiguities estimation, the phase observations were simulated using the equation:

$$\Phi_{i,simu}^k = \sqrt{\left(x^k - x_{i,ppp}\right)^2 + \left(y^k - y_{i,ppp}\right)^2 + \left(z^k - z_{i,ppp}\right)^2} \tag{5-29}$$

where, (x^k, y^k, z^k) represents the k^{th} satellite positions at the epoch of GNSS signal transmitting, which is calculated with the precise ephemeris through the Equation (2-18) to (2-24), $(x_{i,ppp}, y_{i,ppp}, z_{i,ppp})$ is the receiver position obtained via the RTKlib software using the PPP approach. In this thesis we are not aiming to develop a GNSS processing software, just for this validation we simulated the phase observations.

The parameters of the covariance matrix $\boldsymbol{R}_2$ for the measurement of the tightly coupled strategy were set as: phase observation is 0.002 m, Doppler is 1 cm/s.

The solution of position, velocity, and orientation obtained from each of two strategies were compared. Because the position and velocity solution of the two strategies are identical, so here only the orientation solution comparison was done.

Fig. 5-2 shows the results of the Differences of the orientation results obtained with the loosely and tightly coupled strategies. From Fig. 5-2 we can see that, at the beginning of the test, the orientation difference are a little large, particular the difference of the heading angles that reaches 0.014°, this is mainly due to the alignment. Table 5-1 shows the statistics of the difference between the orientation solution of loosely and tightly coupled strategies, where the disagreement at the alignment stage was removed from the statistics analysis. From Table 5-1 we can see that the orientation difference between the two strategies is small, at the level of below 0.5×10^{-3} ° of the standard deviation.

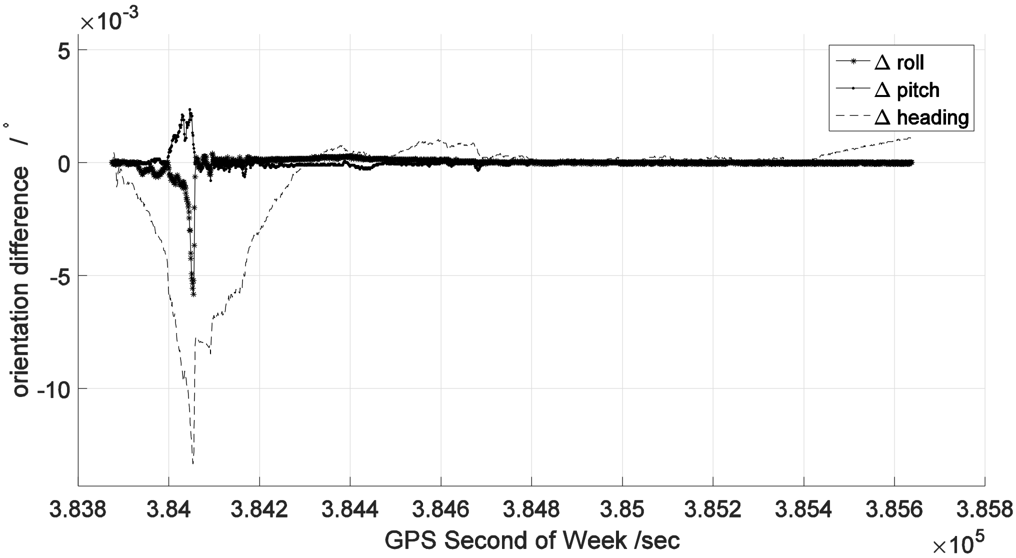

Fig. 5-2 Differences of the orientation results obtained with the loosely and tightly coupled strategies.

Table 5-1 Statistics of the difference between the orientation solution obtained with the loosely and tightly coupled strategies.

	Δroll / 10^{-3} °	Δpitch / 10^{-3} °	Δheading / 10^{-3} °
max	0.286	0.114	1
Min	-0.057	-0.343	-0.114
mean	0.048	-0.021	0.281
std	0.084	0.071	0.256

Therefore, the results from this test show that the loosely and tightly coupled strategies deliver equivalent results. The tightly coupled strategy can have advantages under the situation of poor GNSS observation, however, during aerial observation, the GNSS signals are rarely blocked, as it happens in the terrestrial applications.

Due to this equivalence, we decided to use the loosely coupled approach for the integration of GPS and IMU data, as it allows us to keep a robust aiding of position and orientation for the aerial Photogrammetry.

5.2 GNSS/MEMS-IMU/Imaging Coupled System

The algorithm of the integration of GNSS/MEMES-IMU/Imaging is now presented in detail in this section. The setup of the Kalman Filter for the integration of GNSS/IMU has been well developed in the last decades, and the distinct work here is the inclusion of the geometry information retrieved from the images as additional measurements. In the application of GNSS/IMU aided photogrammetric observations, besides the GNSS measurements, images obtained from the cameras are also available, The GNSS updates, the camera exposure events and the IMU samplings are synchronized by GPS time. The IMU samplings and camera exposure events are tagged by GPS updates (see Fig. 5-3). Simultaneous IMU samplings are interpolated at the epochs of the GPS updates and the camera exposures.

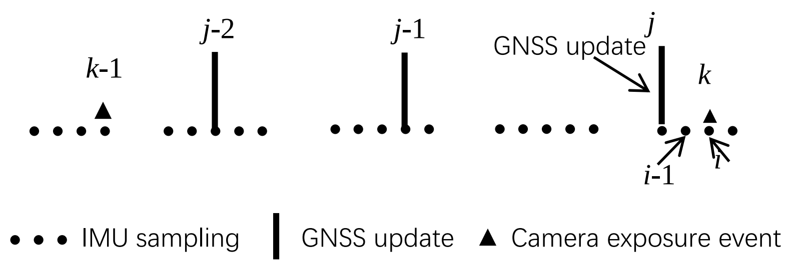

Fig. 5-3 IMU samplings (with index “i” and symbol “•”), GNSS update (with index “j” and symbol “|”) and camera exposure events (with index “k” and symbol “▲”).

The accuracy of the estimation of the exterior orientation parameters is assessed here to check the potential of using it as an additional update measurement to improve the integration of GNSS/MEMS-IMU.

5.2.1 Relative geometric information retrieved from images

As described in Chapter 3, the estimation of the exterior position and orientation parameters is highly depended on the quality and the quantity of the ground tie points. In our processing, besides the ground control points, the tie points automatically detected by the by the "Agisoft Photoscan" software using the algorithm of SIFT/SFM are also applied to estimate the exterior orientation parameters of the images.

Fig. 5-4 shows an overview of the tie points automatically derived by the "Agisoft Photoscan" software in different images overlap. The blue solid points mean strong matching, and the white hollow points indicate a weak matching. From this figure we can see that, many tie points could be automatically obtained precisely by the SIFT/SFM algorithm, and the tie points number in the images with 80% overlap rate are much more than those obtained with 60% overlap rate. Furthermore, and the distribution is with a higher overlap rate. Using these tie points, the exterior orientation parameters can be obtained, during this thesis, it was completed by the software of the software of "Agisoft Photoscan" or the aerial program developed by ourselves.

Fig. 5-5 and Fig. 5-6 show the comparison of the orientation solutions obtained from the SIFT/SFM approach and from the integration GNSS/iMar or GNSS/Litton in two airborne tests in September of 2011 and in August of 2013. iMar and Litton are the high grade IMUs, which belong to the level of navigation and tactical respectively. The GNSS/IMU integration software previously developed at OAUP, was used as reference to assess the quality of the orientation information obtained from the images, these software has been shown that an orientation accuracy can be better than 0.05° (Tomé 2002, Deurloo 2011).

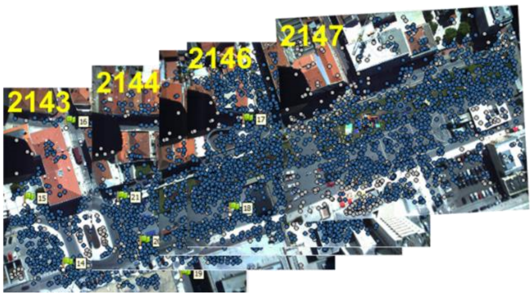

(a) 60% image overlap rate

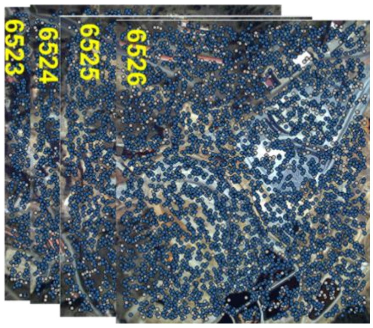

(b) 80% image overlap rate

Fig. 5-4 Tie points overview of the images with different image overlap rate.

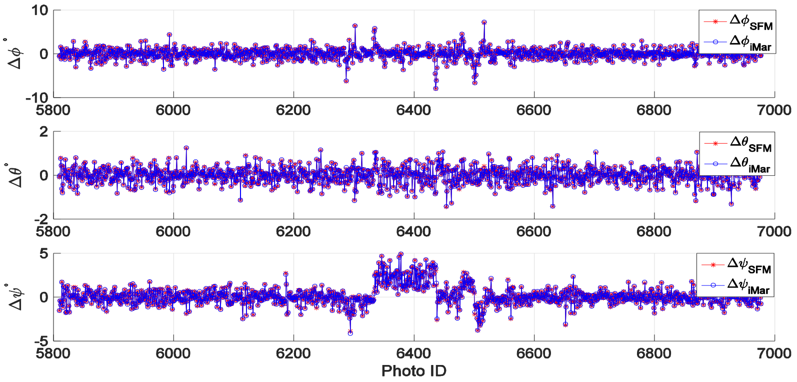

Fig. 5-5 Comparison of the orientation solutions obtained from the SIFT/SFM approach and the GNSS/iMar

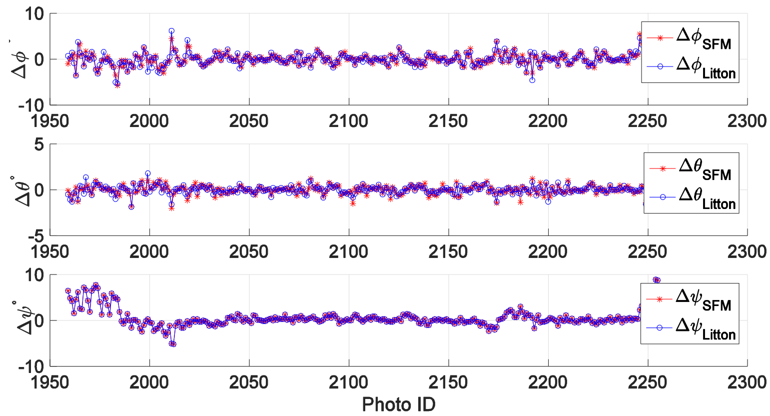

Fig. 5-6 Comparison of the orientation solutions obtained from the SIFT/SFM approach and the GNSS/Litton.

Table 5-2 Statistic of the comparison of the delta orientation solutions from SIFT/SFM and GNSS/iMar (unit: °)

	$\Delta\Delta\phi$	$\Delta\Delta\theta$	$\Delta\Delta\psi$
min	-0.104	-0.095	-0.303
max	0.105	0.091	0.246
std	**0.026**	**0.019**	**0.046**

Table 5-3 Statistic of the comparison of the delta orientation solutions from SIFT/SFM and GNSS/Litton (unit: °)

	$\Delta\Delta\phi$	$\Delta\Delta\theta$	$\Delta\Delta\psi$
min	-0.172	-0.221	-0.303
max	0.103	0.123	0.246
std	**0.049**	**0.045**	**0.053**

Table 5-2 and Table 5-3 give the statistics of the differences between the orientation solutions obtained from the SIFT/SFM and from the integration of GNSS/iMar or GNSS/Litton. $\Delta\psi = \psi_k - \psi_{k-1}$, means the difference retrieved from consecutive images for roll, pitch, and yaw.

From Fig. 5-5, Fig. 5-6, Table 5-2 and Table 5-3, we can see that the relative orientation derived from the image sequences has a very high matching with the GNSS/iMar and GNSS/Litton, which means that the obtained accuracy of the relative orientation is close to the one achieved with the integration of GNSS and high grade IMUs (better than 0.05°). We decided then to use this relative orientation information as an additional update information in our filter.

If there are GCPs available, the precise exterior orientation parameters can be obtained via the process of aerial triangulation, then the orientation obtained by the software of “Agisoft Photoscan” with and without GCPs can be compared here. The differences obtained for the two procedures are plotted in Fig. 5-7. From Fig. 5-7 we can see that there exists an offset and a drift between the two results, which is mainly caused by the boresight between the camera and the IMU which can’t be compensated without GCPs.

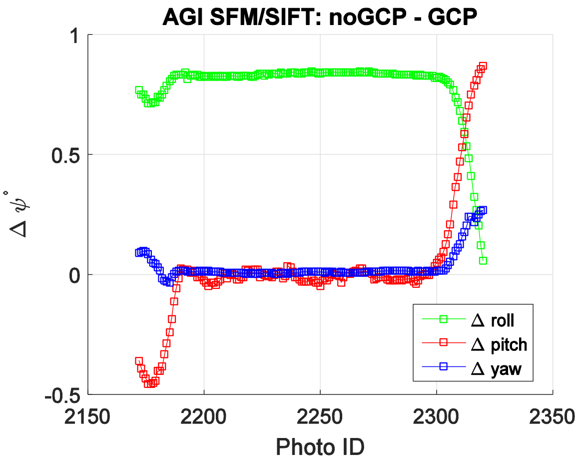

Fig. 5-7 Difference between the orientation solutions with and without GCPs, calculated using the AGIsoft SIFM/SFM software

Using the accuracy relative orientation information that can be retrieved from overlapping images, we can avoid this problem. This has a high potential as an update observation to improve the overall result for the orientation for the Kalman Filter in the GNSS/IMU integration.

Due to this factor, in our algorithm we have used the relative orientation as the update information rather than the absolute orientation.

5.2.2 Applying the GNSS/IMU/Imaging Kalman Filter

The prediction process for the GNSS/IMU/Image Kalman Filter is as described in previous section. The main innovation introduced is related with measurements update. The details of the configurations at the update measurement epoch of the GNSS/IMU/Imaging Kalman Filter are given as following paragraphs.

If there are GNSS observations available, the j^{th} GNSS observation can be written as:

$$\boldsymbol{z}_j^{gnss} = \begin{bmatrix} \boldsymbol{r}_j^{gnss} & \mathbf{v}_j^{gnss} \end{bmatrix}^{\mathrm{T}} \tag{5-30}$$

where, $\boldsymbol{r}_j^{gnss}$ and $\boldsymbol{v}_j^{gnss}$ are the GNSS derived position and velocity.

If there are camera exposure events available, the corresponding k^{th} camera measurement can be written as:

$$\boldsymbol{z}_k^{img} = \boldsymbol{\psi}_k^{img} = \boldsymbol{\psi}_{k-1}^{img} + \Delta\boldsymbol{\psi}_k^{img} \tag{5-31}$$

where, $\boldsymbol{\psi}_{k-1}^{img}$ is the $k\text{-}1^{th}$ orientation angle vector provided by the integration of GNSS/IMU/Imaging; $\Delta\boldsymbol{\psi}_k^{img}$ is the orientation change retrieved from consecutive images at the current epoch, which can be calculated using the SIFT/SFM algorithm referred in Section 3.4.2, which is calculated using the “AGIsoft Photoscan” software.

If the GNSS and the image observations happens at the same time, the update measurements vectors becomes:

$$\boldsymbol{z}_k^{both} = \begin{bmatrix} \boldsymbol{z}_j^{gnss} \\ \boldsymbol{z}_k^{img} \end{bmatrix} \tag{5-32}$$

and, the update observation of the state errors at epoch t_i can then be written as:

$$\delta\boldsymbol{z}_i = \begin{cases} \delta\boldsymbol{z}_j^{gnss} = \boldsymbol{z}_j^{gnss} - \boldsymbol{H}_{gnss}\boldsymbol{x}_{i/i-1} = \boldsymbol{H}_{gnss}\delta\boldsymbol{x}_{i/i-1} + \boldsymbol{l}_j^{gnss},\ if\ t_i = t_j \\ \delta\boldsymbol{z}_k^{img} = \boldsymbol{z}_k^{img} - \boldsymbol{H}_{img}\boldsymbol{x}_{i/i-1} = \boldsymbol{H}_{img}\delta\boldsymbol{x}_{i/i-1} + \boldsymbol{l}_k^{img},\ if\ t_i = t_k \\ \delta\boldsymbol{z}_k^{both} = \boldsymbol{z}_k^{both} - \boldsymbol{H}_{both}\boldsymbol{x}_{i/i-1} = \boldsymbol{H}_{both}\delta\boldsymbol{x}_{i/i-1} + \boldsymbol{l}_k^{both},\ if\ t_i = t_j = t_k \end{cases} \tag{5-33}$$

where, $\boldsymbol{l}$ is a zero mean Gaussian noise of the update observations, which can be used as the innovation sequence in the robust adaptive Kalman Filter, and

$$\boldsymbol{H}_{gnss} = \begin{bmatrix} \boldsymbol{I}_{3\times3} & \boldsymbol{0}_{3\times3} & \boldsymbol{0}_{3\times3} & \boldsymbol{0}_{3\times3} & \boldsymbol{0}_{3\times3} \\ \boldsymbol{0}_{3\times3} & \boldsymbol{I}_{3\times3} & \boldsymbol{0}_{3\times3} & \boldsymbol{0}_{3\times3} & \boldsymbol{0}_{3\times3} \end{bmatrix} \tag{5-34}$$

$$\boldsymbol{H}_{img} = \begin{bmatrix} \boldsymbol{0}_{3\times3} & \boldsymbol{0}_{3\times3} & \boldsymbol{I}_{3\times3} & \boldsymbol{0}_{3\times3} & \boldsymbol{0}_{3\times3} \end{bmatrix} \tag{5-35}$$

$$\boldsymbol{H}_{both} = \begin{bmatrix} \boldsymbol{H}_{gnss} \\ \boldsymbol{H}_{img} \end{bmatrix} \tag{5-36}$$

The update observation retrieved from the GNSS is the position and velocity, which is a 6 state vector. The design matrix $\boldsymbol{H}$ is a 6×15 unit matrix. For the relative orientation information, the dimension of the design matrix is 9×15 if there are both GNSS and camera updates, and 3×15 if there is only camera update available (this situation for the aerial application is very rare). The covariance matrix of the image updating is depending on the observation conditions namely, the overlap rate of the images, as well as the quality of the camera. Therefore the diagonal elements of the covariance matrix must be adjusted accordingly.

When the GNSS update or the camera exposure event happens, the update process can be done using the following equations:

$$\boldsymbol{K}_{flag} = \boldsymbol{P}_{i/i-1}\boldsymbol{H}_{flag}^{\mathrm{T}}[\boldsymbol{H}_{flag}\boldsymbol{P}_{i/i-1}\boldsymbol{H}_{flag}^{\mathrm{T}} + \boldsymbol{R}_{flag}]^{-1} \tag{5-37}$$

$$\delta\boldsymbol{x}_{i/i} = \delta\boldsymbol{x}_{i/i-1} + \boldsymbol{K}_{flag}[\delta\boldsymbol{z}_{flag} - \boldsymbol{H}_{flag}\delta\boldsymbol{x}_{i/i-1}] \tag{5-38}$$

$$\boldsymbol{P}_{i/i} = [\boldsymbol{I} - \boldsymbol{K}_{flag}\boldsymbol{H}_{flag}]\boldsymbol{P}_{i/i-1} \tag{5-39}$$

where, "*flag*" equals "*gnss*", "*img*", or "*both*", depending on the current observation situation.

For the covariance matrix of the update observation, $\boldsymbol{R}_{gnss}$, is defined according to Equation (4-41). For the changes in orientation retrieved from the images, the covariance matrix $\boldsymbol{R}_{img}$, is depending on the observation conditions namely, the overlap rate of the images and the quality of the camera.

5.3 Robust adaptive Kalman Filter

The performance of the integration of GNSS/low-cost-IMU/Imaging can be especially disturbed if the platform is subject to unexpected movements, such as quick turning and titling since these movements lead to distortion errors of the images.

Robust adaptive Kalman Filter has an impressive performance in reducing the influence of unexpected errors and has been used before in the GNSS/IMU integration with good results (Rutan 1991, Moghaddamjoo and Kirlin 1993, Mohamed and Schwarz 1999) showed that the adaptive Kalman Filter led to a 20% improvement in orientation estimation, and the research of Werries and Dolan 2016 demonstrated that the accuracy of the kinematic positioning could be improved by 10% to 50% using a modified adaptive Kalman Filter.

Robust adaptive Kalman Filter has been successfully applied in positioning and navigation since it can optimize the system output by tuning the covariance parameters of the process noise $\boldsymbol{Q}$ and the observation errors $\boldsymbol{R}$ (Yang and Gao 2006, Hajiyev and Soken 2013).

Robust adaptive Kalman Filter has two factors: one adaptive factor is used to tune the weight of the states of the predictions; and the other robust factor is used to balance the contributions of the update measurement. Other researches indicate that the Kalman Filter introducing robust factors estimated by update measurement, under particular conditions, are superior to those obtained by adaptive factors based on the experience (Yang and Gao 2006).

According to previous studies, results from the adaptive Kalman Filter can be smoother than from the classical Kalman Filter if the adaptive factor and robust factor are estimated properly (Gao *et al.* 2006, Yang and Gao 2006).

In the GNSS/IMU/Imaging integration, the dynamic equation can be represented by (4-32), and the corresponding observation equations by (5-33) using the GNSS or image derived information. Then the innovation can be given by (Ding *et al.* 2007):

$$\boldsymbol{d}_i = \delta \boldsymbol{z}_i - \boldsymbol{H}_i \delta \boldsymbol{x}_{i/i-1} \tag{5-40}$$

The innovation covariance $E[\boldsymbol{d}_i \boldsymbol{d}_i^{\mathrm{T}}]$ can be obtained using a limited number of innovation samples applying the Sage windowing as (Mohamed and Schwarz 1999, Yang and Xu 2003, Yang 2004):

$$E\left[\boldsymbol{d}_i \, \boldsymbol{d}_i^{\mathrm{T}}\right] = \frac{1}{m} \sum_{j=0}^{m-1} \boldsymbol{d}_{i-j} \boldsymbol{d}_{i-j}^{\mathrm{T}} \tag{5-41}$$

For the optimal Kalman Filter, the innovation covariance $E[\boldsymbol{d}_i \boldsymbol{d}_i^{\mathrm{T}}]$ and the state predict covariance are equal:

$$\frac{1}{m} \sum_{j=0}^{m-1} \boldsymbol{d}_{i-j} \boldsymbol{d}_{i-j}^{\mathrm{T}} \approx \boldsymbol{H}_i \boldsymbol{P}_{i/i-1} \boldsymbol{H}_i^{\mathrm{T}} + \boldsymbol{R}_i \tag{5-42}$$

In practical applications, an adaptive factor α is normally introduced to modify the state predict covariance as:

$$\frac{1}{m} \sum_{j=0}^{m-1} \boldsymbol{d}_{i-j} \boldsymbol{d}_{i-j}^{\mathrm{T}} = \frac{1}{\alpha_i} \boldsymbol{H}_i (\boldsymbol{\Phi}_{i-1} \boldsymbol{P}_{i/i-1} \boldsymbol{\Phi}_{i-1}^{\mathrm{T}} + \boldsymbol{Q}_{i-1}) \boldsymbol{H}_i^{\mathrm{T}} + \boldsymbol{R}_i \tag{5-43}$$

The adaptive filtering using the Sage windowing has a good performance under the condition of a stable movement (Yang and Xu 2003, Yang 2004), because the construction of Sage windowing is based on the average of the samplings as (5-41), which requires a certain amount of measurements to estimate it. However, as mentioned before, in our case it is difficult to guarantee a stable flight condition, and the average calculation based on too many samplings is not safe. In order to properly reflect the situation of the movement only one step innovation at the epoch of camera exposure events is taken as:

$$E\left[\boldsymbol{d}_i \, \boldsymbol{d}_i^{\mathrm{T}}\right] = \Delta \bar{\boldsymbol{x}}_k \Delta \bar{\boldsymbol{x}}_k^{\mathrm{T}} = (\boldsymbol{z}_k - \boldsymbol{H}_k \boldsymbol{x}_{i/i-1})(\boldsymbol{z}_k - \boldsymbol{H}_k \boldsymbol{x}_{i/i-1})^{\mathrm{T}} \tag{5-44}$$

then, the adaptive factor α can then be estimated through (Yang *et al.* 2002, Yang and Gao 2006, Ding *et al.* 2007):

$$\alpha_i = \begin{cases} 1, & \text{else} \\ \dfrac{c}{|\Delta\tilde{\boldsymbol{x}}_i|}, & if\ |\Delta\tilde{\boldsymbol{x}}_i| > c \end{cases} \tag{5-45}$$

where, c is a constant number that is determined according to the different applications, which is chosen to be 1.0–1.5 (Yang*, et al.* 2002). In our case it was taken as 1 and

$$|\Delta\tilde{\boldsymbol{x}}_k| = \sqrt{\frac{trace\left\{\boldsymbol{H}_k(\boldsymbol{\Phi}_{i-1}\boldsymbol{P}_{i-1}\boldsymbol{\Phi}_{i-1}{}^{\mathrm{T}} + \boldsymbol{Q}_{i-1})\boldsymbol{H}_k{}^{\mathrm{T}}\right\}}{trace\left\{(\delta\boldsymbol{z}_k - \boldsymbol{H}_{\mathrm{k}}\delta\boldsymbol{x}_{\mathrm{i}}^{-})(\delta\boldsymbol{z}_k - \boldsymbol{H}_{\mathrm{k}}\delta\boldsymbol{x}_{\mathrm{i}}^{-})^{\mathrm{T}} - \boldsymbol{R}_k\right\}}} \tag{5-46}$$

The robust factor, β*,* was introduced in (5-37) to modify the covariance of the image observation errors, and improve the gain matrix:

$$\boldsymbol{K}_i = \boldsymbol{P}_{i/i-1}\boldsymbol{H}_{img}{}^{\mathrm{T}}[\boldsymbol{H}_{img}\boldsymbol{P}_{i/i-1}\boldsymbol{H}_{img}{}^{\mathrm{T}} + \frac{1}{\beta_i}\boldsymbol{R}_{img}]^{-1} \tag{5-47}$$

The robust factor, β*,* used in our application is estimated according to the following rule:

$$\beta_k = \begin{cases} 1 & , else \\ \dfrac{d_m}{\Delta\psi_k}, & if\ \Delta\psi_k > d_m \end{cases} \tag{5-48}$$

where, $\Delta\boldsymbol{\Psi}$ is the change in orientation obtained from consecutive images, and d_m indicates the threshold value of the changes in orientation obtained from consecutive images. $m = 1, 2, 3$ holds for roll, pitch and yaw respectively.

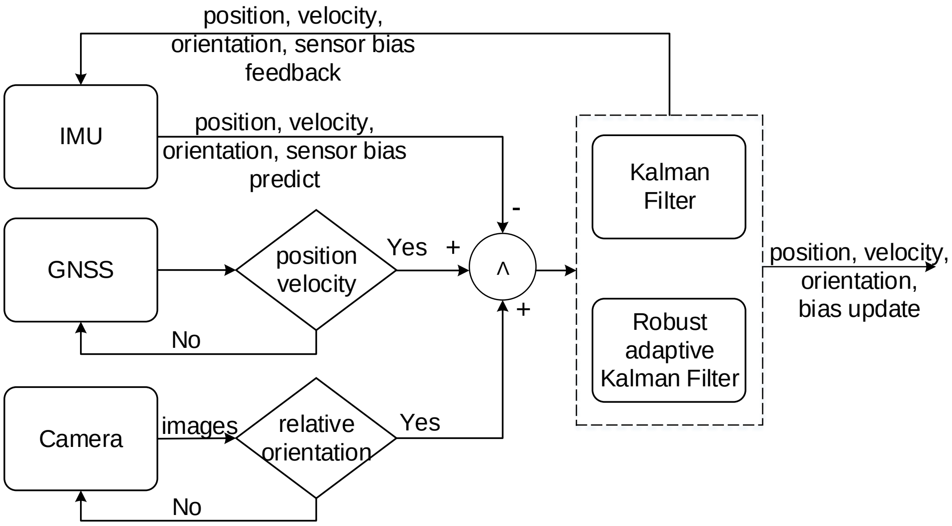

Fig. 5-8 The Image-aided orientation determination process for GNSS/IMU navigation using robust adaptive Kalman Filter

In general, the robust adaptive Kalman Filter was applied to the update process of our system.

The approach used for image-aided orientation determination for GNSS/IMU navigation using a robust adaptive Kalman Filter is illustrated in Fig. 5-8.

As shown in Chapter 4, if there is no update measurement available, the states of the navigation system, such as position, velocity, orientation angles and sensor bias can be calculated by the Inertial navigation equations from (4-27), and the corresponding errors can be predicted through the equations from (4-30) to (4-32). When the GNSS update is available, the GNSS/IMU Kalman Filter is activated, and the update process can be validated according to the equations from (4-36) to (4-38). If there are consecutive images that are taken simultaneously, the update process of GNSS/IMU/Imaging or IMU/Imaging is triggered, and the validation process can be done using the equations from (5-33) to (5-39). Meanwhile, a further improvement methodology, the robust adaptive Kalman Filter can be started. The adaptive factor of the robust adaptive Kalman Filter can be calculated by the equation (5-45), and the robust factor can be estimated by the equation (5-48). With the adaptive and robust factors, the covariance matrix of the Kalman Filter can be rewritten as Equation (5-43), and the gain matrix of can be modified as Equation (5-47).

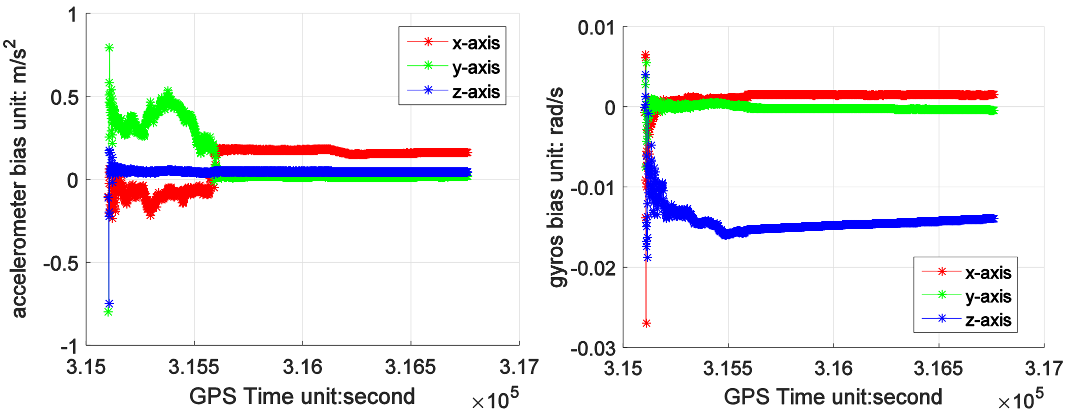

Fig. 5-9 Biases estimation of Crossbow IMU.

To check the efficiency of the new developed Kalman Fitler, the converge time can be used as a quick indicator. In principle if the bias are not estimated correctly, the Kalman Filter will corrupt. Fig. 5-9 shows the estimation of the bias of the low cost IMU using the GNSS/IMU/Imaging Kalman Filter in an airborne test. From this figure we can see that the convergence time is very short, within 10 minutes. We can then conclude that the sensor biases were estimated correctly in our GNSS/IMU/Imaging algorithm.

In general, the precise geometry information retrieved from consecutive images has great potential to improve the exterior orientation parameters of the low-cost DGS, some results of the GNSS/Low-cost-IMU/Imaging Kalman Filter have been published in the article of PERS (Yan *et al.* 2016), and the further results are discussed in the following chapter.

6 Results and analysis

In order to validate and assess the accuracy of the proposed method, three aribone tests were done in different places, using different types of low cost sensors. The proposed GNSS/MEMS-IMU/Imaging Kalman Filter used to process these data is based on the algorithm discribed in Chapter 5, and implemented using the Matlab platform and C/C++ languages.

6.1 Sensors and campaigns

In the scope of the PITVANT (Projecto de Investigação e Tecnologia em Veículos Aéreos Não-Tripulados) project, funded by the Portuguese Ministry of Defense, One of these tests was performed in 2011 in Alentejo, south of Portugal. The other two were near Espinho in the years of 2013 and 2017, in the north of Portugal. The aim of this project was the development and demonstration of tools and technologies for UAV applications.

6.1.1 Sensors

These tests were done with two different types of aerial vehicles, with a dual frequency GNSS receiver, two none-metric digital cameras and two types of MEMS IMUs. To use these sensors in these airborne applications, the specifications must be set rigorously.

The dual frequency GNSS receiver, NovAtel DL-V3, sampling at the frequency of 1Hz was used in all tests. The receiver and its aerial antenna are shown in Fig. 6-1. To get the GNSS measurement updates that will be used to feed the Kalman Filter implementations, the GNSS position, velocity, and the corresponding covariance matrix were obtained through the “RTKlib” software using the PPP kinematic strategy (Takasu 2013).

In this work, only observations from GPS were used; the elevation mask was set as 15°, the strategy of Ionosphere-free linear combination was used to correct the ionosphere delay, Saastamoinen model was used to correct troposphere delay; the LAMBDA method was applied to search the number of the integer ambiguities. Through this airborne test, the GNSS visibility was very good and therefore, the covariance of the observation errors, $\boldsymbol{R}_{gnss}$ defined in Equation (5-37), could be set as a diagonal matrix with the experimental diagonal elements as: $(0.1\ m)^2$,

$(0.1\ m)^2$, $(0.15\ m)^2$, $(0.05\ m/s)^2$, $(0.05\ m/s)^2$, $(0.05\ m/s)^2$. For tagging and triggering the IMU and the camera measurements, the NovAtel GNSS receiver was set to output a 1 PPS (Pulse Per Second).

Fig. 6-1 NovAtel DL-V3 GNSS receiver and the aerial antenna

Two types of MEMS IMUs, Xsens MTi (100 Hz) and Crossbow AHRS440CA-200 (50 Hz), were used during these tests, and the overview and specifications of these IMUs are shown in Fig. 6-2 and Table 6-1.

Xsens MTi Crossbow AHRS

Fig. 6-2 Overview of two MEMS IMUs used in this thesis

Table 6-1 The specifications of two MEMS IMUs used in this thesis (Crossbow Technology INC 2009, Xsens Technologies B.V. 2009).

	gyroscope		accelerometer (g = unit gravity)	
	noise density °/ sqrt(hr)	bias stability °/hr	noise density μg/sqrt(Hz)	bias stability mg
Xsens MTi	3.00	10	150	40
Crossbow AHRS	4.50	360	1700	15

Besides the low cost MEMS-IMU, two higher grades IMUs, a FOG (Fiber Optic Gyro) Litton LN200 (200 Hz) and a RLG (Ring Laser Gyro) iMar INAV-RQH (300 Hz), were available during these airborne tests. The overview and specifications of these high grade IMUs are shown in Fig. 6-3 and Table 6-2. Due to the Litton (tactical grade IMU) and iMar (navigation grade IMU) characteristics, the orientation solution derived from the integration GNSS/Litton and GNSS/iMar, using the software previously developed at OAUP (Tomé 2002, Deurloo 2011). were used as references to access the quality of the orientation information obtained with the method proposed in this thesis. According to previous results obtained, using a FOG or RLG IMU and GNSS integration algorithm developed by the Porto University group, the resulting orientation accuracy can be better than 0.05° (Tomé 2002, Deurloo 2011). As the RLG, iMar performs better than the FOG LN200, the derived orientation is even better.

Litton 200 iMar INAV-RQH

Fig. 6-3 Overview of the two higher grade IMUs for the comparison reference.

Table 6-2 Specifications of tow higher grade IMUs used as references (Litton System INC 1997, iMAR Navigation GmbH 2017).

	gyroscope		accelerometer (g = unit gravity)	
	noise density °/ sqrt(hr)	bias stability °/hr	noise density μg/sqrt(Hz)	bias stability mg
Litton-200	0.15	0.01	110	0.30
IMar INAV-RQH	0.0025	0.002	8	0.025

Additionally, two types of video cameras, a AVT Pike F505 (a 5-megapixel video camera) and a Sony ICX-204AK CCD camera were used in these tests. The overview and the specification of the two cameras are shown in Fig. 6-4 and Table 6-3.

AVT Pike video Sony ICX-204AK CCD

Fig. 6-4 Overview of two cameras used in this thesis.

Table 6-3 Specifications of two cameras used in this thesis.

	AVT Pike video	Sony ICX-204AK CCD
focal length (mm)	8.3	6
pixel size (μm × μm)	3.45 × 3.45	4.65 × 4.65
image size in pixels	2054 × 2452	1024 × 768

These are none-metric cameras and, as the rigorous calibration of interior orientation parameters were not available, the coefficients of a 3rd order polynomial correction were determined to compensate for radial distortion, together with improved focal distance and principal point position, in the process of auto calibration incorporated in the bundle adjustment.

The information about the orientation changes extracted from these images taken by the cameras were obtained using the “AGIsoft Photoscan” software, which uses a SIFT/SFM algorithm without GCPs (Agisoft 2016), as introduced in Chapter 5.2.1.

6.1.2 Campaigns

In order to test the robustness of the developed method in different scenarios, these tests were done with different flying height, velocity and image overlapping percentages. All the tests were equipped with a dual frequency GNSS receiver, a low cost camera, and two of these tests has both the low cost IMU and higher grade IMU, meanwhile one test only have the low cost IMU but with the AT solution was used as the reference.

Test 1 – Alentejo 2011

The first test was done in cooperation with the Portuguese Air Force (PAF) and performed by Squadron 401 "Cientistas" from the Montijo Air Force base. Data analyzed were collected on 9th September of 2011, south of Lisbon, Portugal, with a CASA C212 aircraft from PAF.

The IMUs available for testing were the MEMS Crossbow AHRS and the RLG iMar INAV-RQH. The NovAtel dual frequency GNSS receiver and the AVT Pike video camera were also mounted on the aircraft. The camera was mounted in a hole made on the fuselage, pointing vertically downwards. It was rigidly fixed in the fuselage. The GNSS antenna was mounted approximately on the vertical of the camera. Relative positions of all sensors (camera, IMU and GNSS antenna were measured with a total station.

This test flight was done in the early to mid-afternoon on a very hot day and there was a significant amount of turbulence. The flight altitude ranged between 300 m and 950 m, and the mean velocity was around 400 km/h.

For the purpose of this thesis, only one section of the flight was used. This flight was implemented for testing the algorithm of the strapdown gravimetry using UAVs (Bastos *et al.* 2013). Fig. 6-5 shows the section used in this thesis. It is a section flown in the E-W direction over the region of Alentejo. It has two sections where relatively smooth flight was possible, and imagery data with a good lateral and longitudinal coverage was available. The altitude for this smooth section of the flight was around 300 m, and the direction of the strips were from west to east, making a turn over the mines of Aljustrel, and coming back to west over the same path. The length of the strips was around 92 km. During the strips, 1169 images were taken and stored in a data logging computer, with the GPS time tags, with an overlap rate higher than 80%.

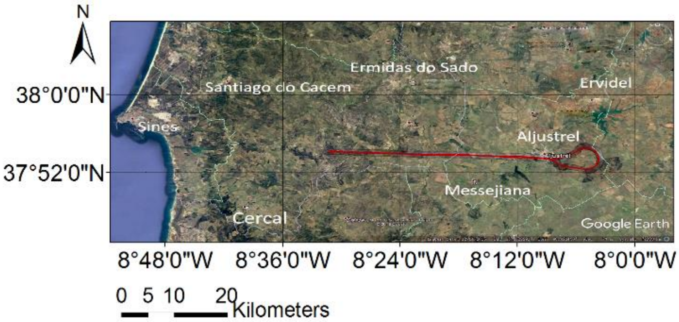

(a) The whole flight (b)The selected section.

Fig. 6-5 Trajectory of the Alentejo test 2011 projected in Google Earth.

Three different strategies were used to process the test data. The first one is a pure GNSS/Crossbow integration, the second one integrates the additional information derived from the images to improve the performance of the GNSS/Crossbow integration, and the third one uses a robust adaptive Kalman Filter to smooth the final orientation solution of the multi-sensor integration (GNSS/Crossbow/imaging).

During this test, the covariance matrix of the orientation information in $\boldsymbol{R}_{img}$ in Equation (5-37) can be set as a diagonal matrix with the elements being the standard deviations with values: $(0.02°)^2$, $(0.02°)^2$, $(0.03°)^2$.

The adaptive factor, α_i, and the robust factor, β_k, were estimated using (5-45) and (5-48), with the threshold values for roll, pitch and yaw set as: $d_1 = 0.2°$, $d_2 = 0.2°$, $d_3 = 0.5°$.

As mentioned before, the GNSS/IMU using the iMar is known to deliver accuracies of the order of 0.05° (Tomé 2002, Deurloo 2011), therefore the integration GNSS/iMar was used here as a reference in this test. Comparisons of results between the first strategy and the GNSS/iMar integration are shown in Fig. 6-6. The comparison of the results for the other two strategies is shown in Fig. 6-7 (GNSS/iMar results were used as reference), and the corresponding statistics, presented in Table 6-4 (GNSS/iMar results were used as reference). During this test, the mean values of the difference were used as the approximate compensation boresight.

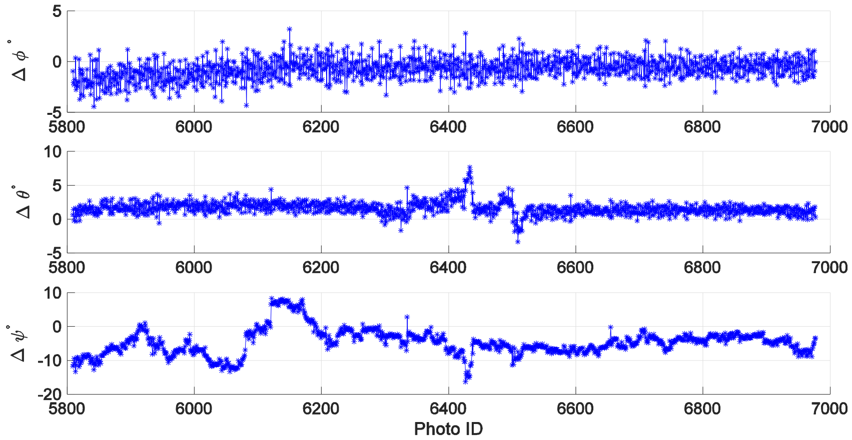

Fig. 6-6 Difference of the orientation solutions obtained with GNSS/Crossbow and with GNSS/iMar, unit: °.

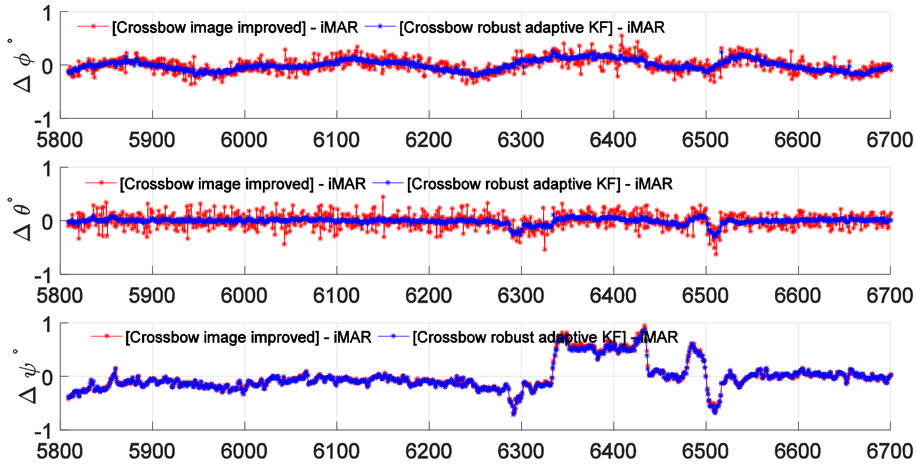

Fig. 6-7 Difference between the orientation solutions and the reference, obtained with the integration GNSS/Crossbow/Imaging, with and without using the robust-adaptive-image Kalman Filter, unit: °.

Table 6-4 Statistics of the difference between the orientation solutions and reference, obtained with the classical Kalman Filter for GNSS/Crossbow and GNSS/Crossbow/Imaging integration and with the robust-adaptive-image Kalman Filter, unit: °.

	GNSS/Crossbow			GNSS/Crossbow/Imaging (80% overlap rate)			further robust-adaptive-image (80% overlap rate)		
	roll	pitch	yaw	roll	pitch	yaw	roll	pitch	yaw
min	-3.728	-4.949	-11.601	-0.356	-0.619	-0.681	-0.220	-0.305	-0.711
max	3.917	6.082	12.936	0.551	0.452	0.945	0.257	0.115	0.868
std	**1.054**	**0.973**	**3.885**	**0.127**	**0.128**	**0.231**	**0.088**	**0.047**	**0.225**

From Fig. 6-6 and Table 6-4 we can see that the performance of the GNSS/Crossbow integration is not very good. The standard deviation of the orientation solution shows values of 1.054°, 0.973°, 3.885° for the Euler angles of roll pitch and yaw respectively. This agrees with the datasheet document of the Crossbow (Crossbow Technology INC 2009) and basically shows the type of accuracy that can be obtained with a pure GNSS/Crossbow integration. From Fig. 6-7 and Table 6-4 we can see that using the precise orientation update information derived from the images, the orientation standard deviation from the integration can be improved by one order of magnitude (from 1.054° to 0.127° in roll, from 0.973° to 0.128° in pitch, and from 3.885° to 0.225° in yaw). After introducing the robust adaptive Kalman Filter, a further improvement of 30% in roll, 63% in pitch and 2% in yaw, was obtained.

Espinho tests

Two airborne tests were done on 8th August 2013, and 16th January 2017, near the coastline of Espinho, south of Porto, north of Portugal. All the tests were based on a light-small aerial vehicle, as shown in Fig. 6-8. During these tests, the dual frequency NovAtel DL-V3 receiver was used, however, the other sensors available have changed from test to test.

Fig. 6-8 The overview of the light-small aerial vehicle

Test 2 – Espinho 2013

During this test, two types of IMUs were used, the MEMS Xsens MTi, and the Litton LN-200. Additionally, the AVT Pike F-505 camera and the dual frequency GPS receiver were mounted in the light-small aerial vehicle. The setup configuration is presented in Fig. 6-9. The LN-200 was mounted inside the body of the airplane, and the Xsens was mounted below the right wing, with the camera rigidly attached beneath. The GPS antenna was installed on the top of the right wing. The camera was mounted in a box, rigidly connected to the Xsens. Images are stored in a data logging computer, with the GPS time tags.

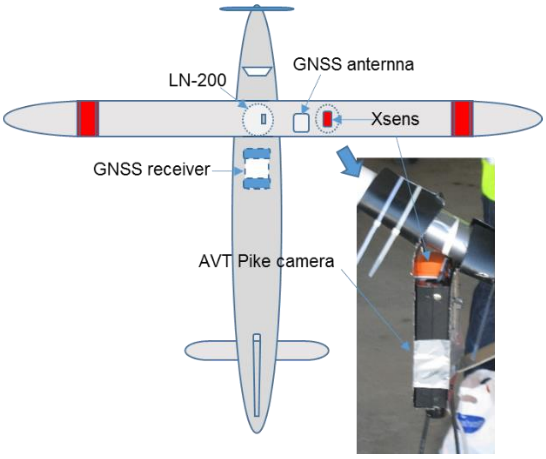

Fig. 6-9 The configuration of the test of Esphinho 2013

The average flying height for this airborne test was about 200 m, and the velocity was around 140 km/h. Contrary to the test of Alentejo 2011, which had a straight line strips, in this test, several curves were made, and one was selected to validate the proposed GNSS/MEMS-IMU/Imaging coupled Kalman Filter. Fig. 6-10 shows the section used in this thesis. This strip makes two big circles, and the length of this strip is around 11 km. During this part, the overlap rate of the successive images in the strip is 60%. A total of 120 images (from image 2523 to 2642, corresponding to the red trajectory in Fig. 6-10) were selected to assess the performance of the proposed method.

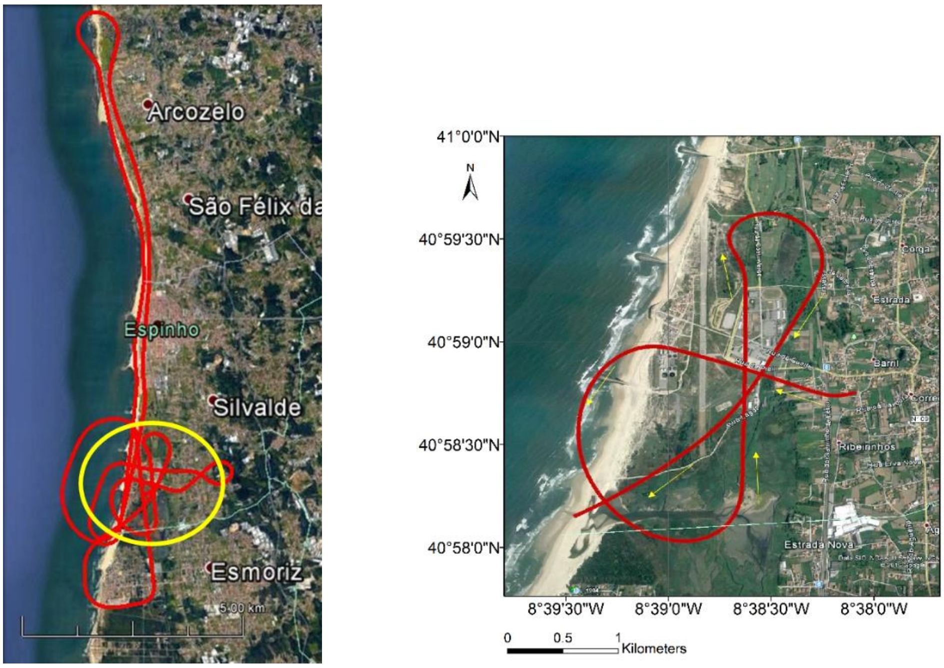

(a) The whole flight

(b) The selected section.

Fig. 6-10 Trajectory of the Espinho test 2013 projected in Google Earth.

Again three different strategies were used to process the test data. The first one is a pure GNSS/Xsens integration, the second one integrates the additional information derived from the images to improve the performance of the GNSS/Xsens integration, and the third one uses a robust adaptive Kalman Filter to smooth the final orientation solution of the multi-sensor integration (GNSS/Xsens/imaging).

Although in this test, the same camera of the Alentejo test was used, the overlap percentage (~60%) was much lower, therefore, the covariance matrix of the orientation information $\boldsymbol{R}_{img}$ in Equation (5-37) for this test was set as a diagonal matrix with the following values for the diagonal elements $(0.04°)^2, (0.04°)^2, (0.05°)^2$, larger than the one in test of Alentejo 2011, because of the less image overlap rate in this test.

The adaptive factor, α_i, and the robust factor, β_k, were also estimated using (5-45) and (5-48), with the same threshold values for roll, pitch and yaw set as: $d_1 = 0.2°$, $d_2 = 0.2°$, $d_3 = 0.5°$.

As mentioned before, the GNSS/IMU used in the LN200 is known to deliver accuracies of the order of 0.05° (Tomé 2002, Deurloo 2011), therefore the integration GNSS/Litton was used here as a reference in this test. Fig. 6-11 shows the comparison of the difference between the results of applying each of the three strategies and the results from the GNSS/Litton integration (GNSS/Litton solution was used as reference). Table 6-5 gives the statistics for these same comparisons (GNSS/Litton solution was used as reference). During this test, the mean values of the difference were used as the approximate compensation boresight.

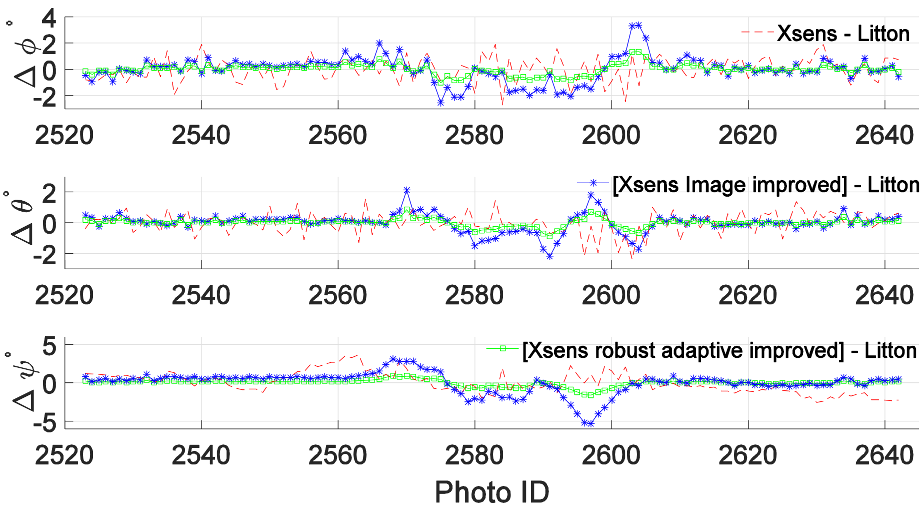

Fig. 6-11 Difference between the orientation solutions and the reference, obtained with the classical KF for GNSS/Xsens and GNSS/Xsens/Imaging integration and with the robust-adaptive-image Kalman Filter for the GNSS/Xsens/Imaging, unit: °.

Table 6-5 Statistics of difference between the orientation solutions and reference, obtained with the classical KF for GNSS/Xsens and GNSS/Xsens/Imaging integration and with the robust-adaptive-image Kalman Filter for the GNSS/Xsens/Imaging, unit: °

	GNSS/Xsens			GNSS/Xsens/Imaging (60% overlap rate)			further robust-adaptive-image (60% overlap rate)		
	roll	pitch	yaw	roll	pitch	yaw	roll	pitch	yaw
min	-2.733	-2.385	-2.545	-2.528	-2.163	-5.291	-1.011	-0.865	-1.587
max	1.912	1.581	3.641	3.338	2.123	3.100	1.335	0.849	0.930
std	**0.916**	**0.719**	**1.388**	**0.865**	**0.611**	**1.302**	**0.386**	**0.244**	**0.420**

From Fig. 6-11 and Table 6-5 we can see that the standard deviation from the orientation solution of the integration of GNSS/Xsens can be improved by 5% to 15% with the aid of the information of orientation changes retrieved from the images: from 0.916° to 0.865° in roll, from 0.719° to 0.611° in pitch, and from 1.388° to 1.302° in yaw. The orientation accuracy is further improved by 55% to 67% when using the robust-adaptive-image Kalman Filter.

Comparing with Table 6-4, we conclude that the standard deviation of the attitude angles is better for the Xsens than for the CrossBow. This is due to the fact that the Xsens has better gyros. We can see that the accuracy improvement of this test is not as big as for the test of Alentejo 2011, which is mainly due to the much lower image overlap rate. However, we can also see that the GNSS/IMU/imaging integration delivers better results in case of the CrossBow Table 6-4. This is due, not to the IMU, but to the better accuracy of the information derived from the images because in Alentejo 2011, when the CrossBow was used, the overlapping was 80%, better than the 60% of this test.

Test 3 – Espinho 2017

During this test only one IMU, the MEMS Xsens MTi was on board. The Sony ICX-204AK CCD camera and the dual frequency Novatel GNSS receiver were mounted in the same light-small aerial vehicle used in test of Espinho 2013. The configuration of this test is as Fig. 6-12.

The average flying height during this test was about 350 m, and the mean velocity was around 140 km/h. Contrary to what happened in tests, there was no higher grade IMU available, therefore, to validate the GNSS/MEMS-IMU/Imaging method, we had to obtain the orientation angles from the Aerial Triangulation. The AT results, obtained using 70 ground control points, were used as reference for the orientation angles. Those 70 ground control points are mainly distributed on the ground along the red trajectory shown in Fig. 6-13, the accuracy of the GCPs were set as 0.2 m, and a subset of this data was chosen to be analysed. The overlap rate of the successive images along the red strip is 60%. A total of 149 images (from image 2172 to 2320) were selected to assess the performance of the developed method.

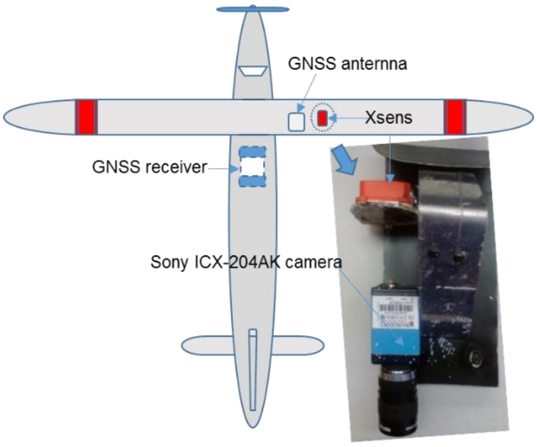

Fig. 6-12 The configuration of the test of Esphinho 2017

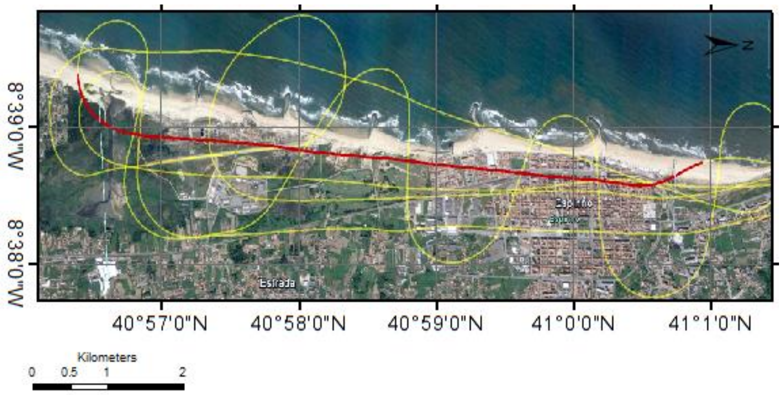

Fig. 6-13 Trajectory of the flight of the test of Esphinho 2017, projected in Google Earth. Ground control points are located along the red line.

Again three processing strategies were used: GNSS/Xsens integration, GNSS/Xsens/Imaging integration, and the robust-adaptive-image Kalman Filter. The quality of the camera used in this test is not as good as the one in the tests of Alentejo 2011 and Espinho 2013, and the overlap percentage is similar to test of Alentejo 2011 (60%). The covariance matrix of the orientation information, $\boldsymbol{R}_{img}$ for this test was set as a diagonal matrix with the diagonal elements being: $(0.05°)^2$, $(0.05°)^2$, $(0.08°)^2$ to account for the impact of the smaller overlap rate and the lower camera quality.

Fig. 6-14 gives the comparison of the difference between the results for each of the three strategies and the results from Aerial Triangulation (Aerial Triangulation solution was used as reference). Table 6-6 gives the statistics for these comparisons (Aerial Triangulation solution was used as reference). During this test, the mean values of the difference were used as the approximate compensation boresight.

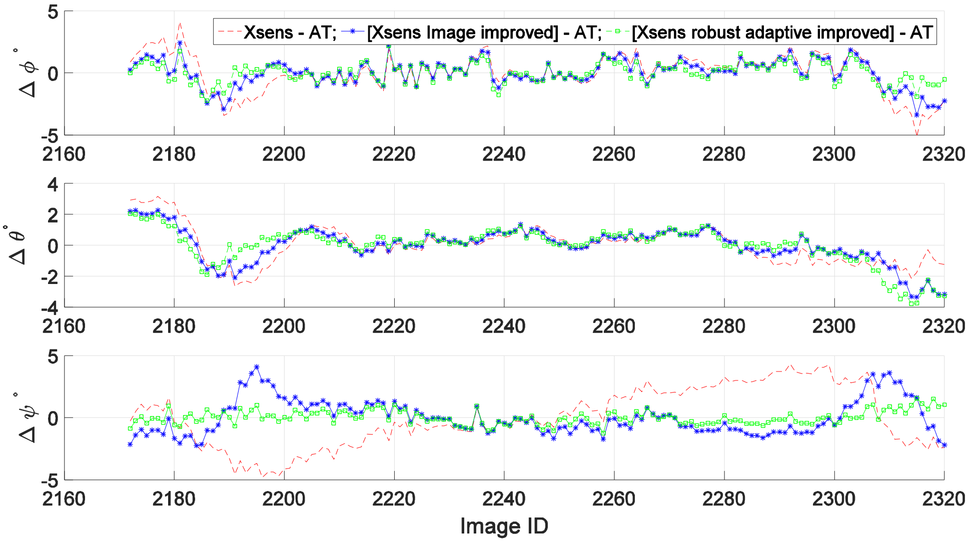

Fig. 6-14 Difference between the orientation solutions and the reference, obtained with the classical KF for GNSS/Xsens and GNSS/Xsens/Imaging integration and with the robust adaptive Kalman Filter for the GNSS/Xsens/Imaging, unit: °

Table 6-6 Statistics of difference between the orientation solutions and reference, obtained with the classical KF for GNSS/Xsens and GNSS/Xsens/Imaging integration and with the robust adaptive Kalman Filter for the GNSS/Xsens/Imaging, unit: °.

	GNSS/Xsens			GNSS/Xsens/Imaging (60% overlap rate)			further robust-adaptive-image (60% overlap rate)		
	roll	pitch	yaw	roll	pitch	yaw	roll	pitch	yaw
min	-5.216	-2.748	-4.879	-3.573	-2.927	-2.463	-2.524	-3.359	-1.253
max	3.726	2.842	4.378	2.212	1.933	3.988	2.239	1.685	1.708
std	**1.534**	**1.123**	**2.420**	**1.131**	**1.010**	**1.410**	**0.849**	1.031	**0.585**

From Fig. 6-14 and Table 6-6 we can see again that the standard deviation of the orientation solution of the GNSS/Xsens integration can be improved with the aid of the information of orientation changes retrieved from the images by up to 40%. Further improvement is achieved using the robust-adaptive-image Kalman Filter: additional 24% in roll and 58% in yaw but no improvement in pitch, which is because the height of this flight was quite constant (always around 350m), means less climbing and descending, and therefore without significant changes of pitch angles.

6.2 Summary

In the Espinho tests, a small light aerial vehicle was used to mount the dual frequency NovAtel GNSS receiver, the Xsens MEMS IMU and two types of low-cost digital cameras. The results show that the orientation standard deviation of the difference compared with the reference can be improved significantly if the relative geometric information from the images is introduced, and additional improvement can be obtained when the strategy of robust-adaptive-image Kalman Filter is implemented. The direct geo-referencing results in the Espinho 2017 test show that with the argument of the images geometric information the coordinates solution can also be improved.

Results from the Alentejo 2017 test were much better than the ones from Espinho, which is mainly due to two reasons: one is that this test was done using a bigger aircraft which allows a more stable flight than with a small aircraft; the other reason is that the image overlap during the Alentejo test is around 80%, much better than the 60% of the other two tests. This is a critical aspect because the accuracy of the relative orientation from the images mainly depends on the overlapping rate. However, we assumed that the orientation changes are not as sensitive to the platform velocity as the positions changes, therefore, we only focus on the orientation improvement rather than the position improvement.

7 Conclusion and recommendations

With the knowledge of the interior and exterior orientation parameters of camera images, the georeferenced information of an area of interest can be directly obtained through the technique of direct georeferencing. The interior parameters are related to the camera's specifications, and can be estimated precisely through a panel of grids or a calibration done before the practical applications. Exterior orientation parameters are referred to the position and orientation of the images taken by the cameras, and play a critical role during the process of direct georeferencing. The commercial POS, based on the integration of GNSS and high grade IMUs, can provide precise exterior position and orientation parameters. However, due to the high cost, large size and weight, these expensive, large and dedicate commercial POS are not proper for aerial photogrammetric surveys those based on small light vehicles, because they have limited payload and power supply capacitates.

Because of the bad performance of the MEMS-IMU, the integration of GNSS and a low-cost IMU cannot achieve enough accuracy as demanded for precise photogrammetric surveys, and there is a great demand to improve its performance, particular the orientation parameters, for mapping applications using UAVs.

Using a multi-sensor approach in moving platforms is becoming popular, however, the implementation of additional sensors, inevitably will increase the weight of the system, and the power consumption. Therefore, the direct exploitation of the precise geometry information retrieved from images, rather using additional sensors to improve the accuracy, becomes utmost interest.

In this thesis, a simple and cheap direct georeferencing system, consisting of different types of MEMS IMUs and consumer grade cameras, was implemented and tested in light airborne platforms. The algorithms for the backward intersection, forward intersection, and bundle adjustment were validated in practical photogrammetric works, using C/C++ and Matlab program modules. Results from the test at Anyang, China, in 2013 using a commercial POS, and the test in Espinho, in 2016, using our developed DGS, show that the accuracy of the developed algorithm for aerial triangulation and direct geroreferencing, is comparable to the commercial photogrammetry software.

A modified Kalman Filter to integrate GNSS, low-cost IMU and relative orientation information retrieved from camera, was implemented. For the development of the method, the rigorous conversion of the orientation parameters between the photogrammetric and navigation definitions of were deduced, which is the essential tie to fusion the two techniques

The critical part in setting up this methodology is mainly linked with the implementation of a modified Kalman Filter to integrate GNSS, low-cost IMU, and camera information. The Kalman Filter for integration of GNSS and IMU was already well established, and the main coupled strategies include loosely and tightly integrations. In this thesis, a 15 state Kalman Filter was implemented, and the equivalence of the loosely and tightly coupled strategies for GNSS and IMU integration, under the condition of the good GNSS observation, was proved and was validated through practical aerial test. The tightly coupled strategy can deliver a better performance under the situation of poor GNSS observation, but during our aerial applications, the GNSS signals were rarely blocked, as they frequently are in the case of terrestrial applications. Therefore, the loosely coupled Kalman Filter for integration of GNSS and IMU was chosen as the core method for our airborne application since it has a simple structure, robust characteristics and an equivalent performance compared with the tightly coupled.

Besides the GNSS update observation, the geometry information retrieved from consecutive images was also used as additional update observation. The critical aspect of introducing the image update is the construction of the image observation equation and the relative covariance matrix in the Kalman Filter.

The implementation of a robust adaptive Kalman Filter allows optimizing the output of a GNSS/low-cost-IMU/Imaging system. In the robust adaptive Kalman Filter, the setting of the adaptive factor is chosen according to experimental values following an heuristic approach, and the robust factor is obtained from the orientation changes derived from consecutive images without the need of previous information.

As the results from the airborne tests presented showed, the orientation accuracy of the GNSS/low-cost-IMU can be improved significantly with the implementation of a GNSS/MEMS-IMU/Imaging Kalman Filter, and can be further improved after the introducing of the adaptive robust Kalman Filter.

The obtained results mean that we could conduct a precise orientation estimation work without using an expensive IMU, which has great potential in photogrammetry and navigation applications using small light airborne platform, particular for the UAV.

The most important feature of this method is precisely the incorporation in the filter of the relative relationship of the consecutive images, with the advantage of decreasing, or eliminating, the need for surveying GCPs while reducing the demand on the quality of the IMU. Additional advantage is the fact that, there is no need to introduce any additional payload to the system. This guarantees a good quality of the exterior orientation parameters solution for photogrammetry, with applications in light-small aerial vehicles (particularly UAVs) as it is precise, efficient, and affordable. However, the accuracy of the proposed method depends on the overlapping rate of the images, as well as on the quality of the camera. According to the results from our aerial tests, we stress in particular the impact of the overlapping rate, as UAVs have a lower velocity than a normal airplane, have the ability to obtain images with higher overlapping rate.

Recommendations for Future works

There are still several topics related to the work in this thesis, which can be further exploited to the proposed low cost DGS or benefit the developed integration method. Some recommendations for further work can be made:

1) Along this thesis, only GPS observations were available, the exploration of the multi-GNSS strategies, such as introducing more measurements from the Galileo, GLONASS and BDS constellations, will be meaningful for the robustness of the GNSS solutions.

2) In our developed methodology, the orientation changes of the consecutive images are directly obtained by the commercial software of “AGIsoft Photoscan”, which were used as the new updated measurement update for the Kalman Filter. For the future work, it will be also an interesting topic to implement the pixels observations from the images as the update information of the Kalman Filter, to make a deeper combination of GNSS/IMU and the images.

3) For the uncertainties in the exposure time delay of the low cost cameras, Improve the exposure mechanical system of the camera to reduce the exposure time, which may involve some development work in the camera hardware.

4) For more intensive testing of its performance, the developed algorithm should be used to process data acquired with the system installed in a drone, which has more compact design and fly with much slower velocity. The low cost drone can be a commercial one, such as the DJI platform Pro, or even the cheap DIY.

5) Besides further work on the coupled algorithms of GNSS, IMUs and cameras, it will also worth to develop a cheap dual frequency geodetic GNSS receiver, which has the characters of small size, low weight, and more open to be embedded with other sensors.

6) Another a worth attention is to analysis the possibility to apply the developed method to

other low cost devices, i.e., using smartphones to acquire 3D information, since the smartphone has all the necessary sensors used, integrated in a relatively cheap unit.

In conclusion, there is still room for further developments of our GNSS/MEMS-IMU/Imaging method, allowing a further exploitation of such a low-cost system for 3D mapping.

References

Advanced Navigation, 2017, Spatial Reference Manual, URL: https://www.advanced navigation.com.au/product/spatial.

Agisoft, 2016, Agisoft PhotoScan User Manual Professional Edition, Version 1.2, URL: http://www.agisoft.com/pdf/photoscan-pro_1_2_en.pdf, A. LLC,St. Petersburg, Russia (last date accessed: 10 May 2016),

Andrew A.M., 2001. Multiple View Geometry in Computer Vision. *Kybernetes*, 30(9/10):1865 - 1872.

Angrisano A., 2010. GNSS/INS Integration Methods, UNIVERSITA' DEGLI STUDI DI NAPOLI, Napoli.

Ayres-Sampaio D., Deurloo R., Bos M., Magalhães A. and Bastos L., 2015. A comparison between three IMUs for strapdown airborne gravimetry. *Survey in Geophysics*, 36:1-16.

Babu R. and Wang J., 2004. Improving the quality of IMU-derived Doppler estimates for ultra-tight GPS/INS integration. *GPS/INS Integration GNSS*:16-19.

Bastos L., Yan W., Magalhães A., Ayres-Sampaio D. and Deurloo R., 2013. Assessment the Performance of Low Cost IMUs for Strapdown Airborne Gravimetry Using UAVs, *4th International Colloquium Scientific and Fundamental Aspects of the Galileo Programme*, Prague,Czech Republic.

Beidou Navigation Office, 2016. BeiDou Navigation Satellite System Signal In Space Interface Control Document, URL: http://www.beidou.gov.cn/.

Bernal D., Closas P., Calvo E. and Fernandezrubio J., 2009. Tight GNSS/INS integration as a constrained least-squares problem, *17th European Signal Processing Conference (EUSIPCO 2009)*, Glasgow, Scotland, pp. 85-89.

Bhatti U.I., Ochieng W.Y. and Feng S., 2007. Integrity of an integrated GPS/INS system in the presence of slowly growing errors. Part I: A critical review. *GPS Solutions*, 11(3):173-181.

Brown R.G. and Hwang P.Y.C., 1997. *Introduction to Random Signals and Applied Kalman Filtering.,* John Willey & Sons, New York., 484 p.

Choi K. and Lee I., 2013. A Sequential Aerial Triangulation Algorithm for Real-time Georeferencing of Image Sequences Acquired by an Airborne Multi-Sensor System. *Remote Sensing*, 5(1):57-82.

Chu T., Guo N., Backén S. and Akos D., 2012. Monocular camera/IMU/GNSS integration for ground vehicle navigation in challenging GNSS environments. *Sensors*, 12(3):3162-3185.

Collin J., Kappi J. and Saarinen J., 2001. Unaided MEMS-Based INS Application in a Vehicular Environment. *Journal of Cardiac Failure*, 9(4):286-295.

Cramer M., Stallmann D. and Haala N., 2000. Direct georeferencing using GPS/inertial exterior orientations for photogrammetric applications. *International Archives of Photogrammetry and Remote Sensing*, 33(B3/1; PART 3):198-205.

Cramer M., 2001. On the use of direct georeferencing in airborne photogrammetry, *3rd. International Symposium on Mobile Mapping Technology*, Universität Stuttgart, Fakultät Bauingenieur-und Vermessungswesen, Institut für Photogrammetrie.

Crossbow Technology INC, 2009, Crossbow 440 Serial User's Manual, URL: www.moog-crossbow.com/products/inertial-products/,

Dach R., Lutz S., Walser P., Fridez P. (Eds), 2015. *Bernese GNSS Software Version 5.2. User manual,* Astronomical Institute, Universtiy of Bern, Bern Open Publishing.,

Dellaert F., Seitz S.M., Thorpe C.E. and Thrun S., 2000. Structure from Motion without Correspondence. 2:557-564 vol.552.

Deurloo R.A., 2011. Development of a Kalman Filter Integrating System and Measurement Models for a Low-cost Strapdown Airborne Gravimetry System, Ph.D., University of Porto, Porto, 197 p.

Ding W., Wang J., Rizos C. and Kinlyside D., 2007. Improving Adaptive Kalman Estimation in GPS/INS Integration. *The Journal of Navigation*, 60(03):517-529.

Ding W., 2008. Optimal Integration of GPS with Inertial Sensors: Modelling and Implementation, The University of New South Wales, Sydney.

Dorn M., Lesjak R. and Wieser M., 2016. Improvement of the standard GNSS/IMU solution for UAVs using already existing redundant navigation sensors, Proceedings of the Navigation Conference (ENC), 2016 European.

Eisenbeiß H., 2009. UAV Photogrammetry, University of Technology Dresden, Zurich.

Ellum C. and El-Sheimy N., 2002. Land-based mobile mapping systems. *Photogrammetric Engineering and Remote Sensing*, 68(1):13-17.

European GNSS Service Centre, 2017. Galileo constellation., URL: https://www.gsceuropa.eu/system-status/Constellation-Information.

Flenniken W., Wall J. and Bevly D., 2005. Characterization of Various IMU Error Sources and the Effect on Navigation Performance, *Proceedings of ION GNSS 18th International Technical Meeting of the Satellite Division*.

Furukawa Y. and Ponce J., 2010. Accurate, dense, and robust multiview stereopsis. *Pattern Analysis and Machine Intelligence, IEEE Transactions on*, 32(8):1362-1376.

Gao W., Yang Y., Cui X. and Zhang S., 2006. Application of Adaptive Kalman Filtering Algorithm in IMU /GPS Integrated Navigation System. *Geomatics and Information Science of Wuhan University*, 31(5):466-469.

Gelb A., 1974. *Applied Optimal Estimation,* M.I.T. Press, Massachusetts.

GmbH i.N., 2017, iNAV-RQH-1003 Inertial Navigation System for Advanced Applications, URL: http://www.imar-navigation.de.

Godha S., 2006. Performance Evaluation of Low Cost MEMS-Based IMU Integration with GPS for Land Vehicle Navigation Application, University of Calgary, Calgary.

Godha S. and Cannon M.E., 2007. GPS/MEMS INS integrated system for navigation in urban areas. *GPS Solutions*, 11(3):193-203.

Gonçalves J. and Henriques R., 2015. UAV photogrammetry for topographic monitoring of coastal areas. *ISPRS Journal of Photogrammetry and Remote Sensing*, 104:101-111.

Grenzdörffer G.J., Engel A. and Teichert B., 2008. The photogrammetric potential of low-cost UAVs in forestry and agriculture. *The International Archives of the Photogrammetry, Remote Sensing and Spatial Information Sciences.*, XXXVII.

Gurtner W., 2007. RINEX: The receiver-independent exchange format. *Gps World*, 5(7):48-52.

Haarbrink R.B.E.K., 2006. *Helicopter UAV for photogrammetry and rapid response.- Proceedings: Second International Workshop - The Future of Remote Sensing.*

Hajiyev C. and Soken H.E., 2013. Robust Adaptive Kalman Filter for estimation of UAV dynamics in the presence of sensor/actuator faults. *Aerospace Science and Technology*, 28(2013):376-383.

Harris R.B. and Mach R.G., 2007. The GPSTk: an open source GPS toolkit. *GPS Solutions*, 11(2):145-150.

Herring T.A., King R.W. and Mcclusky S.C., 2008. Introduction to GAMIT. *GPS Measurements & Analysis*.

Hewitson S., 2006. Quality control for integrated GNSS and inertial navigation systems, The Univerisity of New South Wales, 200 p.

Hofmann-Wellenhof B., Lichtenegger H. and Collins J., 2001. *Global Positioning System: theory and practice,* Springer-Verlag, New York,

Hopkinson C., Chasmer L., Colville D., Fournier R.A., Hall R.J., Luther J.E., Milne T., Petrone R.M. and St-Onge B., 2013. Moving toward consistent ALS monitoring of forest attributes across Canada. *Photogrammetric Engineering & Remote Sensing*, 79(2):159-173.

Hutton J. and Mostafa M.M., 2005. 10 Years of Direct Georeferencing For Airborne Photogrammetry, Proceedings of the the 50th Photogrammetric Week 5-9 September, Stuttgart.

IGI mbH Company., 2007. *AEROoffice User Manual Vers. V5.1.,* IGI mbH Company., Kreuztal,

Jang H.S., Lee J.C., Kim M.S., Kang I.J. and Kim C.K., 2004. Construction of national cultural heritage management system using RC helicopter photographic surveying system, *Proceedings of the Proceedings of the XXth International Society for Photogrammetry and Remote Sensing Congress*, Istanbul, Turkey.

Jekeli C., 2001a. *Inertial Navigation Systems with Geodetic Applications,* Walter de Gruyter, Berlin and New York, 352 p.

Jekeli C., 2001b. Airborne Gravimetry Using INS/GPS and Gravity Gradiometers, *Proceedings of the 60th Annual Meeting of The Institute of Navigation*, pp. 476-482.

Jekeli C. and Kwon J.H., 2002. Geoid profile determination by direct integration of GPS inertial navigation system vector gravimetry. *Journal of Geophysical Research: Solid Earth (1978–2012)*, 107(B10):ETG 3-1-ETG 3-10.

Kaplan E.D. and Hegarty C., 2005. *Understanding GPS : principles and applications,* Artech House.

Khan B. and Qin Y., 2016. Tightly Coupled Integration of a Low Cost MEMS-INS/GPS System using Adaptive Kalman Filtering. *International Journal of Control and Automation*, 9(2):179-190.

Kremer J. and Kruck E., 2003. Integrated Sensor Orientation–Two Examples to show the Potential of simultaneous GPS/IMU and Image Data Processing. *Theory, Technology and Realities of Inertial/GPS Sensor Orientation*.

Kreye C., Eissfeller B. and Ameres G., 2004. Architectures of GNSS/INS integrations: Theoretical approach and practical tests, Proceedings of the Symposium on Gyro Technology.

Lassiter E.M., 2004. NAVSTAR GPS Space Segment/Navigation User Interfaces, (Rev. C). *ICD-GPS-200 C*.

Lee J.Y., Kim H.S., Choi K.H., Lim J., Chun S. and Lee H.K., 2016. Adaptive GPS/INS integration for relative navigation. *GPS Solutions*, 20(1):63-75.

Lin S.-G., 2015. Assisted adaptive extended Kalman filter for low-cost single-frequency

GPS/SBAS kinematic positioning. *GPS Solutions*, 19(2):215-223.

Litton System INC, 1997, LN-200 Inertial Measurement Unit.

Liu S., Sun F., Zhang L., Li W. and Zhu X., 2016. Tight integration of ambiguity-fixed PPP and INS: model description and initial results. *GPS Solutions*, 20(1):39-49.

Lowe D.G., 1999. Object recognition from local scale-invariant features, Proceedings of the Computer vision, 1999. The proceedings of the seventh IEEE international conference on.

Lowe D.G., 2004. Distinctive image features from scale-invariant keypoints. *International journal of computer vision*, 60(2):91-110.

Luhmann T., Robson S., Kyle S. and Boehm J., 2014. *Close-range photogrammetry and 3D imaging,* Walter de Gruyter, Berlin, 689 p.

Madeira S., Gonçalves J.A. and Bastos L., 2010. Photogrammetric mapping and measuring application using MATLAB. *Computers & geosciences*, 36(6):699-706.

Madeira S., Gonçalves J.A. and Bastos L., 2013. Accurate DTM generation in sand beaches using mobile mapping. *Journal of Coastal Conservation*:1-10.

Madeira S., Yan W., Bastos L. and Gonçalves J.A., 2014. Accuracy Assessment of the Integration of GNSS and a MEMS IMU in a Terrestrial Platform. *Sensors*, 14(11):20866-20881.

Mitishita E., Habib A. and Machado A., 2008. Photogrammetric model orientation using LiDAR dataset. *International Archives of Photogrammetry and Remote Sensing*, 37(B3a):167-172.

Moghaddamjoo A. and Kirlin R.L., 1993. Robust adaptive Kalman filtering. *Approximate Kalman Filtering*, 2:65-85.

Mohamed A. and Schwarz K., 1999. Adaptive Kalman filtering for INS/GPS. *Journal of Geodesy*, 73(4):193-203.

Nagai M., Chen T., Shibasaki R., Kumagai H. and Ahmed A., 2009. UAV-borne 3-D mapping system by multisensor integration. IEEE Transactions on Geoscience and Remote Sensing, 47(3):701-708.

NIMA, 2000. *Department of Defense World Geodetic System 1984, third edition,* National Imagery and Mapping Agency,

Niu X., Zhang Q., Gong L., Liu C., Zhang H., Shi C., Wang J. and Coleman M., 2015. Development and evaluation of GNSS/INS data processing software for position and orientation systems. *Survey Review*, 47(341):87-98.

Parkinson B.W. and Spilker J.J., 1996. *Global Positioning System: Theory and Applications,* American Institute of Aeronautics & Astronautics, 781 p.

Quist E.B. and Beard R.W., 2016. Radar odometry on fixed-wing small unmanned aircraft. *IEEE*

Transactions on Aerospace and Electronic Systems, 52(1):396-410.

Rutan S.C., 1991. Adaptive kalman filtering. *Analytical Chemistry*, 63(22):1103A-1109A.

Salazar D., Hernandez-Pajares M., Juan J.M. and Sanz J., 2010. GNSS data management and processing with the GPSTk. *GPS Solutions*, 14(3):293-299.

Savage P.G., 2016. Designing an extended Kalman Filter for a stellar aided strapdwon inertial attitude reference.

Saastamoinen, J., 1972. Atmospheric correction for the troposphere ans stratosphere in radio ranging of satellites. Geophysical Monograph Series, 15: 247-251

Schmidt G. and Phillips R., 2011. INS/GPS integration architecture performance comparisons. *NATO RTO Lecture Series, RTO-EN-SET-116, Low-Cost Navigation Sensors and Integration Technology*.

Scholten F., Sujew S. and Gwinner K., 2003. Application of GPS/INS-Systems with the HRSC - A Comparison of APPLANIX POS/AV-510 and IGI AEROcontrol-IId, Proceedings of the ISPRS Workshop Wg I/5, 22-23 Sept, Castelldefels, Spain.

Schwarz K.P., Chapman M., Cannon E. and Gong P., 1993. An Integrated INS/GPS Approach to the Georeferencing of Remotely Sensed Data. *Photogrammetric Engineering & Remote Sensing*, 59(11):1667-1674.

Shin E.-H., 2001. Accuracy Improvement of Low Cost INS/GPS for Land Application, Master, The University of Calgary, Calgary, Alberta, Canada, 119 p.

Snavely N., Seitz S.M. and Szeliski R., 2008. Modeling the world from internet photo collections. *International journal of computer vision*, 80(2):189-210.

Subirana J.S., Zornoza J.J., Hernández-Pajares M., 2013, GNSS DATA PROCESSING-Volume I: Fundamentals and Algorithms., URL: http://www.gage.upc.edu/gnss_book, E. Communications,Noordwijk.

System R.S., 2017. GLONASS constellation., URL: http://russianspacesystems.ru/.

Tachibana K., Sasagawa T. and Yotsumata T., 2004. Experimental study of direct georeferencing system (DGS) for large-scale mapping, *the XXth ISPRS congress, Istanbul*, pp. 12-23.

Takasu T., 2013, RTKLIB ver. 2.4.2 Manual, URL: http://www.rtklib.com/rtklib_document.htm.

Tawk Y., Tome P., Botteron C., Stebler Y. and Farine P., 2014. Implementation and Performance of a GPS/INS Tightly Coupled Assisted PLL Architecture Using MEMS Inertial Sensors. *Sensors*, 14(2):3768-3796.

Titterton D.H. and Weston J.L., 2004. *Strapdown Inertial Navigation Techonology,* The Institution of Electrical Engineers, Stevenage, 581 p.

Tomé P., 2002. Integration of Inertial and Satellite Navigation System for Aircrft Attitude Determination, University of Oporto, Porto, 218 p.

U.S. Air Force, 2017. The Global Positioning System, URL: http://www.gps.gov/.

VectorNav, 2017, VN-200 User Manual, URL: http://www.vectornav.com/products/vn-200,

Wang J., Garratt M., Lambert A., Wang J.J., Han S. and Sinclair D., 2008. Integration of GPS/INS/vision sensors to navigate unmanned aerial vehicles. *The International Archives of the Photogrammetry, Remote Sensing and Spatial Information Sciences*, 37:963-970.

Wang P. and Xu Y., 2010. *Photogrammetry (2nd version), in Chinese,* Wuhan University Press, Wuhan, 203 p.

Watson R.M., Sivaneri V. and Gross J.N., 2016. Performance Characterization of Tightly-Coupled GNSS Precise Point Positioning Inertial Navigation within a Simulation Environment, Proceedings of the 2016 AIAA Guidance Navigation and Control Conference. AIAA.

Werries A. and Dolan J.M., 2016. Adaptive Kalman Filtering Methods for Low-Cost GPS/INS Localization for Autonomous Vehicles.

Westoby M.J., Brasington J., Glasser N.F., Hambrey M.J. and Reynolds J.M., 2012. 'Structure-from-Motion' photogrammetry: A low-cost, effective tool for geoscience applications. *Geomorphology*, 179:300-314.

Winkler S., Schulz H., Buschmann M., Kordes T. and Vörsmann P., 2004. Improving low-cost GPS/MEMS-based INS integration for autonomous MAV navigation by visual aiding, Proceedings of the ION GNSS.

Wolf P., DeWitt B. and Wilkinson B., 2014. *Elements of Photogrammetry with Application in GIS, Fourth Edition,* McGraw-Hill Education, 696 p.

Won D.H., Lee E., Heo M., Sung S., Lee J. and Lee Y.J., 2014. GNSS integration with vision-based navigation for low GNSS visibility conditions. *GPS Solutions*, 18(2):177-187.

Woodman O.J., 2007. An Introduction to Inertial Navigation. *University of Cambridge, Computer Laboratory, Tech. Rep. UCAMCL-TR-696*.

Xia G., Wang G., Chen X. and Xue J., 2016. Low-cost MEMS-INS/GNSS integration using quaternion-based nonlinear filtering methods for USV, Proceedings of the OCEANS 2016-Shanghai, 10 -13 Apr Shanghai.

Xsens Technologies B.V., 2009, MTi-G User Manual and Technical Documentation, URL: https://www.xsens.com/.

Xu G., 2014. *GPS: theory, algorithms and applications,* Springer Science & Business Media.

Yan W., Li Y. and Xue Y., 2016. Introducing the optimal adaptive factor to improve the accuracy of airborne gravimetry based on the state model method (in Chinese). *Chinese Journal of Geophysics- Chinese Edition*, 59(4):1267-1274.

Yan W., Bastos L., Madeira S., Magalhães A. and Gonçalves J.A., 2017. Using Relative Orientation to Improve the Accuracy of Exterior Orientation Parameters of Low Cost POS. *Photogrammetric Engineering & Remote Sensing.*, 83(2):153-161.

Yang Y., Song L. and Xu T., 2002. Robust estimator for correlated observations based on bifactor equivalent weights. *Journal of Geodesy.*, 76:353-358.

Yang Y. and Xu T., 2003. An Adaptive Kalman Filter Based on Sage Windowing Weights and Variance Components. *THE JOURNAL OF NAVIGATION*, 56(02):231-240.

Yang Y. and Gao W., 2006. An Optimal Adaptive Kalman Filter. *Journal of Geodesy*, 80(4):177-183.

Yang Y., 2008. Tightly coupled MEMS INS/GPS integration with INS aided receiver tracking loops. *University of Calgary*.

Yang Y.X., 2004. *Adaptive Navigation and Kinematic Positioning (in chineses).* Sinomap, Beijing, 324 p.

Zongjian L., 2008. UAV for mapping-Low altitude photgrammetric survey. *The International Archives of the Photogrammetry, Remote Sensing and Spatial Information Sciences.*, XXXVII.

Appendix A. The estimation of satellite position and velocity from ephemeris

Once the signal transmit time is determined, the satellite position and velocity can be calculated by the ephemeris. The GNSS satellite position and velocity can be precisely estimated by a interpolation polynomial using the precise ephemeris in a post process model. The broadcast ephemeris consists of the Kaplerian elements and perturbation, and the estimation of GNSS positon and velocity can be achieved in real-time from the broadcast ephemeris. This appendix gives an example of the estimation of GNSS position and velocity from the broadcast ephemeris. The parameters of GPS broadcast ephemeris is shown as Table A-1.

Table A-1 The parameters of GPS broadcast ephemeris (Lassiter 2004, Angrisano 2010).

Parameter	Description	Note
M_0	Mean Anomaly at Reference Time	Keplerian Element (rad)
Δn	Mean Motion Correction	Perturbation Term (rad/s)
e	Eccentricity	Keplerian Element
$sqrt(A)$	Square Root of Semi-Major Axis	Keplerian Element ($m^{1/2}$)
Ω_0	Longitude of Ascending Node at Weekly Epoch	Keplerian Element (rad)
i_0	Inclination Angle at Reference Time	Keplerian Element (rad)
ω	Argument of Perigee	Keplerian Element (rad)
$\dot{\Omega}$	Rate of Right Ascension	Perturbation Term (rad/s)
$IDOT$	Rate of Inclination Angle	Perturbation Term (rad/s)
C_{uc}	Amplitude of the Cosine Harmonic Correction Term to the Argument of Latitude	Perturbation Term (rad)
C_{us}	Amplitude of the Sine Harmonic Correction Term to the Argument of Latitude	Perturbation Term (rad)
C_{rc}	Amplitude of the Cosine Harmonic Correction Term to the Orbit Radius	Perturbation Term (m)
C_{rs}	Amplitude of the Sine Harmonic Correction Term to the Orbit Radius	Perturbation Term (m)
C_{ic}	Amplitude of the Cosine Harmonic Correction Term to the Angle of Inclination	Perturbation Term (rad)
C_{is}	Amplitude of the Sine Harmonic Correction Term to the Angle of Inclination	Perturbation Term (rad)
t_{oe}	Reference Time Ephemeris	s

The process of estimating GPS satellite position and velocity using the broadcast ephemeris in ECEF frame can be summarized as Table A-2.

Table A-2 Algorithm for the GPS Satellite Position and Velocity Computation (Lassiter 2004, Angrisano 2010)

$\mu = 3.986005\times10^{14}\,(\mathrm{m^3/s^2})$	Earth's Gravitational Constant
$\dot{\Omega}_e = 2921151467\times10^{-5}\,(\mathrm{rad/s})$	Earth's Rotation Rate
$A = (\,sqrt(A)\,)^2$	Semi-Major Axis
$n_0 = sqrt(\mu/A^3)$	Computed Mean Motion
$\Delta t = t - t_{oe}$	Time from t_{oe}
$n = n_0 + \Delta n$	Corrected Mean Motion
$M = M_0 + \mathrm{n}\times\Delta t$	Mean Anomaly
$M = E - e\times\sin E$	Kepler's Equation
$\dot{M} = n$	Mean Anomaly Rate
$\dot{E} = \dfrac{\dot{M}}{1-e\times\cos E}$	Eccentric Anomaly Rate
$v = \tan^{-1}\left(\dfrac{\sqrt{1-e^2}\sin E}{\cos E - e}\right)$	True Anomaly
$\dot{v} = \dfrac{\sin E\times\dot{E}\times(1+e\cos v)}{(1-e\cos E)\times\sin v}$	True Anomaly Rate
$\theta = v+\omega$	Argument of Latitude
$u = \theta + C_{us}\times\sin(2\theta) + C_{uc}\times\cos(2\theta)$	Corrected Argument of Latitude
$\dot{u} = \dot{v} + 2[C_{us}\times\cos(2\theta) - C_{uc}\times\sin(2\theta)]\ \times\dot{v}$	Argument of Latitude Rate
$r = A[1\text{-}e\cos(E)]+C_{rs}\times\sin(2\theta)+C_{rc}\times\cos(2\theta)$	Corrected Radius
$\dot{r} = A\times e\times\sin\mathrm{E}\times\dot{E}\ +2[C_{rs}\times\cos(2\theta) - C_{uc}\times\sin(2\theta)]\times\dot{v}$	Radius Rate
$i = i_0 + IDOT\times\Delta t + C_{is}\times\sin(2\theta) + C_{ic}\times\cos(2\theta)$	Corrected Inclination
$i' = IDOT+2[C_{is}\times\cos(2\theta) - C_{ic}\times\sin(2\theta)]\ \times\dot{v}$	Inclination Rate
$\Omega=\Omega_0+(\,\dot{\Omega} - \dot{\Omega}_e\,)\Delta t - \dot{\Omega}_e\ \times t_{oe}$	Corrected Longitude of Ascending Node
$\Omega' = (\,\dot{\Omega} - \dot{\Omega}_e\,)$	Longitude of Ascending Node Rate
$x_{orb}=r\times\cos u;\quad y_{orb}=r\times\sin u;\ z_{orb}=0$	Position in Orbital Plane
$\dot{x}_{orb}=\dot{r}\cos u - y_{orb}\dot{u};\quad \dot{y}_{orb}=\dot{r}\sin u - x_{orb}\dot{u};\quad \dot{z}_{orb}=0$	Velocity in Orbital Plane
$x = x_{orb}\times\cos\Omega - y_{orb}\times\cos i\times\sin\Omega$ $y = x_{orb}\times\sin\Omega + y_{orb}\times\cos i\times\cos\Omega$ $z = y_{\mathrm{orb}}\times\sin i$	Position in ECEF
$\dot{x} = \dot{x}_{orb}\times\cos\Omega - \dot{y}_{orb}\times\cos i\times\sin\Omega + y_{orb}\times\sin i\times\sin\Omega\times i' - y\times\dot{\Omega}$ $\dot{y} = \dot{x}_{orb}\times\sin\Omega + \dot{y}_{orb}\times\cos i\times\cos\Omega - y_{orb}\times\sin i\times\cos\Omega\times i' + x\times\dot{\Omega}$ $\dot{z} = \dot{y}_{orb}\times\sin i + y_{orb}\times\cos i\times i'$	Velocity in ECEF

Appendix B. The Least-squares method

The Least-squares method is the most common estimation procedure in geomatics application and the estimation of the unknown state parameters. The basic algorithm is introduced as following paragraphs.

Assuming there is a measurement vector $\boldsymbol{y}$, which can be expressed in a linear equations as:

$$\boldsymbol{y} = \boldsymbol{Hx} + \boldsymbol{v} \tag{B-1}$$

where, the elements of the unknown parameter vector $\boldsymbol{x}$ are independent, and the random error vector $\boldsymbol{v}$ are in the Gauss Normal distribution.

then, the least square cost function, J_{LS}, is defined as the sum of the squared measurement errors as:

$$J_{LS} = v_1{}^2 + v_2{}^2 + \ldots + v_m{}^2 = \boldsymbol{v}^{\mathrm{T}}\boldsymbol{v} \tag{B-2}$$

The least-square method is based on the assumption that the numerical value of cost function is minimum:

$$\boldsymbol{v}^{\mathrm{T}}\boldsymbol{v} = \min \tag{B-3}$$

According to Equation (B-1), the cost function can be rewritten as:

$$\begin{aligned} J_{LS} &= (\boldsymbol{y} - \boldsymbol{Hx})^{\mathrm{T}}(\boldsymbol{y} - \boldsymbol{Hx}) \\ &= \boldsymbol{y}^{\mathrm{T}}\boldsymbol{y} - \boldsymbol{y}^{\mathrm{T}}\boldsymbol{Hx} - \boldsymbol{x}^{\mathrm{T}}\boldsymbol{H}^{\mathrm{T}}\boldsymbol{y} + \boldsymbol{x}^{\mathrm{T}}\boldsymbol{H}^{\mathrm{T}}\boldsymbol{Hx} = \min \end{aligned} \tag{B-4}$$

To minimize the cost function, the derivate of $\boldsymbol{J}_{LS}$ could assumed be zero:

$$\begin{aligned} \frac{\partial J_{LS}}{\partial \boldsymbol{x}} &= \boldsymbol{0}^{\mathrm{T}} - \boldsymbol{y}^{\mathrm{T}}\boldsymbol{H} - (\boldsymbol{H}^{\mathrm{T}}\boldsymbol{y})^{\mathrm{T}} + (\boldsymbol{H}^{\mathrm{T}}\boldsymbol{Hx})^{\mathrm{T}} + \boldsymbol{x}^{\mathrm{T}}\boldsymbol{H}^{\mathrm{T}}\boldsymbol{H} \\ &= -2\boldsymbol{y}^{\mathrm{T}}\boldsymbol{H} + 2\boldsymbol{x}^{\mathrm{T}}\boldsymbol{H}^{\mathrm{T}}\boldsymbol{H} = \boldsymbol{0} \end{aligned} \tag{B-5}$$

The called "normal equation" can be obtained as:

$$\boldsymbol{H}^{\mathrm{T}}\boldsymbol{H}\boldsymbol{x} = \boldsymbol{H}^{\mathrm{T}}\boldsymbol{y} \tag{B-6}$$

then, the unknown parameter vector $\boldsymbol{x}$ can be estimated as*:*

$$\hat{\boldsymbol{x}} = (\boldsymbol{H}^{\mathrm{T}}\boldsymbol{H})^{-1}\boldsymbol{H}^{\mathrm{T}}\boldsymbol{y} \tag{B-7}$$

If the weights matrix of each measurements are given, the cost function (B-4) can be rewritten as:

$$J_{WLS} = \boldsymbol{v}^{\mathrm{T}}\boldsymbol{W}\boldsymbol{v} \tag{B-8}$$

where, $\boldsymbol{W}$ is the weight matrix, which normally are calculated by:

$$\boldsymbol{W} = diag(\sigma_1^{-2}, \sigma_2^{-2}, ..., \sigma_m^{-2}) \tag{B-9}$$

where, σ_i is the a-priori standard deviation of the i^{th} measurement error.

then, the Equation (B-7) becomes*:*

$$\hat{\boldsymbol{x}} = (\boldsymbol{H}^{\mathrm{T}}\boldsymbol{W}\boldsymbol{H})^{-1}\boldsymbol{H}^{\mathrm{T}}\boldsymbol{W}\boldsymbol{y} \tag{B-10}$$